Alma Mater Studiorum - Università di Bologna

DOTTORATO DI RICERCA IN

CHIMICA

Ciclo 35°

Settore Concorsuale: 03/C1 - CHIMICA ORGANICA

Settore Scientifico Disciplinare: CHIM/06 - CHIMICA ORGANICA

Innovative photoresponsive materials & supramolecular structures

Presentata da: Alessio Cremonini

Coordinatore Dottorato

Luca Prodi

Supervisore

Stefano Masiero

Co-supervisore

Luca Valgimigli

Esame finale anno 2023

Prologo

La mia esperienza di dottorato si è svolta nel periodo più buio che l'umanità abbia mai attraversato da quando ho memoria. Le persone sono state lasciate morire di proposito e private del loro lavoro senza alcuna ragione scientifica concreta. Alcuni sono stati ingannati e uccisi nel silenzio generale. Quasi tutti coloro che avrebbero dovuto assistere le persone e denunciare ciò che stava accadendo hanno preferito crogiolarsi nel loro silenzio per non mettere a rischio il loro patrimonio monetario e il loro status quo.
Avendo le capacità e le possibilità, ho fatto tutto il possibile per aiutare chi ne aveva bisogno, sacrificando tempo ed energie che avrei voluto dedicare al mio percorso di ricerca.
Ho fatto questa scelta.
E la rifarei altre mille volte.

Nonostante ciò, sono soddisfatto dei risultati ottenuti.
Buona lettura.

Prologue

My PhD experience took place in the darkest period humanity has gone through since I can remember. People were purposely left to die and deprived of their work without any concrete scientific reasons. Some have been deceived and murdered in general silence. Almost all those who should have assisted people and denounce what was happening preferred to bask in their silence so as not to risk their monetary assets and their status quo.
Having the ability and possibilities required, I did everything possible to help those in need, sacrificing time and energy that I would have liked to devote to my research.
I made this choice.
And I would do it again and again.

Despite this, I am satisfied with the results achieved.
Enjoy the reading.

Acknowledgements

The first person who deserves my gratification is the chemistry "Gran Maestro", aka Professor **Stefano Masiero**, who guided me throughout my adventure. His knowledge and experience have been fundamental for the realization of all the projects described in this thesis. Since the first days of collaboration a "chemistry" has grown between us, leading the team to achieve unexpected goals, considering the poor funds and the inadequacy of the facilities available for our research group. Together we founded an imaginary association, the "Masiero & Cremonini Foundation" which, thanks to its spontaneous donations, has allowed us to fix the lack of equipment, facilities and more that should have been supplied by the department. The other member of the research group, Professor **Silvia Pieraccini** certainly deserves my heartfelt thanks from both scientific and human side; I have established a good relationship of trust and friendship with her too! I sincerely hope that your research can proceed in the best possible way and that it will be properly valued in the coming years. I'm grateful to **Andre Cantelli** and **Paolo Neviani** for supporting me during the chemical experience and beyond. **Fabio Mollica**, the PhD with whom I shared the office, was an excellent fellow adventurer with whom I have always dealt with on many topics, even those not related to research. He has always made himself kind and available for any advice. I hope you can continue your career as best as possible! A special recognition to the TU/e SFD research group which offered me their hospitality during my abroad period. Professor **Albert Schenning**, Professor **Michael G. Debije** and the PhDs **Jeroen Sol**, **Henk Sentjens** and **Mark Del Pozo Puig** supported me in the development of the project described in chapter 2, gave me enormous knowledge and assisted me for any need. I hope to meet you again guys! Professor **Maria Grazia Focarete**, Professor **Chiara Gualandi** and especially **Michele Zanoni** have been vital in the development of the project described in chapter 3. Good luck for your future projects! I can't forget to mention my graphic assistants **Matte Rizza** and **Mattia Di Giovanni**, without whom the presentation of the projects would have been a real nightmare, thanks guys!
I must mention all the people who supported me even though they were not directly involved in the scientific project: my **family**, the **physicians** of the Ferrari Hub, my **friends** and **all those who gratified my sacrifices** aimed at saving people.
Last but not least, **Raisa Dahnovici**: thank you for supporting me, but especially putting up with me for these long years!

Table of contents

Abstract

This thesis focuses on two main topics: photoresponsive azobenzene-based polymers and supramolecular systems generated by the self-assembly of lipophilic guanosines.
In the first chapters describe innovative photoresponsive devices and materials capable of performing multiple roles in the field of soft robotics and energy conversion. **Chapter 2** describes a device obtained by coupling a photoresponsive liquid-crystalline network and a piezoelectric polymer to convert visible light into electricity. **Chapter 3** deals with a material that can assume different shapes when triggered by three different stimuli in different environments. **Chapter 4** reports a highly performing artificial muscle that contracts when irradiated.
The last two chapters report on supramolecular structures generated from functionalized guanosines dissolved in organic solvents. **Chapter 6** illustrates the self-assembly into G-quadruplexes of 8- and 5'-functionalized guanosines in the absence of templating ions. **Chapter 7** describes the supramolecular structure generated by the assembly of a lipophilic guanosine in the presence of silver cations.
Chapter 6 is reproduced from an already published paper, while the other chapters are going to be submitted to different journals in a couple of months.

CHAPTER 1

Azobenzenes
Dyes able to give life to objects

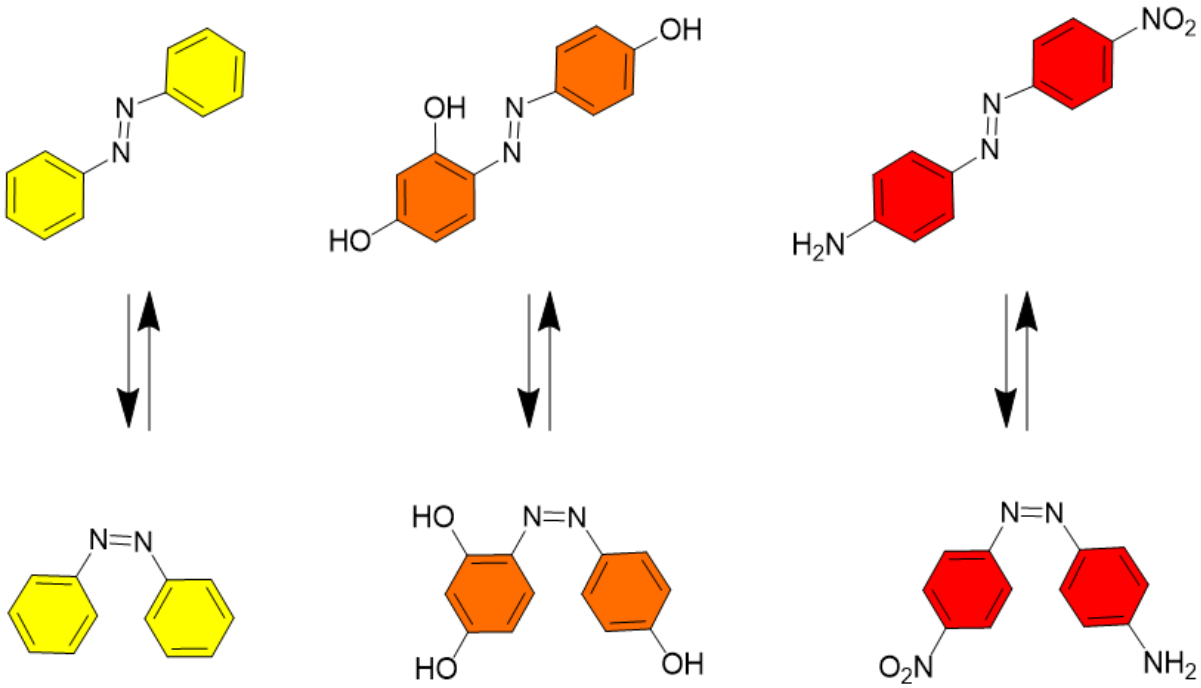

History

Azobenzenes have been discovered almost two centuries ago by Mitscherlich [1], since that day azobenzenes have evolved from simple dyes to 'little engines' and have become ubiquitous in many aspects of our lives, ranging from textiles, cosmetics, food and medicine to energy conversion and photonics.

In the first century following their discovery, azobenzene compounds were exclusively investigated for their use in the dye industry, focusing on finding dyes with good light stability that could be prepared quickly and cheaply. In 1930 an azo compound — sulfonamidochrysoïdine, also known as prontosil — become the first antibiotic to be commercialized, leading to a revolution in medicine[2]. It was only in 1937 that Hartley first reported that azobenzene undergoes photoisomerization from the more stable E (trans) configuration to the Z (cis) form, and succeeded in the isolation and characterization of the Z isomer [3]: this discovery led to the evolution of azos, from simple dyes to molecules capable of controlling the properties of different materials for multiple applications [4-8]. In the last 100 years enormous progress has been made in the synthesis and use of azobenzenes, some of which have also led to important results, awarded by the Nobel prize (**Figure 1**).

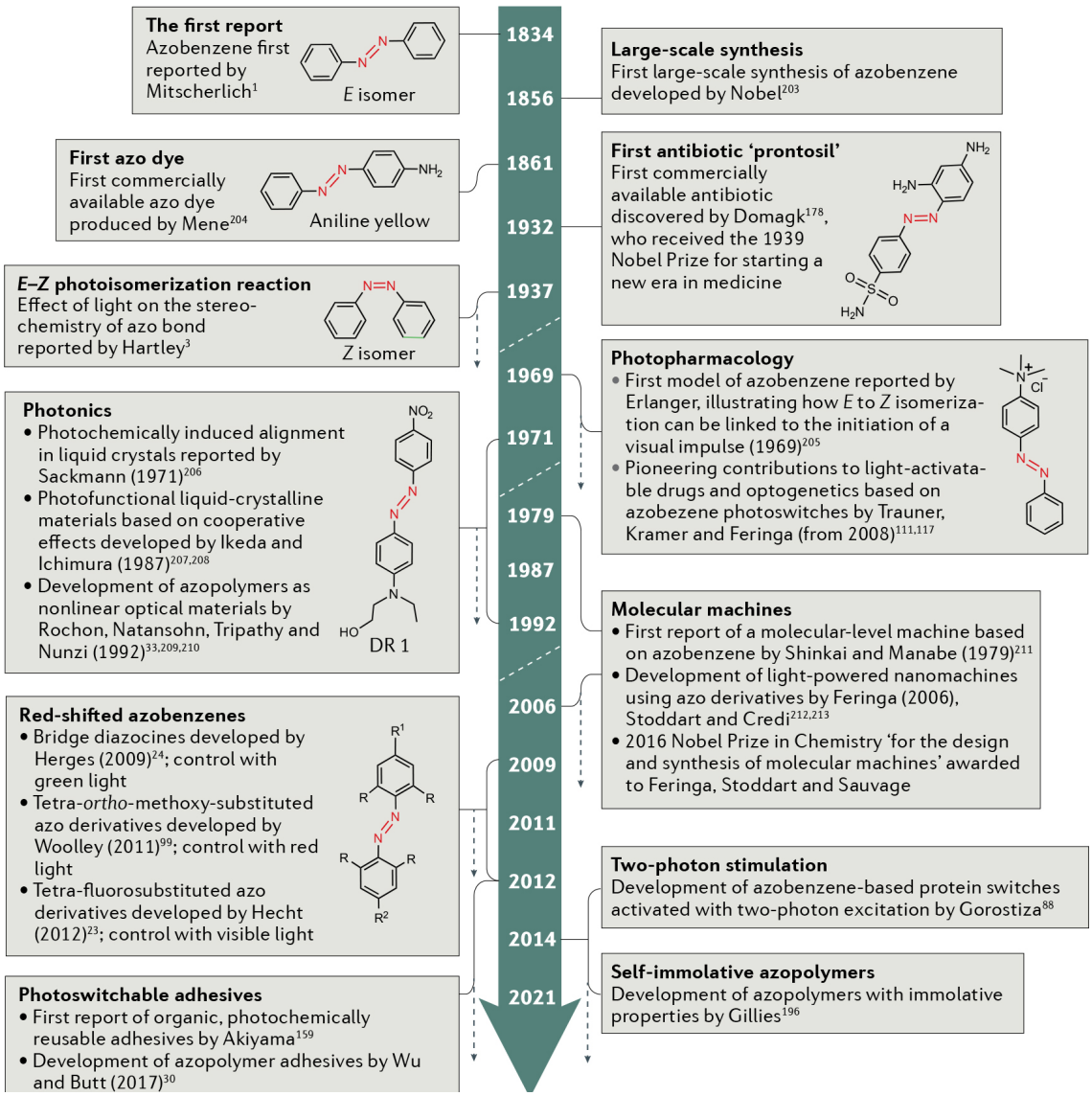

Figure 1 The evolution of azobenzenes: from their first report in 1834 to the fabrication of modern actuators for soft-robotics and smart drugs.

Chemical proprieties

To understand the photoresponsive properties of azobenzenes and their use as molecular switches, some general aspects about their spectroscopy and isomerization mechanism must be introduced. Generally, the E isomer is thermodynamically more stable than the Z isomer, although this order can be the reversed in the case of constrained azobenzenes (namely diazocines). E-azobenzene has a singlet ground state (S_0), and S_1 and S_2 are the first and second singlet excited states, respectively.

The E–Z photoisomerization of azobenzenes occurs through either $S_0 \rightarrow S_1$ or $S_0 \rightarrow S_2$ excitation. The absorption spectrum of azobenzene core displays two bands usually located in the UV-visible region: the most intense band ($\varepsilon \approx 22{,}000$ l mol^{-1} cm^{-1}) corresponds to a symmetry-allowed π–π^* transition (S_2), the less intense corresponds to an n–π^* symmetry-forbidden transition (S_1) (**Figure 2**). The switching mechanism involves a change in molecular physico-chemical characteristics that can be triggered by irradiation at specific wavelengths; in depth a phenyl ring undergoes a rotation of 180° with respect to the CNN' group, giving the molecule a different shape, dimension (a single PhNNPh core measures 9,9 A° in the E form and 5,5 A° in the Z form) (**Figure 3-4**) and dipolar moment.

This spatiotemporal control over molecular motion very quickly became the hinge of most of the research in which azobenzenes are involved. The conversion of azobenzenes from the stable E isomer to the metastable Z isomer is only triggered by light, whereas the reverse can occur photochemically or thermally. Sometimes, the interconversion between the two forms can be visualized with the naked eye as a distinct colour change, whereas in other cases, the difference between the isomers is discernible only by their different absorption spectra.

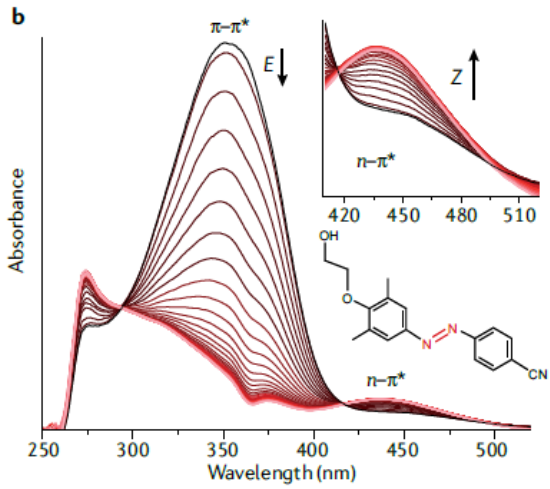

Figure 2. Classic azobenzene core absorption spectrum: the two stereoisomeric forms of azobenzene - E and Z - can be interconverted by light irradiation and/or heat. The π–π* absorption band of the Z isomer is placed at 360-370 nm with a notably decreased intensity when the isomerization occurs, while the n–π* band is placed at 450 nm and slightly increases in intensity when the E isomer produced.

The photoisomerization mechanism of azobenzenes has long been debated [9-12]; many different paths have been hypothesized: torsion about central double bond, inversion at a nitrogen centre and "hula-twist" were considered the most reliable [12] (**Figure 3**). Nowadays is generally accepted that there are different isomerization mechanisms following n–π* or π–π* excitation, depending on the specific characteristic of the analysed azobenzene (**Figure 3-4**). The performance of a switch can be evaluated according to four different parameters. The first of these is the wavelength of maximum light absorption and the quantum yield for the consequent isomerization. The second performance parameter is the relative thermal stability of the two isomers, a parameter that can change greatly among different systems. Indeed, the Z isomers of push-pull or o/p hydroxyl compounds rapidly convert back into their E forms [13-14], while Z isomers in other systems can have appreciable thermal stability [15-16]. The lifetime of the Z form is one of the most important parameters when considering applications in various materials and environments. Lifetimes (τ) or half-lives ($t_{1/2}$) of the Z isomer are usually measured in solution. The nature of the solvent influences the stability of the metastable Z form [17]. Third characteristic parameter of a photoswitch is the steady-state relative abundance of E and Z isomers when the molecule is exposed to a specific light source (or none). It can be expressed as an equilibrium constant, or a ratio referred to the photostationary distribution (PSD) at the photostationary state (PSS). The last parameter concerns the reproducibility of photochemical switching over time [18]. Most of azo compounds exhibit little or no sign of fatigue after several cycles of irradiation, due to the absence of any side reactions. Surface energy levels involved in photoisomerization are described in reference [19].

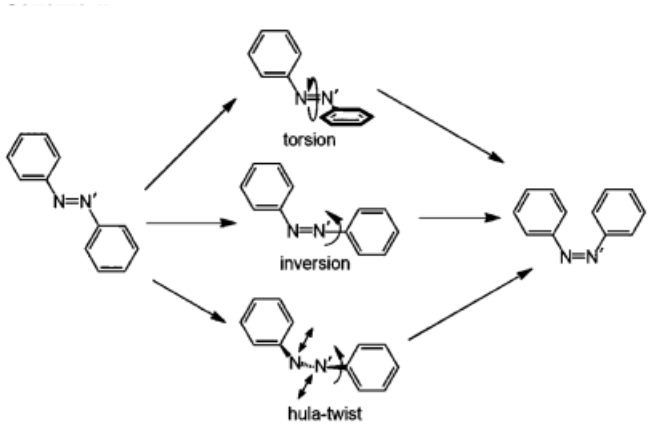

Figure 3. Possible mechanism involved it he conversion from trans to cis isomer: torsion, inversion, hula-twist.

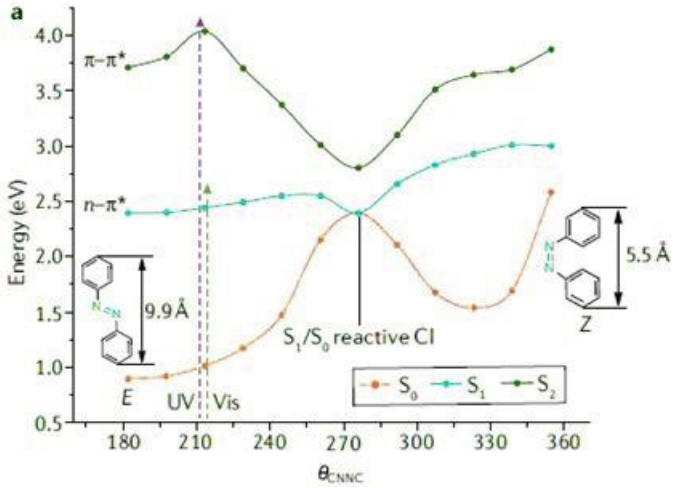

Figure 4. Azobenzene potential energy surface during the photoisomerization scans along fixed values of the θ CNNC torsion coordinate with all other degrees of freedom allowed to relax.

Over the years many azobenzene derivatives have been developed to achieve a better control of their photochemical properties. Indeed, chemical modification of their structure allows access to molecules having a vast chromatic range, from the pigment Yellow 12 to Trypan blue passing through the classic orange; meaning that the tuneable light absorption of azo compounds enables the preparation of species that absorb and consequentially isomerize when exposed to visible, near-IR or UV light [20-21]. Considering the PhNNPh archetype, simply introducing π-donors and π-acceptors substituents, respectively, gives rise to hypsochromic (shorter λmax) and bathochromic (longer λmax) shifts of the main absorption band [22].

Furthermore, by modifying the chemical environment or by inserting heteroatoms on the aromatic rings directly linked to aza group, it is possible to modify the (Z) cis isomer half-life. Adding an hydroxyl group in ortho or para position favours the formation of hydrazone-like intermediates facilitating the rotation around the N=N bond in the transition state (rotational mechanism), consequently leading to a very fast recovery of the (E) trans isomer [23]. The introduction of electron-withdrawing groups, such as cyan or nitro groups, further decreases the relaxation time, due to the additional push–pull electronic effects [24]. Heteroaryl azobenzenes have distinct photophysical and photochemical properties, along with different steric profiles and molecular geometries, the unique characteristics of each one defines half-lives of Z isomer (**Figure 5**) [25-26].

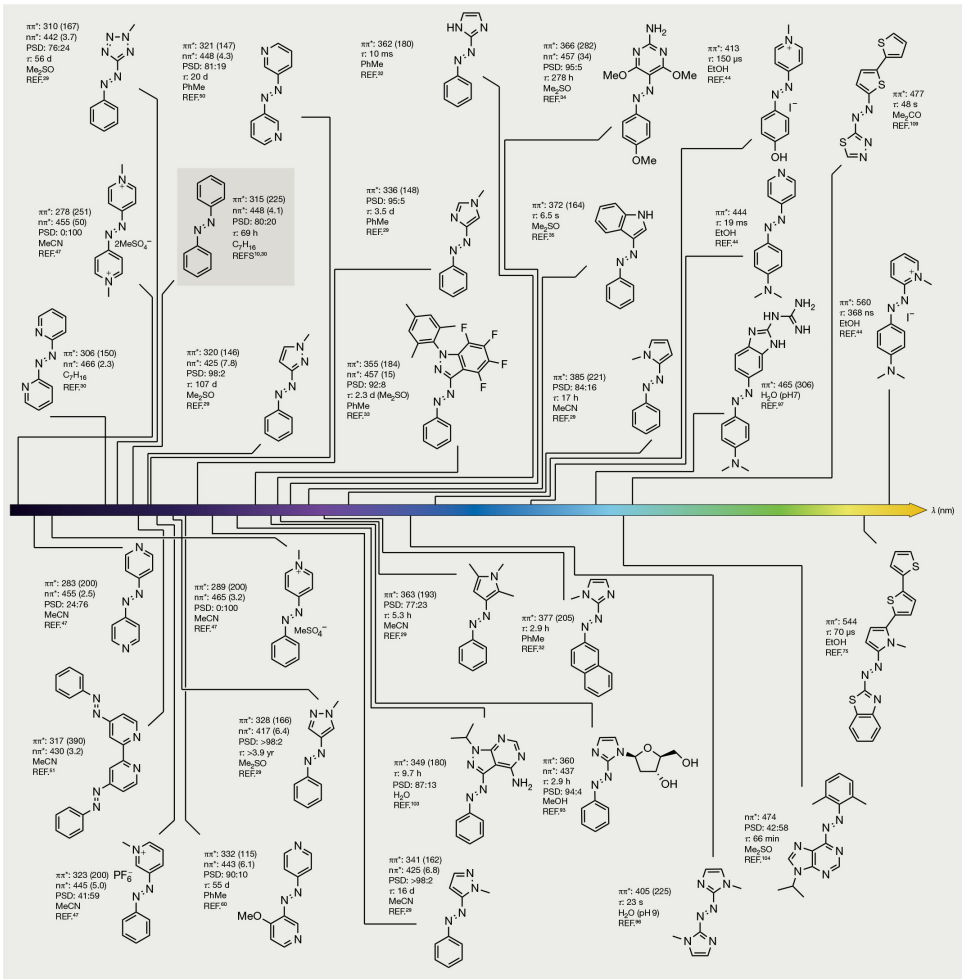

Figure 5. Different cis isomer half-life and the absorption spectrum in AZOs containing heteroaryl atoms: modifying the chemical composition of the core is possible to obtain azobenzenes which absorb visible lightand have a very fast thermal return to the trans isomer. Partially reproduced from [26].

Synthesis methods

Over the years, to obtain a wide range of azobenzenes with multiple characteristics, various synthesis methods have been developed. Most azobenzenes are obtained via azo coupling reaction, this method is based on the initial diazotization of an aromatic primary amine at low temperature, afterwards the obtained diazonium salts reacts with an activated electron rich aromatic nucleophile. Those reactions are usually fast and occur in high yields. Diazonium salts are weak electrophiles that react with electron rich species, in this case with substituted arenes carrying electron donor groups like amine or hydroxy. Usually, this substitution reaction takes place at the para position to the electron donor group on the activated aromatic ring, acting as a nucleophile. When this position is already occupied, the substitution occurs at the ortho position (**Figure 6**).

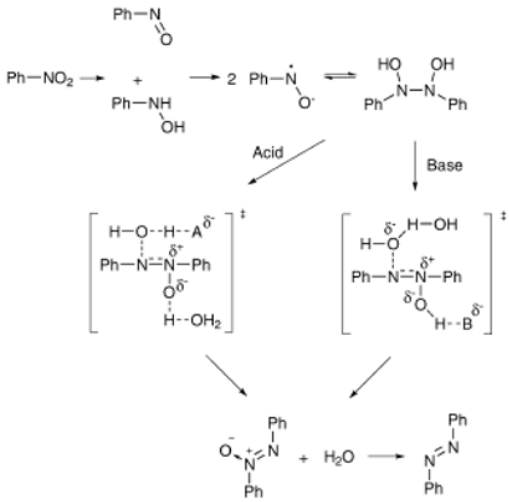

Figure 6. Scheme of classic diazocopoulation reaction.

Mills reaction [27] leads to azobenzenes synthesis starting from an aromatic nitroso derivate and an aniline, the reaction is carried out in glacial acetic acid. One of the most efficient ways to form nitrosoarenes from anilines is a two-phase heterogeneous system like Oxone ($2KHSO_5$, $KHSO_4$, K_2SO_4) in H_2O/CH_2Cl_2; these biphasic systems ensure the separation of the generally less water-soluble nitroso compounds from the N-arylhydroxylamine intermediates and aniline precursors, preventing undesirable condensation reactions and leading to good yields. The mechanism of this reaction involves the nucleophilic attack of aniline on the nitroso derivative and leads to azobenzene after dehydration of the intermediate. (**Figure 7**). A handy method to synthesize symmetrical azo compounds is the reductive coupling of aromatic nitro derivates: most used reducing reagent are $LiAlH_4$, $NaBH_4$, sodium 2-hydroxy ethoxide in ethylene glycol, KOH, Zn/NaOH, Bi, Bi-KOH, or Pb/HCO_2NH_4. Yields range from 60 to 95%. The mechanism proposed for these reductive couplings is the reduction of nitro compounds in the presence of the base or acid shown. Thus, the nitro aromatic compound reacts with the reductant leading to a mixture of the nitroso derivative and the corresponding hydroxylamine. Later both are converted into radical anions that couple to generate a N–N bond leading to the gem-dihydroxy intermediate. Dehydration of this intermediate is the single-rate determining step to form the azoxy compound: the departure of the proton and hydroxide ion, in either acid or basic media, is probably assisted by molecules of water. The resulting azoxy compound is reduced to give the azo compound (**Figure 8**).

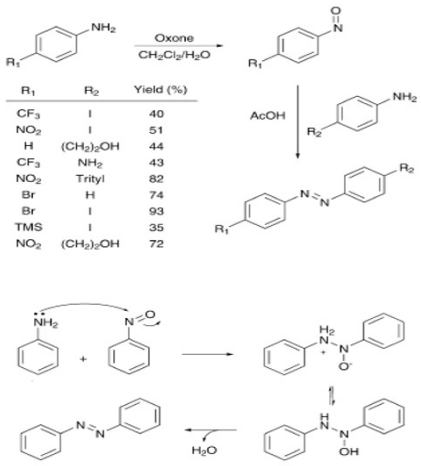

R_1	R_2	Yield (%)
CF_3	I	40
NO_2	I	51
H	$(CH_2)_2OH$	44
CF_3	NH_2	43
NO_2	Trityl	82
Br	H	74
Br	I	93
TMS	I	35
NO_2	$(CH_2)_2OH$	72

Figure 7. Scheme of Mills reaction.

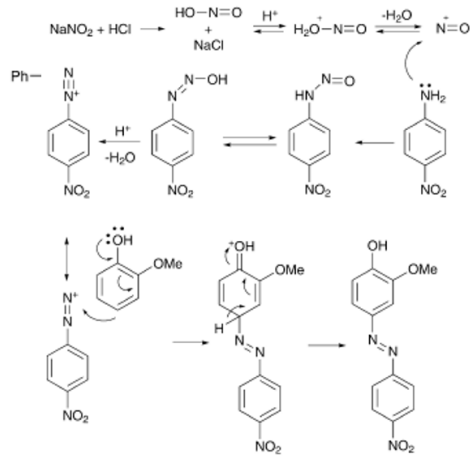

Figure 8. Scheme of reductive coupling of aromatic nitro derivates.

One more method of synthesis is the oxidation of anilines; in most cases this process gives moderate-low yields. The reaction involves the N–N coupling of an initially formed cation radical, which is produced by an one-electron transfer, followed by a two-electron oxidation of the resulting hydrazobenzene to form the corresponding azobenzene. Azobenzene can also be obtained from azoxybenzenes, these compounds can undergo the Wallach reaction or simply be reduced to obtain the desired product. Some other synthetic methods that deserve a mention are dehydrogenation of arylhydrazines and triazene rearrangement [27].
All reactions are summarized in **Figure 9**.

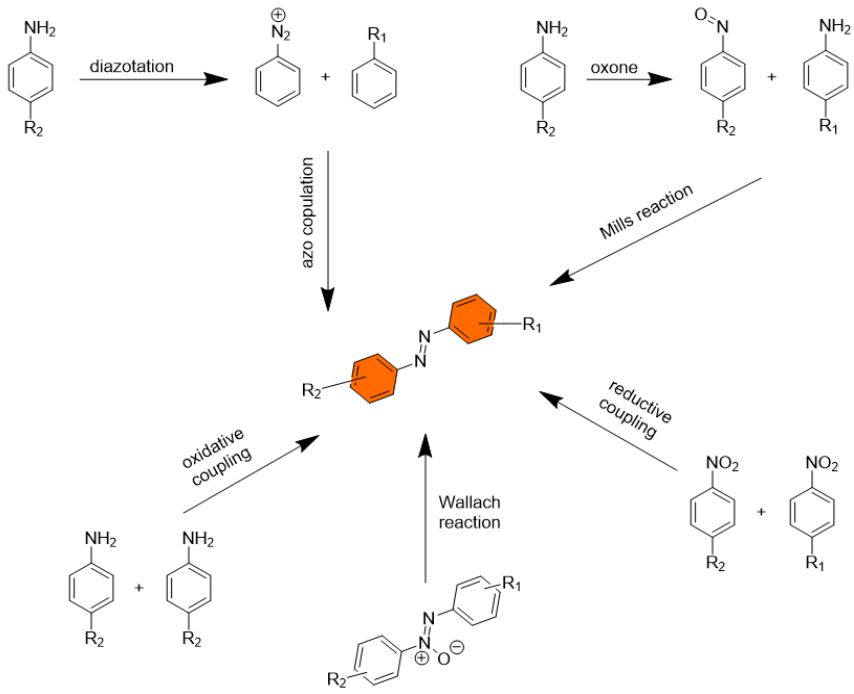

Figure 9 Different path of synthesis of azobenzenes: diazocopulation, Mills reaction, Wallach reaction, reductive coupling, oxidative coupling.

Azobenzenes based liquid crystals

In the past 15 years most notable advances involving azobenzene have emerged: the incorporation of azobenzenes has enabled the fabrication of photoresponsive polymers and other materials with macroscopic properties that can be externally manipulated by light with excellent temporal and spatial control. In particular, azobenzenes were used as cores of thermotropic liquid crystals, making it possible to synthesize photoresponsive liquid crystal networks (LCN) and liquid crystal elastomers (LCE). To better understand the function of azobenzenes within these polymers it is necessary to introduce liquid crystals (LC). LC have one (or more) intermediate mesophase between the solid crystalline and the isotropic liquid phases: in those states materials maintain the fluid-like ability to flow and have low density but preserve the orientational order and anisotropy of crystals. Typically, LC have specific molecular geometries, referred to as rod-like, discotic, banana-like or bowl-like. For LCN/LCE materials, rod-like shapes are the most common. Rod-like LC consist typically of a central core (composed of one or more cyclical moieties) bonded to two aliphatic tails of various lengths. In rod-like LC monomers based on azobenzenes the core is represented by the general formula ArNNAr, and is functionalized in opposite positions by aliphatic chains carrying polymerizable end groups **(Figure 10)**.

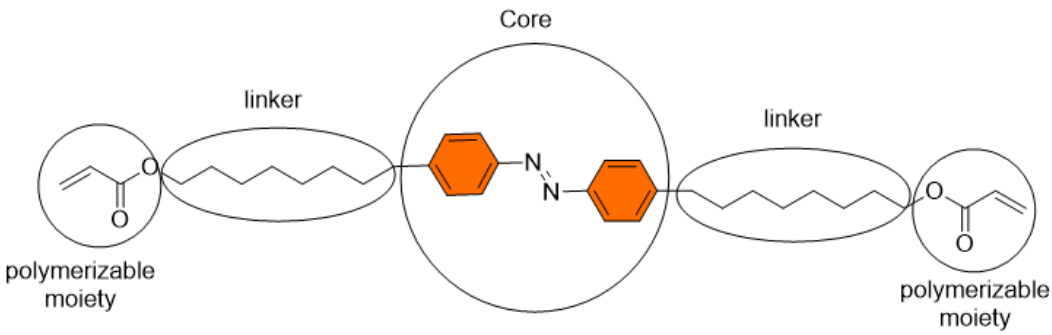

Figure 10. An azobenzene based liquid crystal monomer: the core is represented by the rigid PhNNPh group, bonded to two flexible aliphatic tails ended with acrylate polymerizable group.

LC can show multiple mesophases, within these the arrangement of the molecules is different (**Figure 11**).

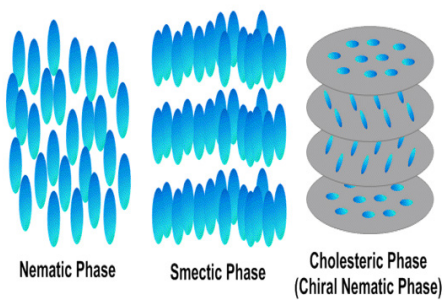

Figure 11. Different arrangements of different LC molecules depending on temperature.

- Nematic: a nematic mesophase consists of molecules packed without any positional order and characterized only by a common preferential orientation. The axis resulting from the mean preferential orientation of the molecules is called the director.
- Nematic Cholesteric: in the cholesteric mesophase, the presence of chiral intermolecular interactions causes each molecule to remain misaligned by some degree with respect to those that surround it; hence the orientation of the molecules is not constant throughout the phase but the director follows a helical trend. Since these misalignments are generally temperature dependent, the pitch of the helix also varies with temperature. This property is of particular importance since the cholesteric mesophases can selectively reflect the fraction of visible light which has a wavelength proportional to the pitch.
- Smectic: the smectic mesophase is characterized by a molecular order higher than the nematic one. In addition to possessing a preferential orientation, the molecules are in fact ordered in superimposed planes, packed in autonomous layers. Within each layer, the molecules move freely as in a normal fluid but have great difficulty in passing from one layer to the next.

By modifying the chemical environment or the structure of the liquid crystals, one mesophase can be favored over another: for example, adding a kink in the core (e.g. a methyl group) disfavours the smectic phase and promotes the nematic.
While LC are in any of these mesophase they can be oriented using different techniques such as use of specific alignment layers [28] (**Figure 12**), application of electric or magnetic fields [29], stretching [30] or by flow using different methods [31-32]. The LC alignment can be fixed in a polymeric structure if molecular units have polymerizable end-groups. Depending on the crosslink density of the polymer, Liquid Crystal elastomers (LCEs) or liquid crystal networks (LCNs) can be obtained. LCEs have low crosslink densities, hence glass transition temperatures (Tg) are typically below room temperature making them behave as rubbers, while LCNs have a Tg above room temperature and behave like glassy solids. LCNs are typically crosslinked through one-step radical polymerisation (triggered by thermal or photochemical initiators) carried out in a cell, which allows the use of alignment layers to direct the molecular organization (**Figure 12**). LCEs usually have a flexible backbone that give the material viscous properties at RT. In this case stretching or flow orienting techniques are preferred (**Figure 13-14**).

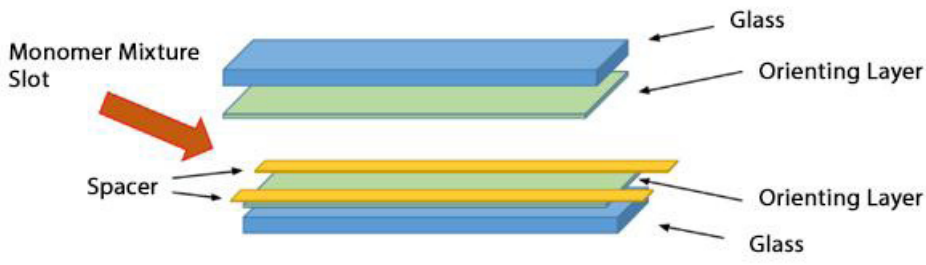

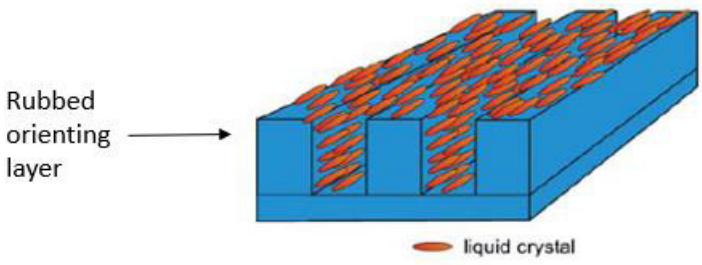

Figure 12. Classic polymerisation cell set-up: two flat glasses are covered by an orienting layer by spincoating, the glasses are coupled and air gap is left between them using a spacer. The gap is filled with the liquid crystal mixture by capillarity.

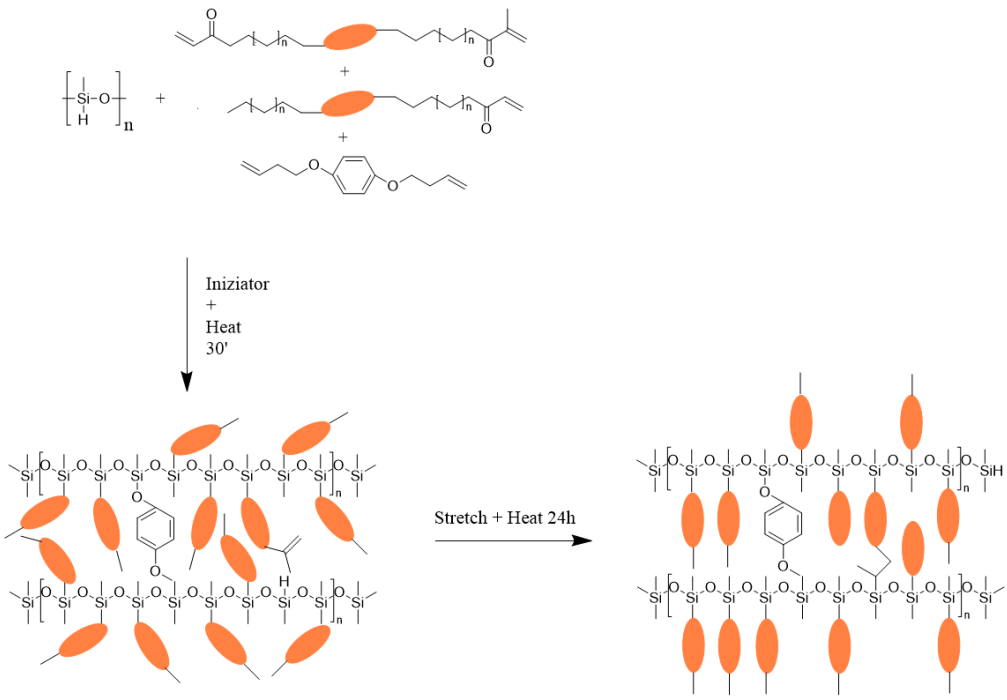

Figure 13. Two-step polymerisation: exploiting the different reactivity between acrylates and methacrylates groups is possible to carry out a first fast polymerisation of a mixture obtaining a rubbery liquid crystal polymer that can be stretched and fixed in a steady shape by a subsequent longer polymerisation.

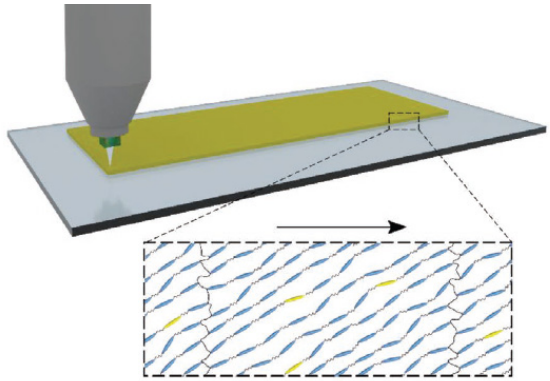

Figure 14. Liquid crystal oligomers can be oriented by flow with a 3D printer and subsequently polymerized to obtain an LCE. Reproduced from [56].

LCEs have continuous alignment driven by stretching or flow direction while LCN may have both uniform or non-uniform alignment throughout the thickness of the polymer. Most common uniform LC alignments are planar and homeotropic, while splay (**Figure 15**) and twisted nematic are non-uniform alignments.

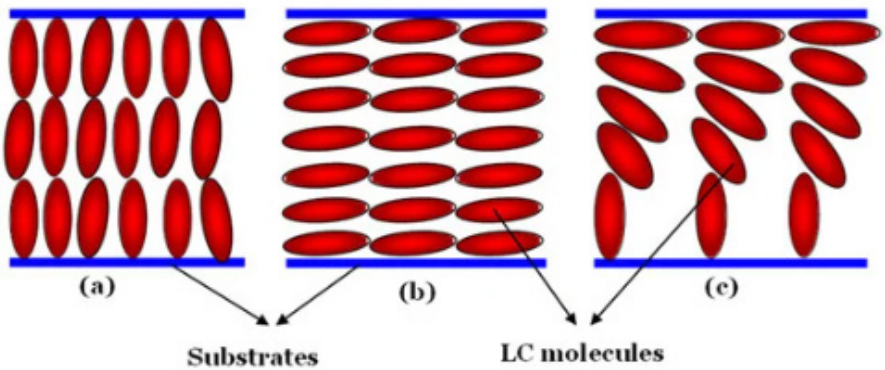

Figure 15. In homeotropic (a) and planar (b) alignments, LC molecules are uniformly oriented either perpendicular or parallel to the top and bottom polymer film surfaces respectively, splay (c) is a gradual transition between planar and homeotropic alignments throughout the sample thickness.

LCPs (liquid crystal polymers) show anisotropic proprieties, which are extremely interesting for actuators triggered by external stimuli such as light, temperature and electric fields, because this allows to control the direction of their expansion and their bending. Whereas LCE can undergo broad deformations even at room temperature due to their rubbery nature, large deformations in LCNs are driven by a temperature increase, which leads to a transition from LC phase to the disordered isotropic phase: this causes a large uniaxial contraction (up to 400%) along the molecules director. For LCNs, thermally driven deformations can be amplified by utilizing non-uniform alignments such as splay, in which the different molecular orientation of the two sides of the film amplifies the anisotropic volume expansions and induce larger macroscopic deformations [33]. Incorporating azobenzenes into a polymer leads to the conversion of the absorbed light energy into heat and mechanical work [34].

Azobenzene derivatives can be exploited to trigger the actuation by indirectly heating the polymer network through light absorption, working as photothermal agent: in this case the azobenzene units are usually not crosslinked with the other monomers but are dispersed in the network. Current literature suggests that the photoactuation of azobenzene-containing LCNs is triggered from combined photothermal and photomechanical effects. Photothermal effects include isomerization-driven heating and network photo-softening, which are responsible for the large decrease in storage modulus (much larger than the thermal-softening of glassy polymers) [35-37]. Photomechanical effects occur due to the molecular dimension change upon isomerization, from E to Z isomer, leading to molecular order disruption [38-39]and network pull effect [40]. LC azobenzene monomers can be inserted into LCPs as side chains, crosslinkers or main chain components. Single polymerizable endtail monomers (SPEM) (**Figure 16**) work as side chain while those with two or more polymerizable endtails (PPEM) perform the other roles (**Figure 17**).

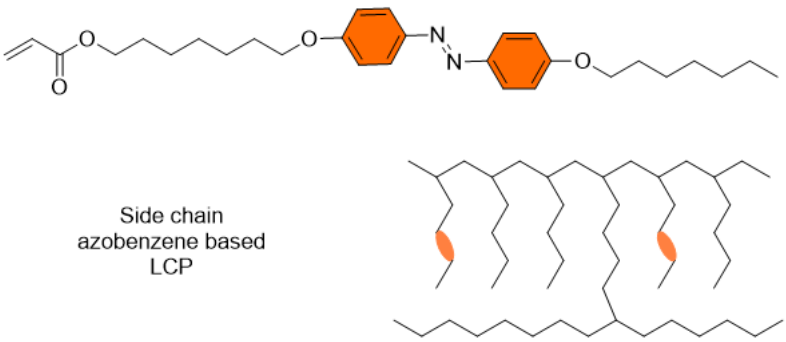

Figure 16. Single polymerizable end-tail molecules exploited as side chain monomers in liquid crystals polymers.

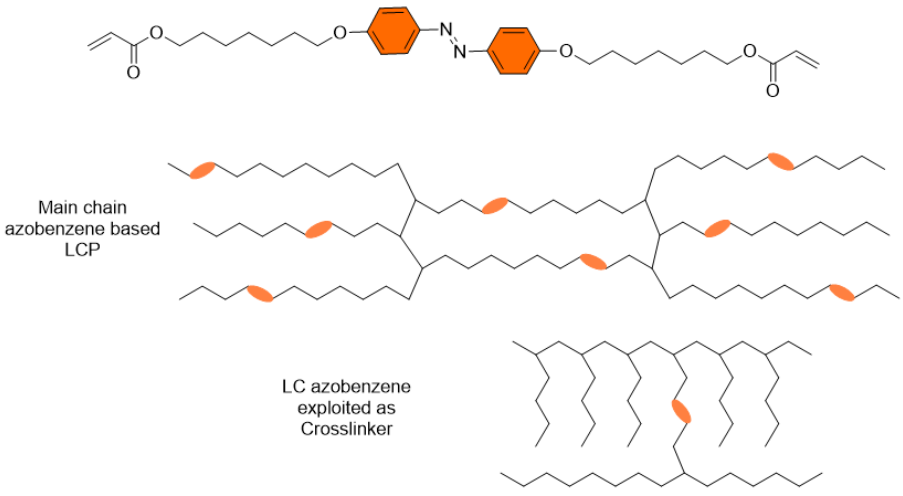

Figure 17. Multiple polymerizable end-tail monomers can work both as crosslinker or backbone in liquid crystals polymers.

The return to the original shape of polymers containing exclusively SPEM is not affected by half-life times of azobenzenes cis form, since photoresponsive chromophores are not included in the crosslinker or in the main chain and do not exercising a network pull action. Whereas SPEM induce almost exclusively photothermal actuation of a polymer when irradiated, PPEM also lead to the photomechanical one. Hence, PPEM has a higher actuation efficiency when compared to SPEM, due to a constructive contribution between photochemical and photothermal effects in the actuation mechanism. Furthermore, polymers in which PPEM are included can be actuated in different environments, such as water, thanks to their independence from thermal phenomena [41] (**Figure 18**).

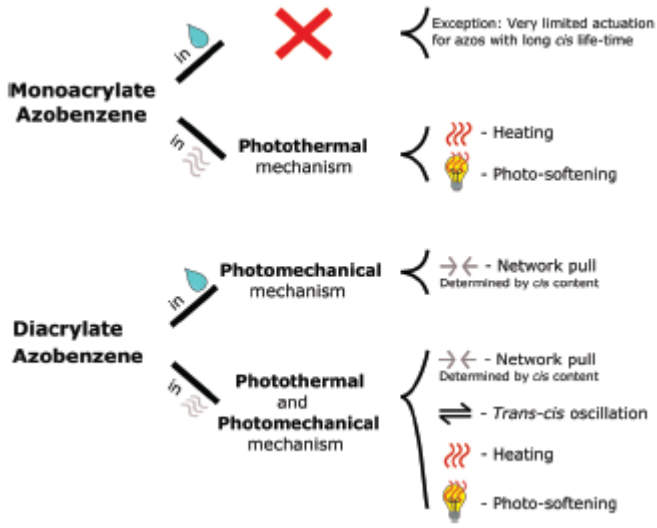

Figure 18. Different properties of single polymerizable end-tail monomers (monoacrylate) and poly polymerizable end-tails monomers (diacrylate). Reproduced from [41].

Photoresponsive Liquid Crystal actuators

At the beginning of the current century, liquid crystalline azobenzoic monomers began to be introduced into polymers. The first was Finkelmann in 2001, who developed a two-step polymerization method to obtain oriented LCE starting from polymerizable azobenzene [42]. Photoresponsive LCNs were described by Ikeda, who polymerized a mixture of azo monomers inside cells delimited by specially treated layers [43,44,45]. The interest of the scientific community in these materials that use azobenzene as molecular switches grew rapidly and many groups began to use azobenzenes as dopants for their polymers. Those studies show actuators, triggered by discontinuous light source, able to swim into the dark [46] or acting like snails [47] and caterpillars [48] (**Figure 19**). Light-driven actuators are not restricted to dry environments, although those operating underwater are rarely reported. In fact, most of these actuators use photothermal dyes SPEM, which upon light absorption heat the LCE above the nematic to isotropic transition temperature, triggering a fast and local anisotropic contraction, utilized to power the locomotion. Those films usually start flat with a fixed molecular alignment, and are restricted to just one way of actuation, such as simple bending. Afterwards, shape and motion programmable light responsive actuators were developed, greatly increasing freedom in the

design of azobenzene LC-based soft robots. One approach to achieve motion programmability utilizes light of specific wavelengths to choose the type of deformation in LCNs containing two types of chromophores, achieving photo-rewritable programming of light-driven actuators [49]. Another paper reports a light-responsive PET/LCN bilayer that can be thermally fixed in a mold and thereafter modified in shape using different wavelengths [50]. A reconfigurable actuator was developed through selective decrosslinking, obtaining a film that is patterned with active and inert regions [51] (**Figure 20**).

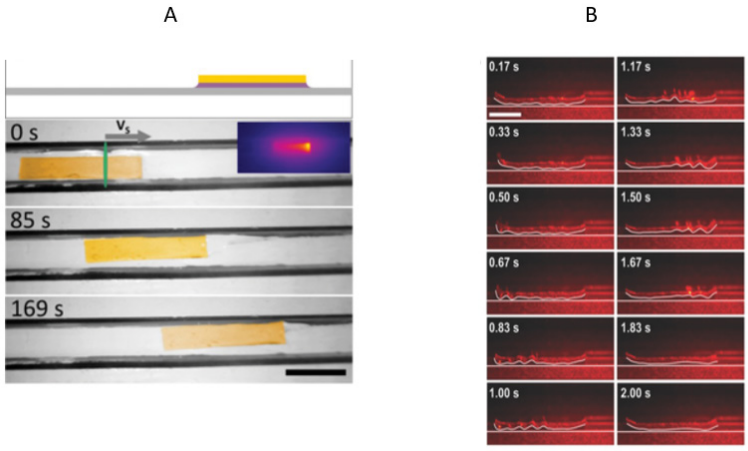

Figure 19 First Azo-based LCP actuation. A) stripes of LCN acting like snail depending on the irradiated portion B) stripes of LCN acting like caterpillar when irradiated. Copyright A): Reproduced with permission,[47] Copyright 2016, Wiley VCH. B) Reproduced with permission, [48] Copyright 2016, Wiley VCH.

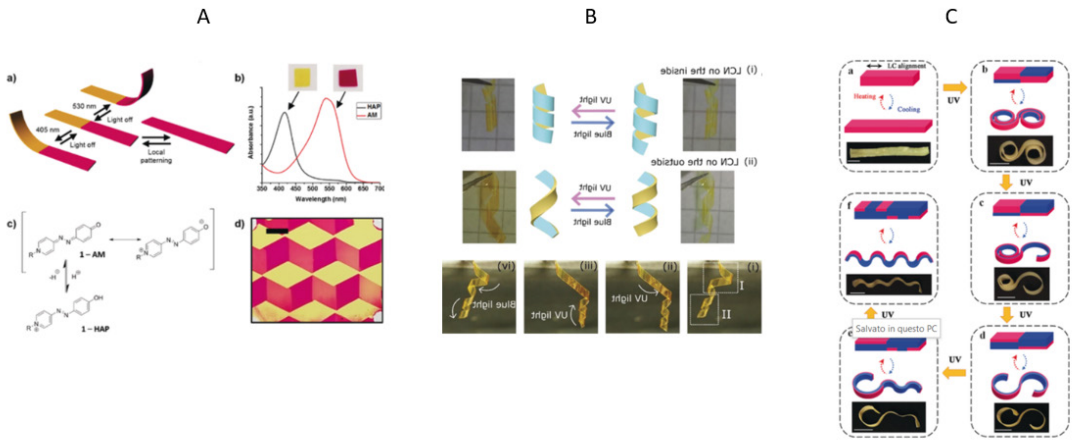

Figure 20. Programmable light responsive actuator. A) Azo based LCN composed by chromophores absorbing at different wavelength B) light-responsive PET/LCN bilayer that can be thermally fixed in a mold and thereafter modified in shape using different wavelengths C) film patterned with active and inert regions. A) Reproduced with permission,[49] Copyright 2017, Wiley VCH. D, B) Reproduced with permission,[50] Copyright 2020, Wiley VCH C) Reproduced with permission,[51] Copyright 2020, Wiley VCH.

During the past years devices and polymers triggered by a continuous light beam were also developed; these change their shape or position constantly until the light is switched off. The work that pioneered those actuators shows the light-driven oscillation of liquid crystal cantilevers having planar molecular orientation upon exposure to constant high intensity light beam. The mechanism for such oscillations commonly relies of the photothermal and photomechanical deformation of the LCP to move the material into and out of the light beam, leading to a high frequency oscillation [52]. Later, devices showing a continuous locomotion were developed. Among those we find a four-blade light-driven plastic mill based on hydrazone liquid-crystal networks [53] or a splay-oriented film mimicking waves motion [54] (**Figure 21**). A key point in the functioning mechanism of the previously mentioned actuators is the orientation of the LC material. All the materials cited so far were obtained through orientation techniques such as polymerization in cells with orienting layers or stretching. In recent years, additive manufacturing has proved to be an excellent way to control molecular orientation and create photoresponsive devices [55-57] (**Figure 22**). These papers show how direct 3D printing of inks consisting of liquid crystalline oligomers is a powerful method for creating photoresponsive LCEs that can be triggered in different environments and integrated with other materials. Many examples of actuators similar to those described in this thesis can be consulted in the following reviews [58-59]. There are no references in the literature that show the coupling of these polymers with other materials for the development of multifunctional devices.

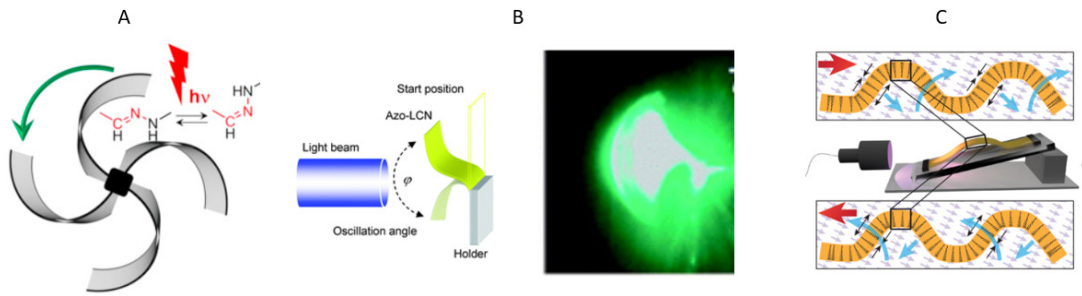

Figure 21. Azo based LCP triggered by continuous irradiation. A) Rotating four-blade light-driven plastic mill B) high frequency oscillation cantilever C) splay oriented LCP stripes mimic waves motion. copyright A) Reproduced with permission,[53] Copyright 2017, Elsevier. B) reproduced from [52], C) Reproduced with permission,[54] Copyright 2017, Nature Publishing Group.

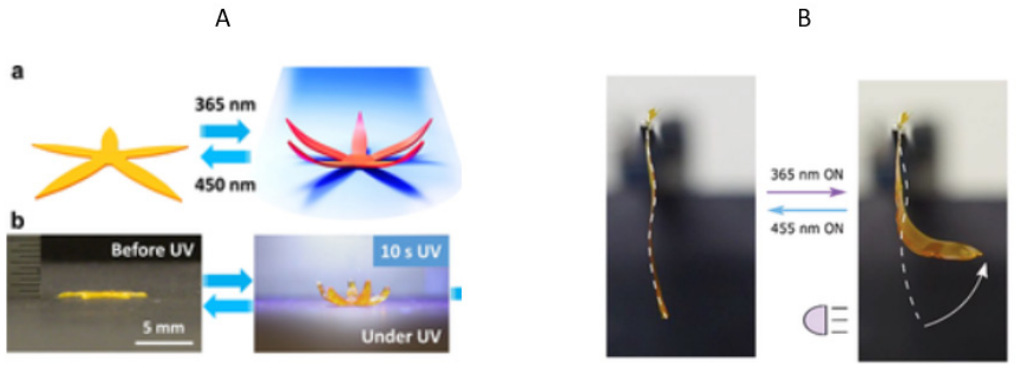

Figure 22. Azobased liquid crystal actuator obtained through addictive manufacturing. A) UV light triggered starfish B) Planar oriented amphibious actuator A) Reproduced with permission [55] Copyright 2020, Wiley-VCH B) Reproduced under the terms of the Creative Commons CC BY license [56].

Moisture and Light responsive Liquid Crystal Polymers

Nowadays research is focusing on the development of multiple stimuli-responsive actuators for soft-robotics; that kind of devices can perform multiple roles, undergoing different motions when triggered by different stimuli. Few examples of actuators reactive both to moisture and irradiation are described in literature, all of them are influenced both by supramolecular interactions and photoresponsive moieties. Yu et Al. developed a LCN which bent in orthogonal directions when triggered by either humidity or light [60], while Wani OM designed a humidity-sensitive, splay aligned LCN device containing both azobenzenes dyes and acid dimeric LC monomers: the presence of both photoresponsive and humidity sensitive moieties makes the actuator to respond to light only when environmental humidity is high, showing how a secondary trigger can be a controller on the photoactuation [61] (**Figure 23**). This is the only reported actuator, in which supramolecular interactions have an impact on the photo response of the LCP. Many supramolecular polymers have been described, but none of these contains LCs [62,63]. Photoresponsive azobenzene based LCP actuators in which the supramolecular structure of the chromophore influences the actuator has not been described yet.

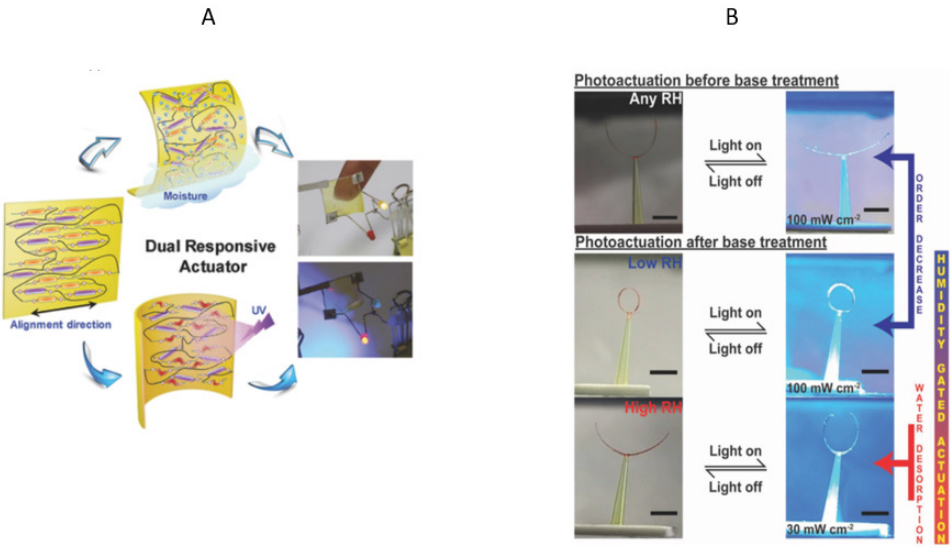

Figure 23. Azo based multi-stimuli responsive Materials. A) LCN triggered by either humidity or light. B) LC azo based actuator responding to light only when environmental humidity is high. A) reproduced with permission Copyright 2016 [61], Wiley VCH. B) Reproduced with permission,[62] Copyright 2019, Wiley VC.

Photoresponsive LCP coupled with other materials

To exploit the characteristics of azo-based LCPs, they have been coupled with other materials to manufacture devices capable of performing various roles in soft robotics. Most of those devices act as carriers to move objects [64-65]: a bilayer actuator consisting of a light responsive LCN and a magnetic responsive polydimethylsiloxane (PDMS) composite was used as a multi-stimuli triggered transporter [66], an amphibious device composed of a magnetically driven stem and a light-driven gripper was assembled to carry objects underwater and transport them to a defined place. Through magnetically driven motion, the polyp induces stirring and attracts suspended targets. The light responsive gripper is sensitive to low light intensities and has programmable states and rapid and highly controlled actuation, allowing the device to capture or release targets on demand with wireless control [67] (**Figure 24**). At least a bilayer photoresponsive sensor able not only to bend but also to reflect selectively green light was obtained via DIW (direct ink writing) [58]. Devices containing azobenzenes for converting light energy into electrical energy have not been reported yet.

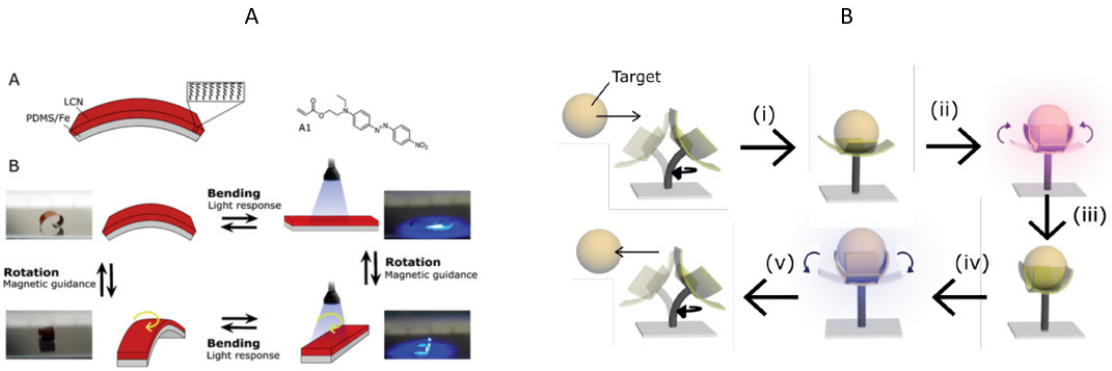

Figure 24. Examples of photoresponsive polymers coupled with other material to perform as carrier in soft robotics. A) bilayer actuator consisting of a light responsive LCN and a magnetic responsive polydimethylsiloxane B) amphibious device working as a wireless octopus. A) Reproduced with permission,[64] Copyright 2018, Wiley VCH. B) Reproduced with permission,[65] Copyright 2010, Royal society of Chemistry.

More advanced opportunities in azobenzenes word are described in reference [68].

Research aim and thesis outline

The aim of the thesis was to explore the exciting world of azobenzene to develop a device able to transform the light energy not only in the classic mechanical energy but also in electric current. To reach this goal many polymers described in literature [52,54,55] have been reproduced and coupled with piezoelectric materials with poor results. Many other novel polymers, obtained through different polymerisation ways, has been synthetised and tested. A "Proof of principle" was first obtained using a planar oriented LCN, in which well-known azobenzenes monomers described in **Figure 16-17** were exploited as chromophores, afterwards the polymer wascoupled with a PVDF piezoelectric material. The device was triggered by UV light and had a very low efficiency; therefore the polymer was modified adding chromophores that absorb visible light and the liquid crystal orientation was changed into splay. Results are described in **Chapter 2**.
Furthermore, innovative techniques for the production of LCEs were explored. During the abroad period at TU/e (University of the Technology, Eindhoven, SFD research group) DIW through a 3D printer was exploited to fabricate an innovative bilayer device which assumes different shapes when triggered by different stimuli and able to perform in different environments. The device is described in **Chapter 3**. Electrospinning was also explored as a method for the orientation of liquid crystals. Few references were found in the literature concerning this innovative technique. The first attempts had the aim of orienting mixtures of liquid crystals - presenting their mesophase a at room temperature - inside inert matrix. Those experiments failed because of the low density of those mixtures, now the work is focusing on liquid crystal oligomer in which the azo-chromophore is included in the main chain. Electrospinning led to the manufacture of an high efficiency artificial muscle made of an shape memory matrix and doped with a push-pull azobenezene. This device is described in **Chapter 4.**

References

[1] Mitscherlich, E. (1834). Ueber das Stickstoffbenzid. Annalen der Pharmacie, 12(3), 311-314.

[2] Domagk, G. (1935). Ein Beitrag zur Chemotherapie der bakteriellen Infektionen. Deutsche MedizinischeWochenschrift, 61(7), 250-253.

[3] Hartley, G. S. (1937). The cis-form of azobenzene. Nature, 140(3556), 281-281.

[4] Beharry, A. A., & Woolley, G. A. (2011). Azobenzene photoswitches for biomolecules. Chemical Society Reviews, 40(8), 4422-4437.

[5] Jerca, F. A., Eliseeva, S. V., Gromov, S. P., & Kuz'mina, L. G. (2018). Polymer and Photonic Materials Towards Biomedical Breakthroughs. In J. Van Hoorick, J. Raes, H. Thienpont, & J. Van Erps (Eds.), Springer.

[6] Besson, E., Mehdi, A., Lerner, D. A., Reyé, C., & Corriu, R. J. P. (2005). Photoresponsive ordered hybrid materials containing a bridged azobenzene group. Journal of Materials Chemistry, 15(8), 803-809.

[7] Khayyami, A., & Karppinen, M. (2018). Reversible photoswitching function in atomic/molecular-layer-deposited ZnO: azobenzene superlattice thin films. Chemistry of Materials, 30(16), 5904-5911.

[8] Kanj, A. B., Müller, K., & Heinke, L. (2018). Stimuli-responsive metal-organic frameworks with photoswitchable azobenzene side groups. Macromolecular Rapid Communications, 39(24), 1700239.

[9] Schultz, T., Quenneville, J., Levine, B., Toniolo, A., Martínez, T. J., Lochbrunner, S., ... & Stolow, A. (2003). Mechanism and dynamics of azobenzene photoisomerization. Journal of the American Chemical Society, 125(27), 8098-8099.

[10] Henzl, J., Mehlhorn, M., Gawronski, H., Rieder, K. H., & Morgenstern, K. (2006). Reversible cis-trans isomerization of a single azobenzene molecule. Angewandte Chemie International Edition, 45(4), 603-606.

[11] Salzmann, I., & Dörfler, U. (2001). Theoretical study on the photoisomerization of azobenzene. The Journal of Chemical Physics, 115(16), 7503-7510.

[12] Quick, M., Dobryakov, A. L., Gerecke, M., Richter, C., Berndt, F., Ioffe, I. N., Granovsky, A. A., Mahrwald, R., Ernsting, N. P., & Kovalenko, S. A. (2014). Photoisomerization Dynamics and Pathways of trans- and cis-Azobenzene in Solution from Broadband Femtosecond Spectroscopies and Calculations. J. Phys. Chem. B, 118(29), 8756-8771.

[13] Vela, S., & Corminboeuf, C. (2020). The Photoisomerization Pathway(s) of Push-Pull Phenylazoheteroarenes. Chem. Eur. J., 26(63), 14724-14731.

[14] Garcia-Amorós, J., Sánchez-Ferrer, A., Massad, W. A., Nonell, S., & Velasco, D. (2010). Kinetic study of the fast thermal cis-to-trans isomerisation of para-, ortho-, and polyhydroxyazobenzenes. Phys. Chem. Chem. Phys., 12(45), 13238-13242.

[15] Dokić, J., Kleinschmidt, M., Nalbach, M., Kovalenko, S. A., & Ernsting, N. P. (2009). Quantum chemical investigation of thermal cis-to-trans isomerization of azobenzene derivatives: substituent effects, solvent effects, and comparison to experimental data. J. Phys. Chem. A, 113(25), 6763-6773.

[16] Knie, C., Weiss, C. K., Mena-Osteritz, E., Yushchenko, O., Ruhlmann, L., Rück-Braun, K., Braun, K. R., & Görls, H. (2014). ortho-Fluoroazobenzenes: Visible Light Switches with Very Long-Lived Z Isomers. Chem. Eur. J., 20(54), 16492-16501.

[17] Bandara, H. M. D., & Burdette, S. C. (2012). Photoisomerization in Different Classes of Azobenzene. Chem. Soc. Rev., 41(5), 1809-1825.

[18] Siewertsen, R., Kathan, M., Schmittel, M., & Görller-Walrand, C. (2009). Highly Efficient Reversible Z-E Photoisomerization of a Bridged Azobenzene with Visible Light through Resolved S1 ($n\pi^*$) Absorption Bands. J. Am. Chem. Soc., 131(43), 15594-15595.

[19] Yu, J. K., Bannwarth, C., Liang, R., Hohenstein, E. G., & Martínez, T. J. (2020). Nonadiabatic Dynamics Simulation of the Wavelength-Dependent Photochemistry of Azobenzene Excited to the $n\pi^*$ and $\pi\pi^*$ Excited States. Journal of the American Chemical Society, 142(49), 20680-20690.

[20] Knie, C., et al. (2014). Ortho-fluoroazobenzenes: Visible light switches with very long-lived Z isomers. Chemistry - A European Journal, 20, 16492-16501.

[21] Beharry, A. A., Sadovski, O., & Woolley, G. A. (2011). Azobenzene photoswitching without ultraviolet light. Journal of the American Chemical Society, 133, 19684-19687.

[22] Brown, E. V., & Granneman, G. R. (1975). Cis-trans isomerism in the pyridyl analogs of azobenzene. Kinetic and molecular orbital analysis. Journal of the American Chemical Society, 97, 621-627.

[23] Garcia-Amorós, J., et al. (2018). Activation volumes for cis-to-trans isomerisation reactions of azophenols: A clear mechanistic indicator? Physical Chemistry Chemical Physics, 20, 1286-1292.

[24] García-Amorós, J., & Velasco, D. (2012). Recent advances towards azobenzene-based light-driven real-time information-transmitting materials. Beilstein Journal of Organic Chemistry, 8, 1003-1017.

[25] Weston, C. E., Richardson, R. D., Haycock, P. R., White, A. J. P., & Fuchter, M. J. (2014). Arylazopyrazoles: Azoheteroarene photoswitches offering quantitative isomerization and long thermal half-lives. Journal of the American Chemical Society, 136, 11878-11881.

[26] Crespi, S., Simeth, N. A., & König, B. (2019). Heteroaryl azo dyes as molecular photoswitches. Nature Reviews Chemistry, 3, 133-146.

[27] Merino, E. (2011). Synthesis of azobenzenes: The coloured pieces of molecular materials. Chemical Society Reviews, 40, 3835-3853.

[28] Nishikawa, M. (2000). Design of polyimides for liquid crystal alignment films. Polym. Adv. Technol., 11, 404-412.

[29] Nakano, S., Mizukami, M., & Kurihara, K. (2014). Effect of confinement on electric field induced orientation of a nematic liquid crystal. Soft Matter, 10, 2110-2115.

[30] Nishikawa, M. (2000). Design of polyimides for liquid crystal alignment films. Polym. Adv. Technol., 11, 404-412.

[31] Sol, J. A. H. P., Sentjens, H., Yang, L., Grossiord, N., Schenning, A. P. H. J., & Debije, M. G. (2021). Photogenerating work from polymers. Advanced Materials, 33, 2103309.

[32] Bertocchi, M. J., Ratchford, D. C., Casalini, R., Wynne, J. H., & Lundin, J. G. (2018). Electrospun Polymer Fibers Containing a Liquid Crystal Core: Insights into Semiflexible Confinement. J. Phys. Chem. C, 122(29), 16964–16973.

[33] Mol, G. N., Harris, K. D., Bastiaansen, C. W. M., & Broer, D. J. (2005). Thermo-mechanical responses of liquid-crystal networks with a splayed molecular organization. Adv. Funct. Mater., 15, 1155–1159.

[34] Koerner, H., White, T. J., Tabiryan, N. V., Bunning, T. J., & Vaia, R. A. (2008). Photogenerating work from polymers. Mater. Today, 11(7–8), 34-42.

[35] Vapaavuori, J., Laventure, A., Bazuin, C. G., Lebel, O., & Pellerin, C. (2015). Submolecular Plasticization Induced by Photons in Azobenzene Materials. J. Am. Chem. Soc., 137, 13510.

[36] Kumar, K., Schenning, A. P. H. J., Broer, D. J., & Liu, D. (2016). Regulating the modulus of a chiral liquid crystal polymer network by light . Soft Matter, 12, 3196.

[37] Harrison, J. M., Goldbaum, D., Corkery, T. C., Barrett, C. J., & Chromik, R. R. (2015). Nanoindentation studies to separate thermal and optical effects in photo-softening of azo polymers . J. Mater. Chem. C, 3, 995.

[38] Harris, K. D., Cuypers, R., Scheibe, P., van Oosten, C. L., Bastiaansen, C. W. M., Lub, J., & Broer, D. J. (2005). Large amplitude light-induced motion in high elastic modulus polymer actuators. J. Mater. Chem., 15, 5043.

[39] Liu, D., & Broer, D. J. (2015). New insights into photoactivated volume generation boost surface morphing in liquid crystal coatings. Nat. Commun., 6, 8334.

[40] Sánchez-Ferrer, A., & Finkelmann, H. (2011). Opto-Mechanical Effect in Photoactive Nematic Side-Chain Liquid-Crystalline Elastomers. Macromol. Rapid Commun., 32, 671.

[41] Pilz da Cunha, M., van Thoor, E. A. J., Debije, M. G., Broer, D. J., & Schenning, A. P. H. J. (2019). Unravelling the photothermal and photomechanical contributions to actuation of azobenzene-doped liquid crystal polymers in air and water. Journal of Materials Chemistry C, 7, 13502-13509.

[42] Finkelmann, H., Nishikawa, E., Pereira, G. G., & Warner, M. (2001). A new opto-mechanical effect in solids. Physical Review Letters, 87, 015501.

[43] Ikeda, T., Nakano, M., Yu, Y., Tsutsumi, O., & Kanazawa, A. (2003). Anisotropic bending and unbending behavior of azobenzene liquid-crystalline gels by light exposure. Advanced Materials, 15, 201-205.

[44] Yamada, M., Kondo, M., Miyasato, R., Naka, Y., Mamiya, J. I., Kinoshita, M., Shishido, A., Yu, Y., Barrett, C. J., & Ikeda, T. (2009). Photomobile polymer materials—various three-dimensional movements. Journal of Materials Chemistry, 19, 60-62.

[45] Yu, Y., Nakano, M., & Ikeda, T. (2003). Directed bending of a polymer film by light. Nature, 425, 145.

[46] Camacho-Lopez, M., Finkelmann, H., Palffy-Muhoray, P., & Shelley, M. (2004). Fast liquid-crystal elastomer swims into the dark. Nature Materials, 3, 307-310.

[47] Rogóż, M., Dradrach, K., Xuan, C., & Wasylczyk, P. (2019). A millimeter-scale snail robot based on a light-powered liquid crystal elastomer continuous actuator. Macromolecular Rapid Communications, 40, 1900279.

[48] Rogóż, M., Zeng, H., Xuan, C., Wiersma, D. S., & Wasylczyk, P. (2016). Light-driven soft robot mimics caterpillar locomotion in natural scale. Advanced Optical Materials, 4, 1689-1694.

[49] Gelebart, A. H., Mulder, D. J., Vantomme, G., Schenning, A. P. H. J., & Broer, D. J. (2017). A rewritable, reprogrammable, dual light-responsive polymer actuator. Angewandte Chemie International Edition, 56, 13436-13439.

[50] Verpaalen, R. C. P., Pilz da Cunha, M., Engels, T. A. P., Debije, M. G., & Schenning, A. P. H. J. (2018). Liquid crystal networks on thermoplastics: Reprogrammable photo-responsive actuators. Angewandte Chemie International Edition, 57, 15580-15584.

[51] Jiang, Z.-C., Xiao, Y.-Y., Tong, X., & Zhao, Y. (2019). Selective Decrosslinking in Liquid Crystal Polymer Actuators for Optical Reconfiguration of Origami and Light-Fueled Locomotion. Chemistry-A European Journal, 25(23), 5332-5337.

[52] Serak, S., Tabiryan, N., Vergara, R., White, T. J., Vaidya, R. D., & Bunning, T. J. (2010). Liquid crystalline polymer cantilever oscillators fueled by light. Soft Matter, 6(4), 779-783.

[53] Vantomme, G., Gelebart, A. H., Broer, D. J., & Meijer, E. W. (2017). A four-blade light-driven plastic mill based on hydrazone liquid-crystal networks. Tetrahedron, 73(33), 4963-4967.

[54] Gelebart, A., Mulder, D. J., Varga, M., Konya, A., Janes, D. W., Voets, I. K., & Broer, D. J. (2017). Making waves in a photoactive polymer film. Nature, 546(7657), 632-636.

[55] Lu, X., Ambulo, C. P., Wang, S., Rivera-Tarazona, L. K., Kim, H., Searles, K., & Ware, T. H. (2021). 4D-Printing of Photoswitchable Actuators. Angewandte Chemie International Edition, 60(10), 5536-5543.

[56] del M., M., Liu, L., Pilz da M., Broer, D. J., & Schenning, A. P. H. J. (2020). Direct Ink Writing of a Light-Responsive Underwater Liquid Crystal Actuator with Atypical Temperature-Dependent Shape Changes. Advanced Functional Materials, 30(25), 2005560.

[57] Pozo, M. D., Sol, J. A. H. P., van Uden, S. H. P., Peeketi, A. R., Lugger, S. J. D., Annabattula, R. K., Schenning, A. P. H. J., & Debije, M. G. (2021). Patterned Actuators via Direct Ink Writing of Liquid Crystals. ACS Applied Materials & Interfaces, 13(49), 59381-59391.

[58] Huang, Y., Yu, Q., Su, C., Jiang, J., Chen, N., & Shao, H. (2021). Light-Responsive Soft Actuators: Mechanism, Materials, Fabrication, and Applications. Actuators, 10(11), 298.

[59] Sun, D., Zhang, J., Li, H., Shi, Z., Meng, Q., Liu, S., Chen, J., & Liu, X. (2021). Toward Application of Liquid Crystalline Elastomer for Smart Robotics: State of the Art and Challenges. Polymers (Basel), 13(11), 1889.

[60] Liu, Y. Y., Xu, B., Sun, S. T., Wei, J., Wu, L. M., Yu, Y. L. (2017). Humidity- and Photo-Induced Mechanical Actuation of Cross-Linked Liquid Crystal Polymers. Adv. Mater., 29, 1604792.

[61] Wani, O. M., Verpaalen, R., Zeng, H., Priimagi, A., & Schenning, A. P. H. J. (2019). An Artificial Nocturnal Flower via Humidity-Gated Photoactuation in Liquid Crystal Networks. Adv Mater, 31.

[62] Baroncini, M., Ragazzon, G., Silvi, S., Venturi, M., & Credi, A. (2015). The eternal youth of azobenzene: new photoactive molecular and supramolecular devices. Pure and Applied Chemistry, 87(6), 537-545.

[63] Fuentes, E., Gerth, M., Berrocal, J. A., Matera, C., Gorostiza, P., Voets, I. K., Pujals, S., & Albertazzi, L. (2019). An Azobenzene-Based Single-Component Supramolecular Polymer Responsive to Multiple Stimuli in Water. Journal of the American Chemical Society, 141(38), 15076-15084.

[64] Lu, X., Zhang, H., Fei, G., Yu, B., Tong, X., Xia, H., & Zhao, Y. (2018). Liquid-Crystalline Dynamic Networks Doped with Gold Nanorods Showing Enhanced Photocontrol of Actuation. Adv Mater, 30,

[65] Cheng, F., Yin, R., Zhang, Y., Yen, C.-C., & Yu, Y. (2010). Fully plastic microrobots which manipulate objects using only visible light. Soft Matter, 6(14), 3447-3449.

[66] Pilz da Cunha, M., Foelen, Y., Engels, T. A. P., Papamichou, K., Hagenbeek, M., Debije, M. G., & Schenning, A. P. H. J. (2019). Light-Controlled Morphing of Liquid Crystalline Polymer Networks. Advanced Optical Materials, 7(2), 1801604.

[67] Pilz da Cunha, M., Kandail, H. S., den Toonder, J. M. J., & Schenning, A. P. H. J. (2020). An artificial aquatic polyp that wirelessly attracts, grasps, and releases objects. Proceedings of the National Academy of Sciences of the United States of America, 117(30), 17571-17577.

From light to electric energy:
a novel photoresponsive device

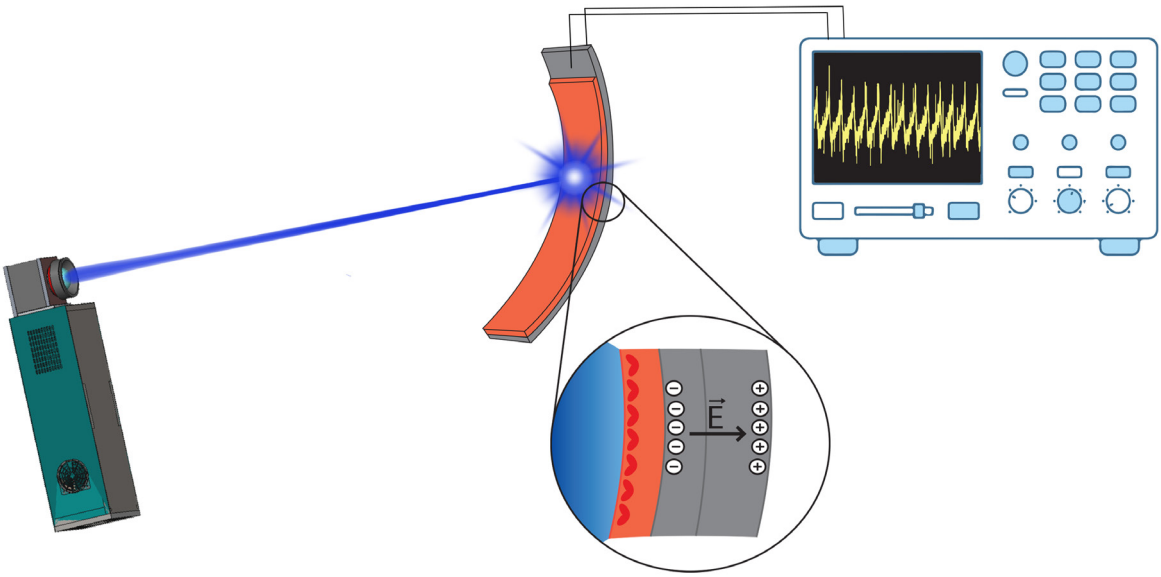

This project was carried out in collaboration with Stefano Masiero.

Introduction

Research in the field of photoresponsive polymers is very active, as these materials are capable of transforming light energy into mechanical energy (or chemical or heat) through a change in their shape [1]. The deformation in these polymers is driven by molecules that undergo a nanoscale change in their dimensions [2], which leads to macroscopic activation of the material.
Azobenzene(AZO)-based actuators are of particular interest for their rapid response and for the reproducibility of their deformation without showing any sign of fatigue. AZOs undergo a reversible photoinduced isomerization between their trans and cis configurations when irradiated at specific wavelengths: this causes an alteration of their physico-chemical properties as well as a change of their shape, in particular a drastic reduction of their length [3-4]. By functionalization of the azobenzene core, one can modulate some properties of the chromophore, such as the cis form life-time [5] and the wavelength needed to induce the photoisomerization [6]. When AZO moieties are included -even at low percentages- as monomers in the production of polymeric materials the change of dimension driven by trans to cis photoisomerization at the molecular level leads to a macroscopic deformation of the polymer shape.
In this context, AZOs often constitute the rigid core of liquid crystalline monomers: during the years many azo-containing liquid crystals networks (LCNs) and liquid crystal elastomers (LCEs) have been developed to obtain materials with uniaxial deformation. These polymers have been exploited to manufacture devices that can perform multiple roles in soft robotics and industry, ranging from artificial muscles to wireless carriers [7-15]. In this context, visible-light-photoswitchable AZO compounds are the most interesting materials for the development of photoresponsive devices [16]. Herein, an AZO-containing blue-light triggered LCN has been developed and coupled with a piezoelectric material, to obtain a novel device able to transform visible light into electrical energy.

Methods and materials

Compounds **3, 4** and 2-[ethyl(phenyl)amino]ethan-1-ol are commercially available.

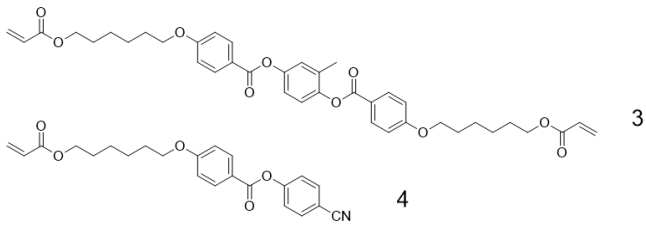

3

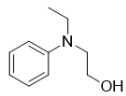

4

α and **β** were synthetised following the literature procedure [17]. N-ethyl-N-hydroxy ethyl aniline was coupled with nitroaniline to synthetize **DR1** through a diazo coupling reaction. The alcoholic function of DR1 was made to react with acryloyl chloride to obtain the monoacrylate monomer **1** (**Scheme 1**).
Trihydroxyazobenzene core was synthesized through a classic diazo-copulation reaction between resorcin and p-hydroxyaniline, diacrylate azobenzene monomer **2** was obtained via nucleophilic substitution between trihydroxyazobenzene and the acrylate ended tails **5** (**Scheme 2**).

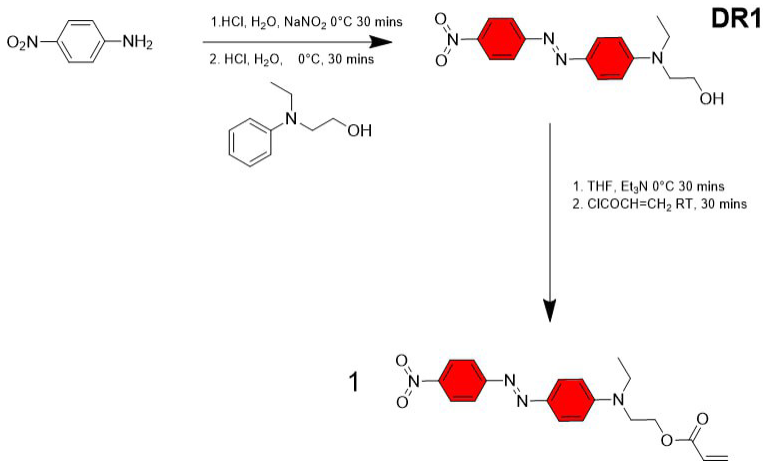

Scheme 1. Synthesis scheme of **1.**

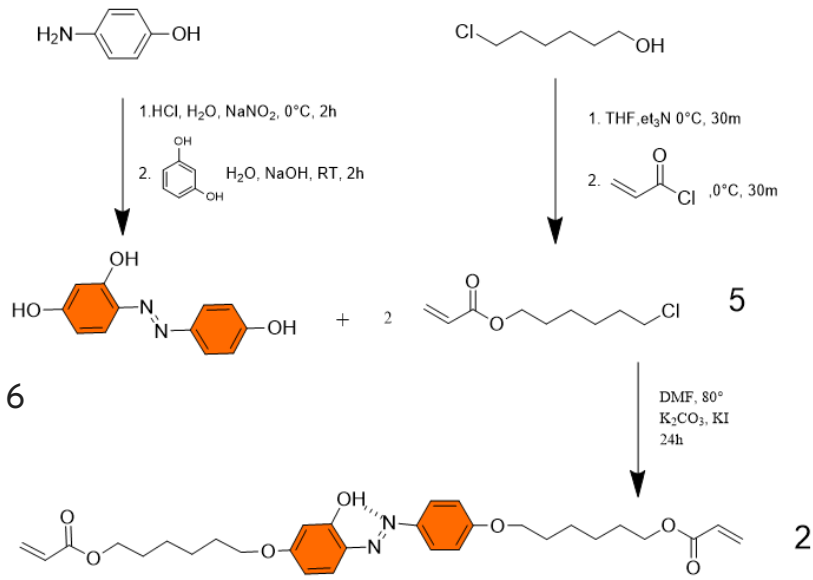

Scheme 2. Synthesis scheme of **2.**

In our first attempts, a well-known [18] UV light triggered LCN obtained by copolymerization of monofunctional azo monomer **α** and azo crosslinker **β** (**Scheme 3**) was employed as photo-active component of the device described below. Results were poor in terms of voltage produced compared to the intensity of the radiant light used.

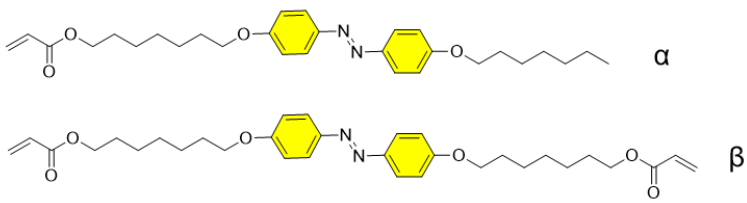

Scheme 3. Chemical structure of monomers **α** and **β.**

In light of that, azo-based monomers **1** and **2**, copolymerized with non-photoactive structural monomers **3** and **4** (**Scheme 4**), were chosen to obtain a blue-light triggered LCN with fast actuation, high network pull force and fast shape recovery.

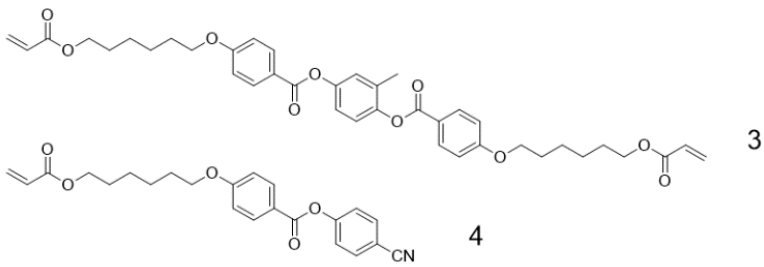

Scheme 4. Chemical structure of monomers **3** and **4.**

Both photoresponsive monomers have their π-π* absorption band encompassing the blue region of the spectrum as shown in **Figure 1.** Moreover, they both have short cis-form half-life [19]. Side-chain monomer **1** presents electron-donating/withdrawing substituents in the para positions of the azobenzene core, thus behaving as a push-pull azobenzene [6] with low nπ*/ππ* vertical excitation energy and a fast thermal return from cis to trans isomer. **1** has an high molar extinction coefficient (see below) and acts as a fully photothermal-driven photo-switch: the heat released by its cis–>trans isomerization triggers the actuation of the polymer. Crosslinker **2** belongs to the azo-phenols category [20-21] and it was chosen to exploit both photothermal and photomechanical contributions, with the purpose of giving the polymer an improved actuation efficiency [22]. Because of its fast thermal return, **2** does not fix the polymer in a bent mold after photoisomerization, allowing it to quickly recover the starting shape, contrary to what happened in previous experiments with β as cross linker **(Figure 3)**.

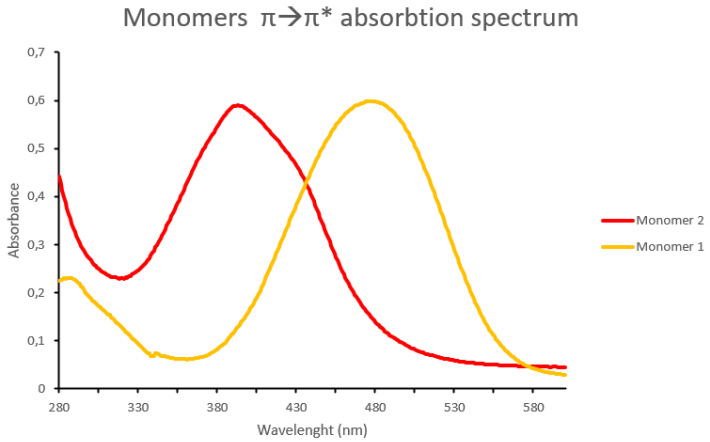

Figure 1. Absorption spectrum of ππ* band of the azobenzene monomers **1-2** (monomer 2 band is normalized 1:3).

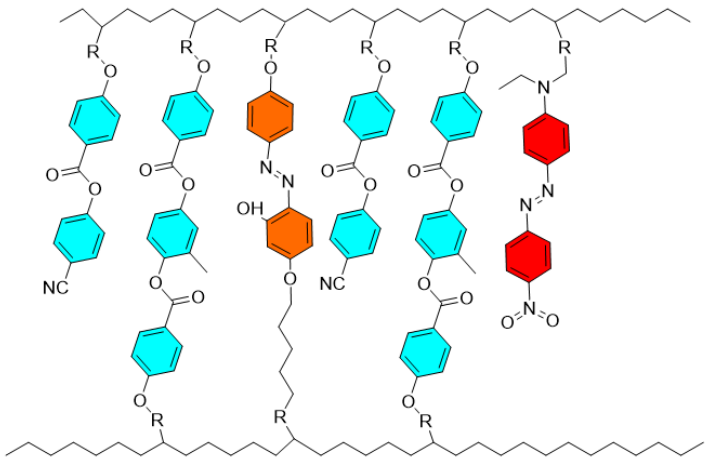

Figure 2. Stylized representation of the polymer / polymer concept. **1-2** represent the photoactive portion and are exploited respectively as side chain and crosslinker monomers. **3-4** are exploited as inert matrix.

Monomers **3** and **4** were used as non-photoactive components of the LCN as shown in **Figure 2**. The polymerisation mixture was composed of **1** 2 mol% (1,9 mg), **2** 3 mol% (2,9 mg), **3** 38,5 mol% (42,3 mg) **4** 56,5 mol% (102,9 mg) and initiated by 3 mg of photoiniziator Irgacure 784. Monomers were dissolved together in 2 mL of DCM, sonicated and subsequently the solvent was removed under nitrogen flow in the dark.
The polymerization was carried out in custom-made cells obtained by clamping together a glass plate, carrying a rubbed PVA layer, and a clean, uncoated glass plate previously treated with plasma to make it more hydrophilic. Two stripes of kapton (20 μm thickness) were used to control the spacing between the glass plates. Consequently, all the LCN samples used for the experiments have a thickness of 20 μm. This set-up was chosen with the purpose of obtaining a splay alignment of the liquid crystalline material, which is known to lead to larger deformation, as compared to uniaxial alignment, owing to the expansion and shrinkage that takes place on the opposite sides of the LCN film [23]. The cells were placed on a hot plate controlled by a thermocouple at 95 °C and were filled with the molten polymerisation mixture by capillary action. At this temperature the monomers mixture is isotropic. Once the cells were totally filled, the temperature was decreased to reach the nematic phase, at 75 °C. The polymerization was performed at this temperature for about 24 h; during the first 2 hours cells were flipped every 30 min, while during the last hours were flipped every 8 h. A mercury lamp, equipped with an optical fiber and a cut-off filter (OYA Y52, >500 nm) to avoid premature isomerization of azobenzenes, was used to trigger the photoinitiator. The light intensity during the polymerization was about 10 mW cm^{-2}. After photopolymerization, the film was post-cured at 120 °C for 10 min and slowly cooled to room temperature. Polymeric films were removed from cells using a razor.
Films were weighed to get their initial weight (m0) and then immersed in 15 mL of DCM for 1 h. The samples were then dried under vacuum for 1 h and weighed to determine the residual mass (md). The gel content (G) was then calculated according to Equation 1 and resulted to be 87%:

Equation 1. $G=md/m0 \times 100$

Different mixtures, containing higher percentages of **1** were tested (7%,14%,25% mol, decreasing proportionally % mol of **4**) but recorded gel fractions were lower than 70%; that leads to a melting of the unreacted monomers during the irradiation and a consequential irregular deformation of the polymer. LCN films were checked by polarized optical microscopy (POM) to verify the liquid-crystalline alignment of the material. The thermal properties of the LCN were determined using differential scanning calorimetry. The Tg of the polymer was detected at about 47 ± 2 °C, while thermogravimetric analysis confirmed that the material is stable up to 230°C. Transmission of the films was measured to ensure that light is not going throughout the overall thickness, hence the beam is not able to reach the piezoelectric material placed behind the polymer (see below).
Films were cut as stripes (25 × 5 mm), with the planar alignment director of molecules parallel to the long edge, then were coupled by insulating tape to previously cut piezoelectric PVDF stripes (30 x 5 mm). The piezoelectric film had silver-coated faces for electrical connections (**Figure 3a**). The side with homeotropic orientation was directed towards the piezo while the side with planar orientation towards the light source, to obtain the highest possible deformation (**Figure 3b**). Most of the photoactive film does not come into contact with the piezo: an air gap (**Figure 3c**) was left to dissipate any heat generated by the irradiation limiting as much as possible the influence of temperature oscillations or triboelectric effect on the performances of the piezoelectric film. Other configurations have been tested, but the best results were obtained with the set-up just described.

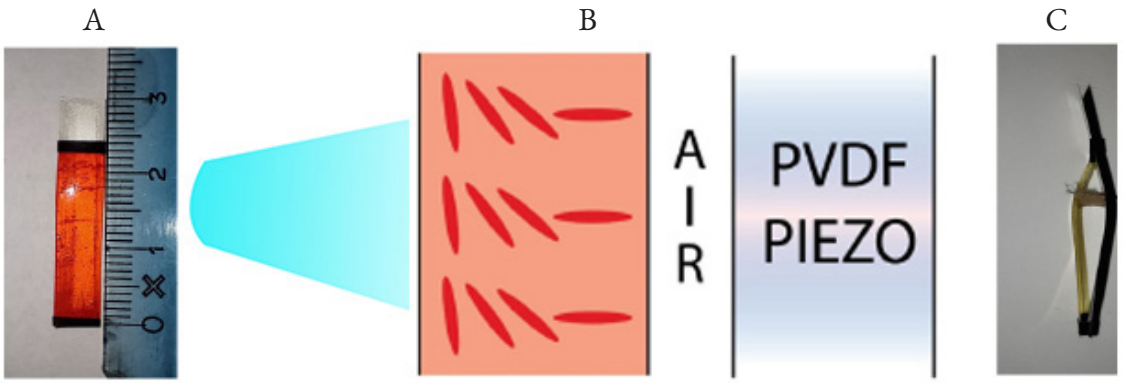

Figure 3. Device morphology a) device size; b) device concept: the planar side is directed towards the light beam to improve bending; c) evidenced air gap between polymer and piezo material.

Actuation and results

The device previously described is designed to produce electric energy exploiting the fast uniaxial bending of the polymer -driven by the photoisomerization of the azobenzenes moieties- that causes a mechanical stress in the piezoelectric material: the dipole alignment of the piezoelectric is thus perturbed and the charge asymmetry generates a potential across the piezoelectric layer [24-25].

The device was hooked, using a home-made clamp equipped with copper electrodes, at a 90 cm distance from the light source in a frontal position. The distance was chosen to allow the laser beam spot to cover the entire width of the polymer strip, the irradiated area turned out to be a circle of 5 mm in diameter. A variable-power 455 nm blue laser was used as the light source. The copper electrodes were connected to an oscilloscope for the detection of the produced voltage. The complete setup is show in **Figure 4**.

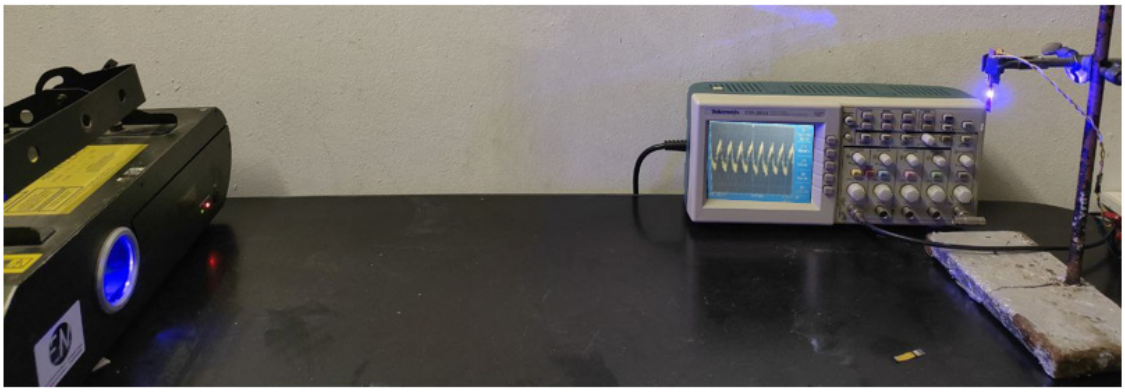

Figure 4. Experimental set-up; from left to right: light source, oscilloscope, polymer-piezo device.

The device was irradiated with a pulsed 455 nm light at different intensities and frequency. Temperature was registered both on the beam-exposed side of the photoactive polymer and on the piezo using a thermal imaging camera. The measurement evidenced a great increase in temperature of the polymer, but the heat generated is dissipated by the air gap between the polymer and the piezoelectric. The temperature of the piezo rises slightly above room temperature during first irradiation pulses and quickly reaches a plateau, remaining constant over time during the experiment. This confirms that voltage production is not driven by the oscillation of the temperature of the piezo. Best results were obtained with a frequency of 3.25 pulses per second (0,15 s pulse followed by 0,15 s relaxation with light off) and an irradiation intensity of 1450 mW cm^{-2}. Under these conditions, the device worked continuously for more than one hour with no decrease of performance. By using longer pulses a higher voltage can be obtained, but only in the first few cycles of irradiation, since prolonged exposure of the film to the light causes a temperature increase (> 300°C), which leads to a partial deterioration of the polymer, and, in turn, to a reduction of the voltage produced in subsequent cycles. On the other hand, lowering the duration of the pulses produces more discharges per second, but with lower intensity, because the bending angle is smaller and the polymer has not enough time to recover the original shape between pulses. Photoactuation was studied by tracking the film's tip vertical displacement under different incident light intensities (at 3.25 pulses per second): the bending angles increase as the intensity of the light increases as shown in **Figure 5**. The temperature reached by the polymer also increases as the intensity of the light increases (**Figure 6**), and the polymer does not return to room temperature in the time interval between two pulses. No actuation was observed when photoactive polymer's temperature was below its Tg (47°C). The voltage produced by the piezoelectric is directly proportional to the bending angle of the azo-containing-polymer and consequentially to the intensity of the incident light as show in **Figure 7**a-b.

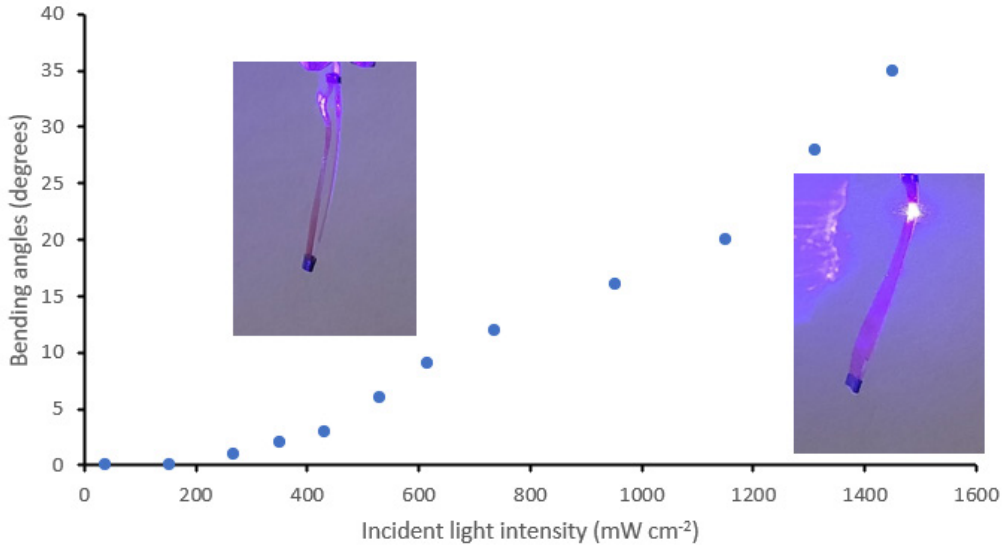

Figure 5. Bending angle vs. incident light intensity. (Inset) Photographs of sample during irradiation at 400 mW cm^{-2} (left) and 1400 mW cm^{-2} (right).

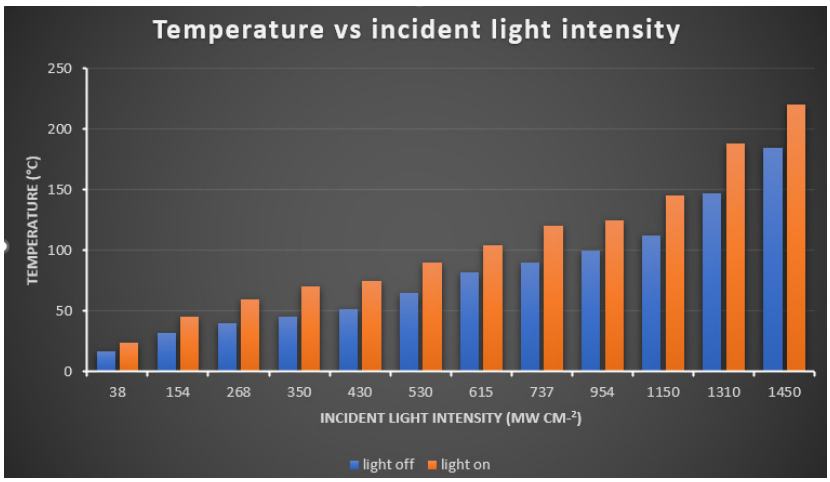

Figure 6. Average temperature reached by the polymer under different irradiation intensities.

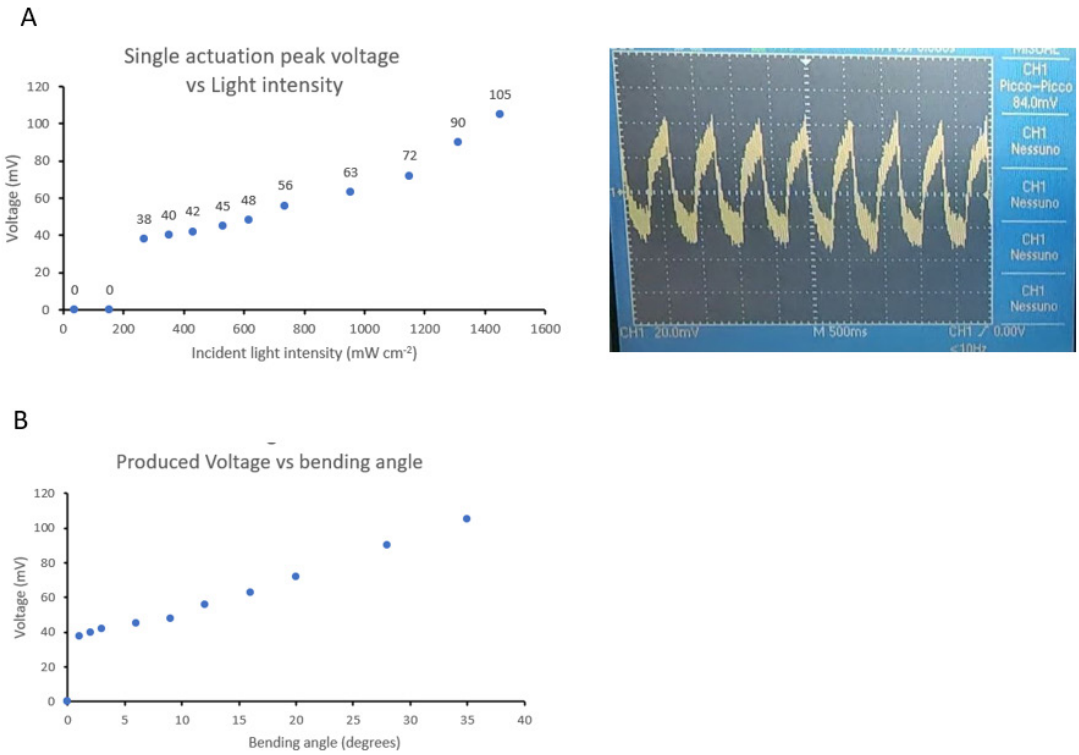

Figure 7. a) Correlation between single-pulse voltage produced and incident light intensity b) bending angles related to voltage produced.

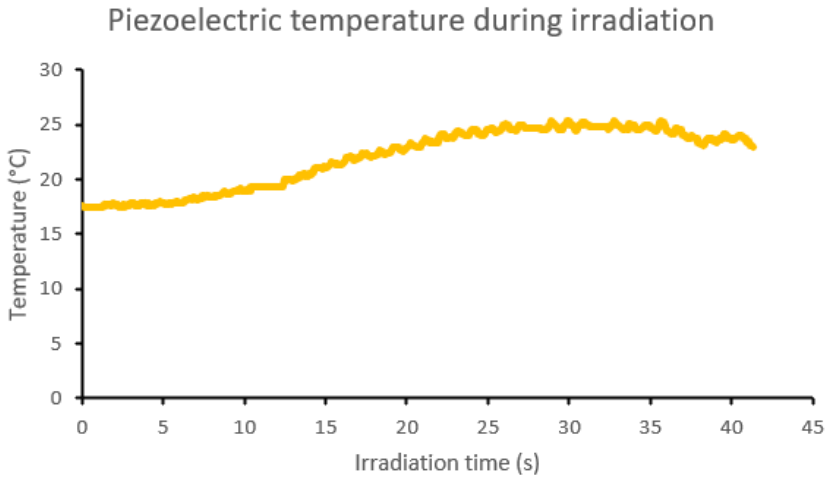

Figure 8. Piezoelectric temperature during irradiation at 1450 mW cm^{-2} 3,25 pulse per second.

A 2.5 Ω resistor was placed between the 2 electrodes to calculate the current generated by the device, intensities in the order of microamperes were recorded when the device was irradiated with a light intensity above 1000 mW cm^{-2} as show in **Figure 9**.

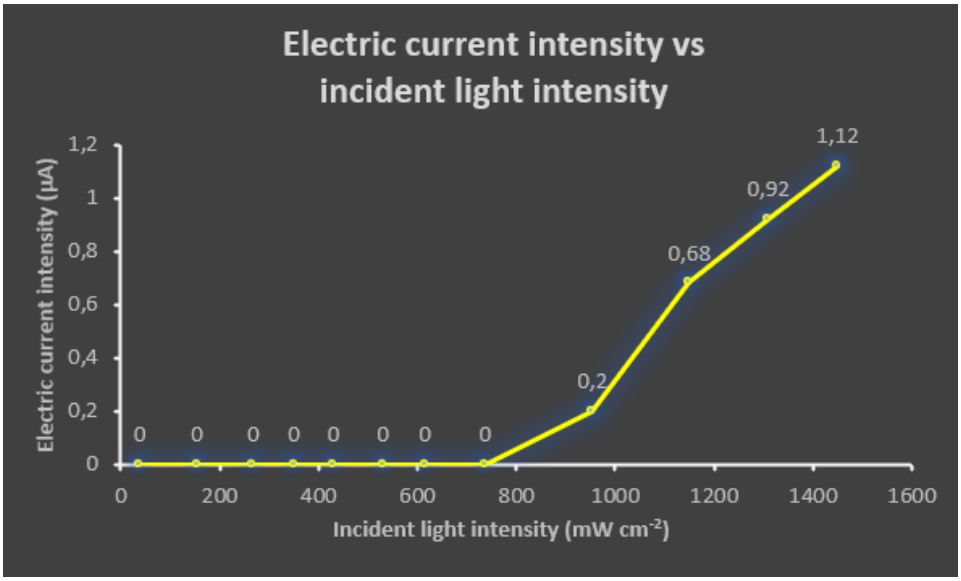

Figure 9. Correlation between current produced and incident light intensity.

The performances of the device were compared with those obtained from a device assembled with an analogus LCN, obtained from **α** and **β** as photoresponsive monomers in place of **1** and **2**. Even when a more powerful UV lamp with a longer pulse duration was used, the voltage produced by the latter device was significantly lower (**Figure 10**). Moreover, under those conditions, the device was damaged after few pulses.

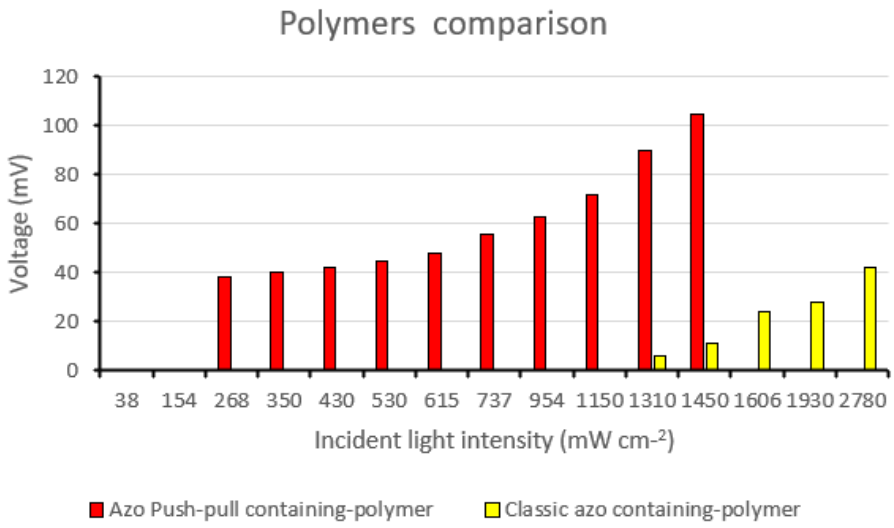

Figure 10. Comparison between voltage produced by device assembled using polymer containing **1-2** (red) and polymer containing **α–β** yellow) at different incident light intensity.

Conclusion

A novel photo-responsive device capable of transforming visible blue light into electrical energy has been developed. In comparison with photovoltaic systems the efficiency of this device is poor, but it constitutes a "proof of principle" prototype amenable of improvements in many aspects, both chemical and physical. A major point, to mention one, concerns the possibility of using a steady light source fueling the continuous oscillation of the LCN: such azo-based materials are known in the literature. Here we demonstrated that the use of push-pull azobenzenes, with a lower photoisomerization activation energy, improves the efficiency of this kind of polymers. Further modifications of the chemical structure of the chromophores could lead to a cheap device able to produce sufficient electricity for practical applications (e.g. IoT) from sunlight.

Experimental section

Materials

1,4-Bis-[4-(6-acryloyloxyhexyloxy)benzoyloxy]-2-methylbenzene(**3**),4[[6[(Acryloyl)oxy]hexyl] oxy]benzoic acid 4-cyanophenyl ester (**4**) and 2[ethyl(phenyl)amino]ethan-1-ol were purchased from Merck. Photoinitiator Irgacure 784, was purchased from Ciba. PVA with an average molecular weight of 40 000 g mol^{-1} was purchased from Sigma-Aldrich. Solvents were obtained from Merk. N-ethyl-N-hydroxy ethyl aniline, 4-nitroaniline and resorcinol were purchased from Sigma. Acryloyl chloride was purchased from TCI.

Synthesis of compounds

2-[ethyl({4-[(1E)-2-(4-nitrophenyl) diazen-1-yl]phenyl})amino]ethan-1-ol (DR1)

0,414 g (3 mmol, 1 eq.) of 4-nitroaniline was dissolved in a solution of 1,25 mL of concentrated hydrochloric acid and 8,87 mL of water. The mixture was cooled to 0°C in an ice-water bath, then a solution of 0,207 g (3 mmol, 1 eq.) of sodium nitrite in 2 mL of water was added dropwise. The resultant solution of neutralized salt was stirred for 30 min at 0–3◦C. Another solution of 0,3 g (1,8 mmol, 0,6 eq.) of N-ethyl-N-hydroxy ethyl aniline dissolved in 5 mL of hydrochloric acid (10%) was stirred for 5 min at 0◦C. The above solution of neutralized salt was added into this solution within 30 min. Allow the mixture to stand for 20 min and then was neutralized with added slowly and with stirring 10% NaOH solution. Reddish crystals filtered on a Buchner funnel and recrystallized from 2-propanol. Compound 1 was obtained as crimson crystals. Yield 76 %, 0,431 g.

2-[ethyl({4-[(1E)-2-(4-nitrophenyl) diazen-1-yl]phenyl})amino]ethyl prop-2-enoate (1)

2-[ethyl({4-[(1E)-2-(4-nitrophenyl) diazen-1-yl]phenyl})amino]ethan-1-ol (0,431g, 1,37 mmol, 1eq) was dissolved in 20 mL of THF under argon atmosphere, stirred and cooled to 0°C. Et_3N (0,19 mL, 1,37 mmol, 1 eq) was added and the mixture was left stirring for 30 min. Acryloyl chloride (0,144 mL, 1,78 mmol, 1,3 eq) was added dropwise leading to the production of a precipitate. After 30 min the mixture was filtered and the resulting crude clear red solution was subjected to chromatography column (dichloromethane) Rf product = 0,82. The resulting red

powder was crystalized with methanol. The desired compound was obtained with a yield of 34 %, 0,171 g.

1-(buta-1,3-dien-2-yloxy)-6-chlorohexane (5)

6-choro-exan-1-ol (2,048 g, 15 mmol, 1eq) was dissolved in 230 mL of THF under argon atmosphere, stirred and cooled to 0°C. Et_3N (4,186 mL, 30 mmol, 2 eq) was added and the mixture was left stirring for 30 min. Acryloyl chloride (1,22 mL, 15 mmol, 1 eq) was added dropwise leading to the production of a white precipitate. After 30 min the mixture was filtered and the resulting crude solution was subjected to chromatography column (Ethyl acetate: cyclohexane 1:9) Rf product = 0,82. The desired compound was obtained as a colorless oil with a yield of 87 %, 2,45 g.

4-[(1E)-2-(4-hydroxyphenyl) diazen-1-yl]benzene-1,3-diol (6)

4-aminophenol (15 mmol, 1.6 g, 1 equiv.) was suspended in water (4.1 mL). The reaction mixture was stirred and cooled to 0 °C with an ice bath. Concentrated HCl (4.1 mL) was added dropwise dissolving 4-aminophenol. After 10 min of stirring, a solution of sodium nitrite (17 mmol, 1.14 g, 1.1 equiv.) in water (3.5 mL) was added dropwise into the mixture. The solution was stirred for 2 h at 0 °C. Then, this solution was added dropwise over 2 h to a solution of resorcinol (15 mmol, 1.6 g, 1 equiv.) dissolved in water (3.5 ml) and NaOH (37.5 mmol, 1.5 g, 2.5 equiv.) at 0 °C. Stirring was continued for 3 h while the mixture was warmed to room temperature. The solution was acidified with 1 M HCl and a red solid precipitated was obtained as the pure product with a yield of 85% 2,96 g.

(E)-6-(4-((4-((6-(acryloyloxy)hexyl)oxy)-2-hydroxyphenyl)diazenyl)phenoxy)hexyl acrylate (2)

4-[(1E)-2-(4-hydroxyphenyl)diazen-1-yl]benzene-1,3-diol (0.43 mmol, 100 mg, 1 eq.), 6-Chlorohexylacrylate (0.86 mmol, 160 mg, 2 eq.), potassium carbonate (0.86 mmol, 120 mg, 2 eq.) and sodium iodide (catalytic amount) were suspended in DMF (5 mL) under an argon atmosphere and heated at 80 °C for 24h. The mixture was cooled, filtered and concentrated under vacuum. Chloroform was added to the mixture and the organic layer was washed with saturated NaHCO3 solution. The organic layer was dried over magnesium sulphate and concentrated. The crude mixture was subjected to chromatography column (dichloromethane: cyclohexane 4:1) Rf product = 0,5. The fractions containing the product were pooled and dried under vacuum, the obtained orange powder was crystalized with methanol. The desired compound was obtained with a yield of 60% 140 mg.

ESI spectra were recorded with a Micromass ZQ4000 instrument using methanol as solvent.

NMR spectra were collected on a 400 MHz VarianInova spectrometer with $CDCl_3$ as solvent.

UV-Vis absorption spectra were carried out using Jasco-550 Spectrophotometer, compounds **1-2** was dissolved in DCM at a concentration of 10^{-5}M and the UV-VIS spectrum was acquired in the range 280-600 nm.

Differential Scanning Calorimetry DSC measurements were carried out using a TA Instruments Q2000 DSC, equipped with a Refrigeratd Cooling System (RCS) system. Samples were subjected to a first heating scan at 10 °C min^{-1} from -80°C to 200 °C, a controlled cooling

at 10 °C min^{-1} up to -90 °C and a second heating scan at 10 °C min^{-1}, in nitrogen atmosphere. The Glass transiction temperature was determined at 47°C.

Thermogravimetric analysis was carried out using a TA Instrument Q500.

POM analysis was carried out using Zaiss microscope.

The temperature during irradiation was registered by using a thermal camera Optris Xi 400

Preparation of photoresponsive polymer

PVA (1 mw%) was suspended in water and left stirring for at 80°C until completely dissolved, then the solution was slowly cooled at RT. Custom-made cells (**Figure M1**) were obtained as following: the previously mentioned solution was spin-coated on a microscope slide at 3000 RPM, the glass was left on an hot plate at 100° for 20 mins. The PVA layer was rubbed with velvet placed on a self-made machine which gives a pressure of 11500 Pa. Another microscope slide was treated with plasma using Diener plasma surface Tetra 5200 LF machine with the following parameters: time 50 sec, air flow, power 50%.The two glassed were coupled together with the treated side turned towards each other, spaced with a kapton stripe of 20um thickness to leave a slot for the liquid crystal mixture and fixed with 2 clamps.The cells were placed on a hot plate controlled by a thermocouple and were filled by capillary action at 95 °C, at which temperature the monomers mixture is isotropic. Once the cells were totally filled, the temperature was decreased to reach the nematic phase, at 75 °C. The polymerization was performed at this temperature for about 24 h; during the first 2 hours cells were flipped every 30 min, while during the last hours were flipped every 8 h. A mercury lamp, equipped with optical fiber and a cut-off filter (OYA Y52, l>500 nm) to avoid premature isomerization of azobenzenes was used to trigger the photoiniziator (**Figure M2**). The light intensity during the polymerization was about 10 mW cm^{-2}. After photopolymerization, the film was post-cured at 120 °C for 10 min and slowly cooled to room temperature. Polymeric films were removed from cells using a razor.

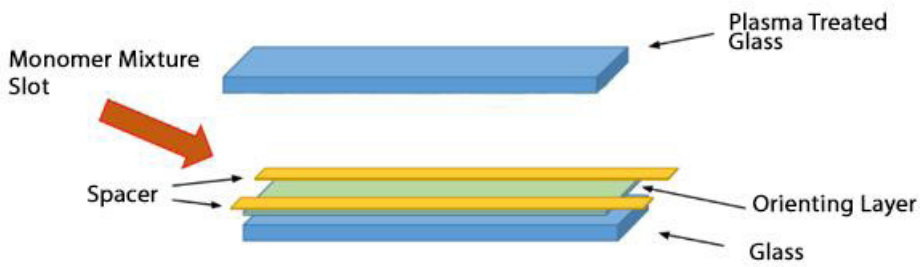

Figure M1. Home-made orienting cell configuration.

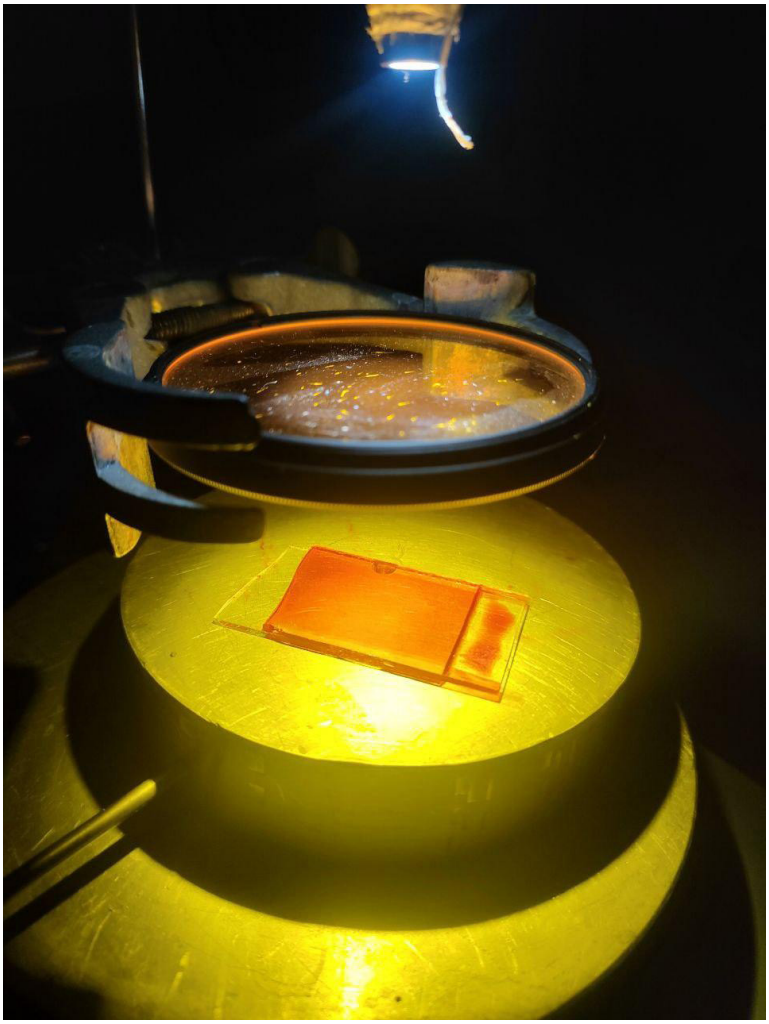

Figure M2. Polymerisation set-up.

Multimedia Files

Video 1. Device actuation

References

[1] Koerner, H., White, T. J., Tabiryan, N. V., Bunning, T. J., & Vaia, R. A. (2008). Photogenerating work from polymers. Materials Today, 11(7-8), 34-42.

[2] Wang, G., & Zhang, J. (2007). Photoresponsive molecular switches for biotechnology. Organic Letters, 9(20), 3865-3868.

[3] Schultz, T., Quenneville, J., Levine, B., Toniolo, A., Martínez, T. J., Lochbrunner, S., Schmitt, M., Shaffer, J. P., Zgierski, M. Z., & Stolow, A. (2003). Mechanism and dynamics of azobenzene photoisomerization. Journal of the American Chemical Society, 125(27), 8098-8099.

[4] Henzl, J., Mehlhorn, M., Gawronski, H., Rieder, K. H., & Morgenstern, K. (2006). Reversible cis-trans isomerization of a single azobenzene molecule. Angewandte Chemie International Edition, 45(4), 603-606.

[5] Crespi, S., Simeth, N. A., & König, B. (2019). Heteroaryl azo dyes as molecular photoswitches. Nature Reviews Chemistry, 3, 133-146.

[6] Aleotti, F., Nenov, A., Salvigni, L., Bonfanti, M., El-Tahawy, M. M., Giunchi, A., Gentile, M., Spallacci, C., Ventimiglia, A., Cirillo, G., Montali, L., Scurti, S., Garavelli, M., & Conti, I. (2020). Spectral Tuning and Photoisomerization Efficiency in Push–Pull Azobenzenes: Designing Principles. The Journal of Physical Chemistry A, 124(39), 9513-9523.

[7] Liu, Z., Yang, X., Guo, H., Zhang, X., Wang, L., Zheng, Y., Zhang, J., Shi, W., Yang, W., Chen, T., Lu, W., Chen, J., Xu, L., Gao, H., & Zou, G. (2020). Controllable manipulation of fluorescence emission in photochromic material for anti-counterfeiting. ACS Applied Materials & Interfaces, 12(39), 44195-44204.

[8] Yamada, M., Kondo, M., Mamiya, J., Yu, Y., Kinoshita, M., Barrett, C. J., & Ikeda, T. (2008). Photomobile polymer materials: towards light-driven plastic motors. Angewandte Chemie International Edition, 47(27), 4986-4988.

[9] Lu, X., Guo, S., Tong, X., Xia, H., & Zhao, Y. (2017). Tunable Photocontrolled Motions Using Stored Strain Energy in Malleable Azobenzene Liquid Crystalline Polymer Actuators. Advanced Materials, 29(28).

[10] Pilz da Cunha, M., Foelen, Y., Engels, T. A. P., Papamichou, K., Hagenbeek, M., Debije, M. G., & Schenning, A. P. H. J. (2019). Optical indicators based on cholesteric liquid crystal polymers . Advanced Optical Materials, 7, 1801604.

[11] Lu, X., Zhang, H., Fei, G., Yu, B., Tong, X., Xia, H., & Zhao, Y. (2018). Liquid-Crystalline Dynamic Networks Doped with Gold Nanorods Showing Enhanced Photocontrol of Actuation. Advanced Materials, 30(14), e1706597.

[12] Cheng, F., Yin, R., Zhang, Y., Yen, C.-C., & Yu, Y. (2010). Fully plastic microrobots which manipulate objects using only visible light. Soft Matter, 6, 3447-3449.

[13] Pilz da Cunha, M., Kandail, H. S., den Toonder, J. M. J., & Schenning, A. P. H. J. (2020). An artificial aquatic polyp that wirelessly attracts, grasps, and releases objects. Proceedings of the National Academy of Sciences of the United States of America, 117(30), 17571-17577.

[14] Sun, D., Zhang, J., Li, H., Shi, Z., Meng, Q., Liu, S., Chen, J., & Liu, X. (2021). Toward Application of Liquid Crystalline Elastomer for Smart Robotics: State of the Art and Challenges. Polymers, 13, 1889.

[15] Verpaalen, R. C. P., Engels, T., Schenning, A. P. H. J., & Debije, M. G. (2020). Stimuli-Responsive Shape Changing Commodity Polymer Composites and Bilayers. ACS Applied Materials & Interfaces, 12(35), 38829-38844.

[16] Jerca, F. A., Jerca, V. V., & Hoogenboom, R. (2022). Advances and opportunities in the exciting world of azobenzenes. Nature Reviews Chemistry, 6, 51-69.

[17] Angeloni, A. S., Caretti, D., Carlini, C., Chiellini, E., Galli, G., Altomare, A., Solaro, R., & Laus, M. (1989). Photochromic liquid-crystalline polymers. Main chain and side chain polymers containing azobenzene mesogens. Liquid Crystals, 4(5), 513-527.

[18] Yu, Y., Nakano, M., & Ikeda, T. (2003). Directed bending of a polymer film by light. Nature, 425, 145.

[19] Gelebart, A., Jan Mulder, D., Varga, M., et al. (2017). Making waves in a photoactive polymer film. Nature, 546, 632–636.

[20] Garcia-Amorós, J., Sánchez-Ferrer, A., Massad, W. A., Nonell, S., & Velasco, D. (2010). Kinetic study of the fast thermal cis-to-trans isomerisation of para-, ortho- and polyhydroxyazobenzenes. Physical Chemistry Chemical Physics, 12, 13238–13242.

[21] Garcia-Amorós, J., & Velasco, D. (2014). Understanding the fast thermal isomerisation of azophenols in glassy and liquid-crystalline polymers. Physical Chemistry Chemical Physics, 16, 3108.

[22] Pilz da Cunha, M., van Thoor, E. A. J., Debije, M. G., Broer, D. J., & Schenning, A. P. H. J. (2019). Unravelling the photothermal and photomechanical contributions to actuation of azobenzene-doped liquid crystal polymers in air and water. Journal of Materials Chemistry C, 7, 13502-13509.

[23] Mol, G. N., Harris, K. D., Bastiaansen, C. W. M., & Broer, D. J. (2005). Thermo-mechanical responses of liquid-crystal networks with a splayed molecular organization. Advanced Functional Materials, 15, 1155-1159.

[24] Hu, Y., Kang, W., Fang, Y., Xie, L., Qiu, L., & Jin, T. (2018). Piezoelectric Poly(vinylidene fluoride) (PVDF) Polymer-Based Sensor for Wrist Motion Signal Detection. Applied Sciences, 8, 836.

[25] Sappati, K. K., & Bhadra, S. (2018). Piezoelectric Polymer and Paper Substrates: A Review. Sensors, 18, 3605.

CHAPTER 3

4D printing of a photo-, thermal-, and water-responsive liquid crystal elastomer actuator

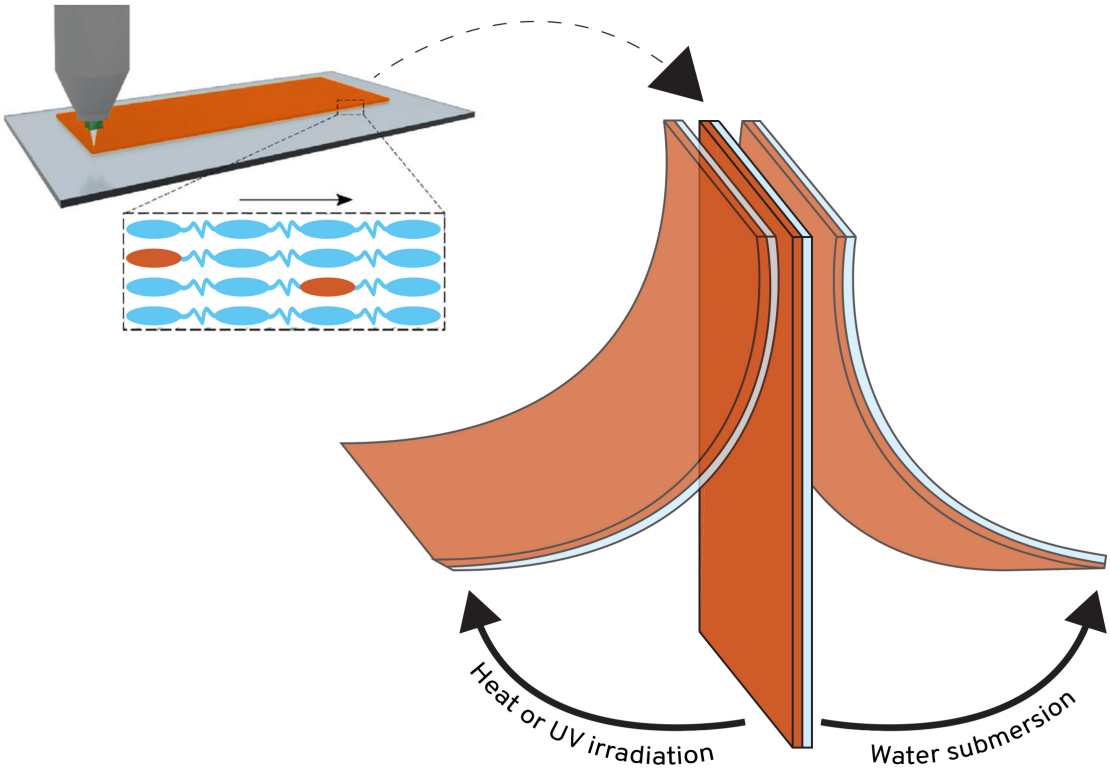

This project was carried out in collaboration with Jeroen A. H. P. Sol, Stefano Masiero, Albert P. H. J. Schenning, and Michael G. Debije

Introduction

Additive manufacturing (AM) is becoming more popular for fabrication of soft-robotic and other mechanical components; AM allows making of three-dimensional structures quickly using a variety of materials [1–3]. Direct ink writing (DIW) represents an innovative orientation method for liquid crystals[4]: in recent years different liquid crystal elastomers (LCE) devices have been fabricated using DIW to perform multiple roles in soft robotics [5]. LCEs have been designed to respond to external stimuli including light [6–8] moisture [9], temperature [5,8] and magnetic fields [10]. Light triggered actuators are particularly interesting for their rapid response and their easy and non-invasive manner of address. Actuation behavior is obtained in the LCEs by introducing photo responsive moieties in the polymer, such as azobenzenes (AZOs) or spiropirans [11].

AZOs are molecules able to induce macroscopic changes in the shape of polymers even when present in low concentrations. AZO-containing polymers can be photo-triggered in different conditions and in different environments [12,13], and AZO moieties have been widely used as a photoresponsive core in numerous liquid crystalline devices [14–20]. In recent years oligomers containing azobenzene-based monomers have been exploited as inks for DIW light responsive devices [8,21,22].

The photoisomerization mechanisms of AZOs are affected by the chemical structure of the cores as well as by the environment. In particular, heteroatoms and substituents on the aromatic rings connected to the AZO-group have a strong influence on the rate of thermal return from the *cis* to the *trans* configuration [23]. The presence of a hydroxyl group in ortho position with respect to the aza group leads to the formation of an intramolecular hydrogen bond and decreases the *cis*-isomer half-life [24–26]. Literature presents few examples of photoresponsive devices involving a supramolecular structure capable of influencing activation [27,28], and none of them has been obtained through DIW. In this work we describe the fabrication and performances of a temperature-, light- and water-responsive LCE cantilever obtained by DIW using an ink containing a novel ortho-hydroxy-azobenzene moiety that shows what appears to be unique actuation variability.

Results & Discussion

An LC oligomer used for the DIW needed to satisfy two requirements: 1) a broad temperature range for the liquid crystalline phase to allow both DIW and photopolymerization at different temperatures while maintaining liquid-crystalline anisotropy, and 2) inclusion of a responsive liquid crystalline monomer in the main chain to improve the network pull force. Ortho-hydroxyl azobenzene core -trihydroxyazobenzene was synthesized through a classic diazo-copulation reaction, while diacrylate azobenzenemonomer **2** was obtained via nucleophilic substitution between the Trihydroxyazobenzene and the acrylate terminated tails 6-chlorohexyl acrylate (**Scheme 1**). The ink was obtained by modifying a previously reported DIW ink [8] by replacing 4,4′-bis(6-acryloyloxyhexyloxy) azobenzene with o-hydroxyl diacrylate azobenzene **2** in the main chain of the LC oligomer. The chemical composition for the oligomer consists of reactive mesogens **1**, **2**, and the isotropic chain extender **3** (**Figure 1**). The acrylate-terminated main chain LC oligomer was synthesized via a dimethylphenylphosphine (DMPP) catalysed thiol-Michael addition reaction with a slight excess of acrylates versus thiol (1.1 to 1) . The post

reaction ^{1}H-NMR spectrum shows acrylate signals between 6.40-5.70 ppm and the presence of hydroxyl group on the ring. Gel permeation chromatography showed the characteristic trans-azobenzene peak at ≈390 nm and the peak at ~260 nm had the same retention times, confirming that azobenzene residues were incorporated into the main chain oligomer. The average molecular weight was = 9000 g mol $^{-1}$. A differential scanning calorimetry (DSC) spectrum and polarized optical microscopy (POM) showed a crystal-to-smectic phase transition (T_c/Sm) at ≈- 25°, a smectic-to-nematic phase transition temperature (Sm/N) at ≈42 °C, and a nematic-to-isotropic phase transition temperature (N/I) at 76 °C (spectra are reported in methods and materials section of this chapter).

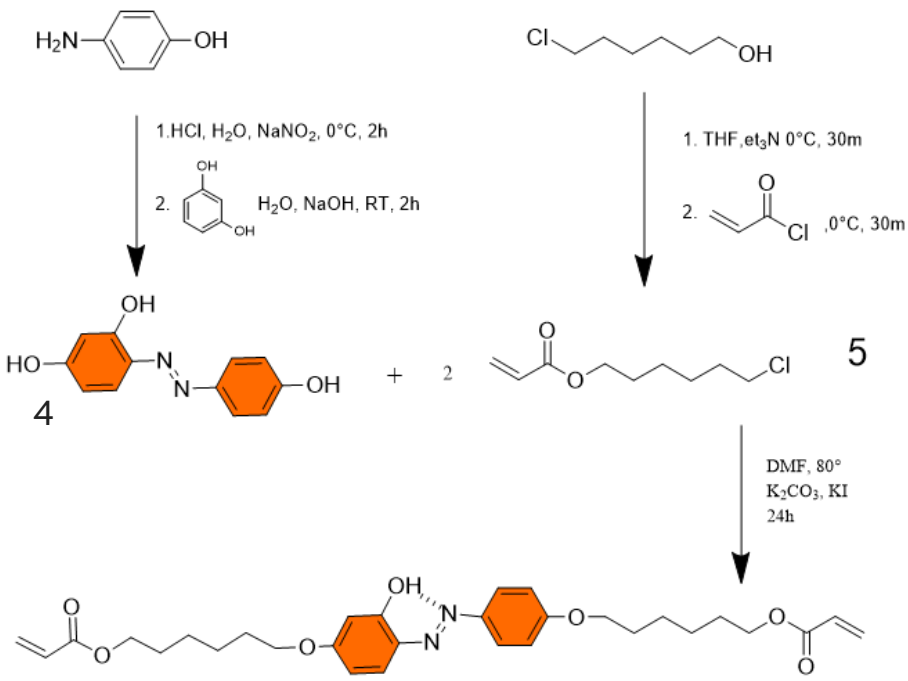

Scheme 1. Synthesis of **2.**

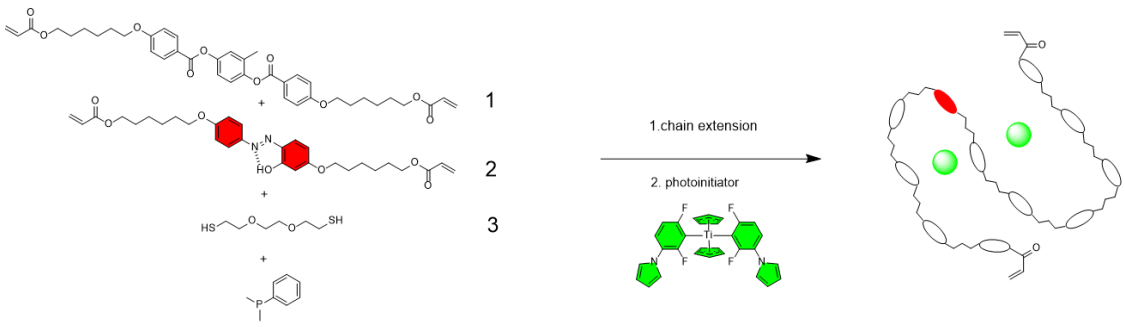

Figure 1. Synthesis of the oligomer and chemical composition of the ink: the reactive mesogens (**1**), o-Hydroxyl azobenzene (**2**), di-thiol spacer (**3**), catalyst and photoinitiator (green).

The ink was used for DIW to fabricate uniaxially oriented films. The printing temperature was set to 60 °C. Lines printed at speeds < 5 mm s^{-1} did not show alignment when viewed via polarized optical microscopy (POM). Lines printed with speeds 6 - 15 mm s^{-1} showed birefringence when viewed via POM, suggesting the LCs oriented along the printing direction (**Figure 2A-B**). Based on these observations, the printing speed was set to 12 mm s^{-1}.

Single layer 'stripes' of different dimensions (2-5 x 25 mm^2) were printed on top of either a glass substrate coated with polyvinylpyrrolidone (PVP) acting as sacrificial layer (**Figure 2C**) to generate free-standing films (FS), or on a 10 μm uniaxially stretched polyetherimide (PEI) foil with nanogrooves as the passive substrate to create substrate bound (SB) bilayer films for the novel actuators. There is no indication that stretched PEI acts as an alignment layer for oligomeric mesogens: alignment is solely dictated by the motion of the printing head relative to the substrate [29]. PEI has a storage modulus of ca. 3000 MPa at 20 °C, the same order of magnitude poly (ethylene terephthalate) (PET) [30].

After photopolymerization, sol/gel fraction experiments revealed an average 87% gel fraction for the LCE while, according to the IR spectrum, there were no unreacted acrylate groups. Using a contact profiler, we determined the average thickness of the oriented LC film to be 100 μm. After characterization, the film was either detached from the glass substrate by dissolving the PVP layer to obtain a free-standing film, or using a laser cutter to cut the PEI support around the LCE rectangles (**Figure 2D**) so the PEI film had 50% of its area covered by the LCE for enhanced actuation [31].

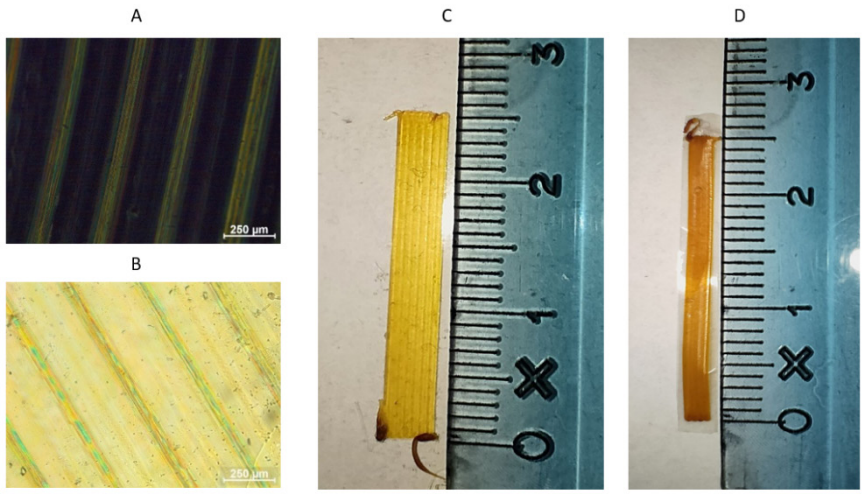

Figure 2 Polarized optical microscopy images of the printed film (A) parallel to one polarizer or (B) at 45° with respect to both polarizers (B). The scale bar represents 250 μm. (C) Polymer stripes printed on glass covered by a PVP layer and (D) on PEI substrate.

Temperature response

The response of both the FS and SB films to temperature were investigated using an oven. Films containing **2** contracted along the deposited films length upon heating, similar to results described in the literature [5,8]. Longitudinal film shrinkage was quantified by plotting the fractional change in length as a function of temperature. Different stages of the response were observed for both samples (**Figure 3**): from 30 °C to ≈40 °C, minimal contraction was observed in the freestanding film, followed by a large actuation region from ≈50 °C (corresponding to the first mesophase transition in the DSC) to ≈80 °C, in which the film started to contract and showed a reduction in length of about 20%. A second actuation occurred above 80 °C (corresponding to the N/I transition in the DSC), in which the film underwent a further length contraction of about 30%, so that the overall contraction was about 50%. Beyond 80°C, the LCs in the polymerized film are in the isotropic phase, leading to the maximum contraction along the deposition direction concurrent with an increase in width. No additional changes in shape were registered above 90 °C. The film recovered its initial shape upon cooling the sample back to 30 °C. In contrast, the substrate-adhered sample rolls up with the deposited film on the inside of the curl upon heating. The thermal actuations of the two films are illustrated in **Figure 4**.

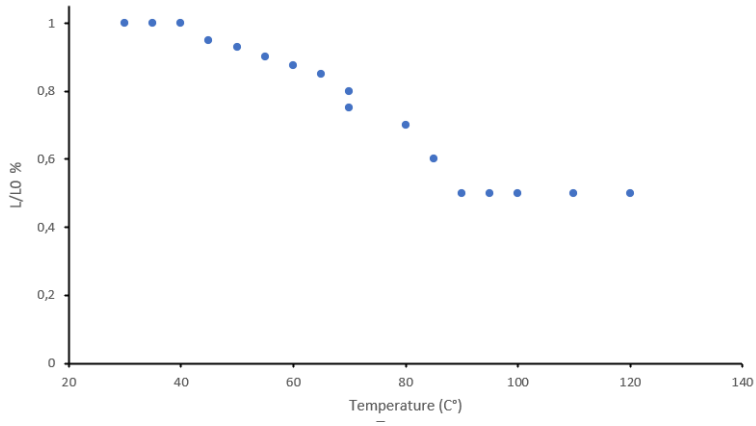

Figure 3. Longitudinal shrinkage ratio (L/L_0) of the freestanding film as a function of temperature. L represents the length of the film at a given temperature and L_0 the length at 30 °C.

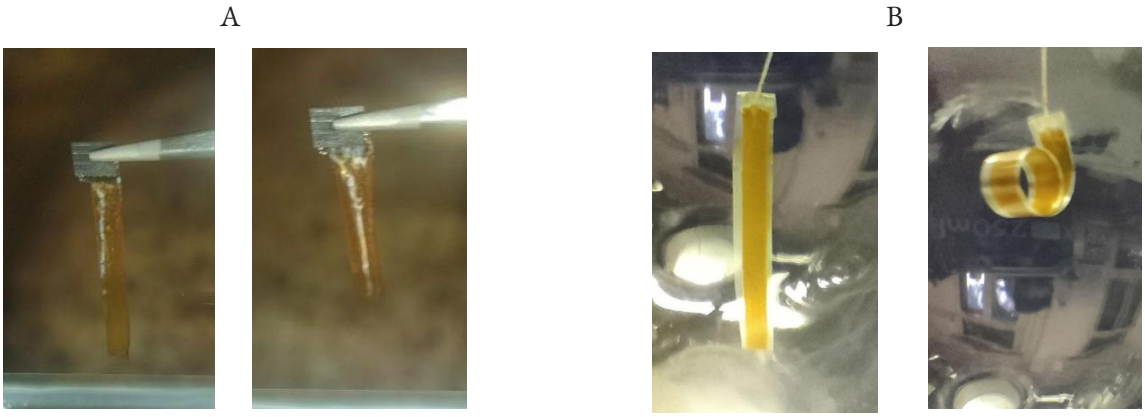

Figure 4. Photographs of the a) freestanding film at 30 °C and at 100 °C, showing the contraction of the film along its long axis and expanding along its width, and b) the substrate attached film at 20°C and 60°C demonstrating the curling of the film.

Light response in air

Photoactuation using a 385 nm light was investigated for 4 x 25 mm^2 SB and FS films. Films were clamped and hung from a stand as shown in **Figure 5**. FS samples did not showed regular deformation. Photoactuation of the SB film was studied by tracking the film's tip vertical displacement under different light intensities with the deposited polymer film facing the light source in the case. Simultaneously, the temperature of the film's exposed surface was registered with an IR thermal camera. The SB film bends towards the light beam: increasing the light intensity, and thus the heating of the sample, increased the maximum bending angle until a plateau was reached. After switching off the light, the PEI bound film does not return to its initial shape, but bends away from the light beam. Recovery of the initial position is achieved after a few minutes without involving other stimulus (**Figure 6**). After 10 cycles of alternating UV light and darkness, the films didn't show any signs of fatigue (**Video 1-2**). The actuation is governed both by photothermal and photomechanical effects: no significant bending was observed when the measured film temperature was below 40°. This behavior is a consequence of the fast thermal return of the o-hydroxyl azo core from *cis* to *trans* isomers [25] and to the temporary expansion of the surface exposed to light. This rapid recovery made it impossible to isolate the *cis* isomer in the UV-Vis spectrum after irradiation.

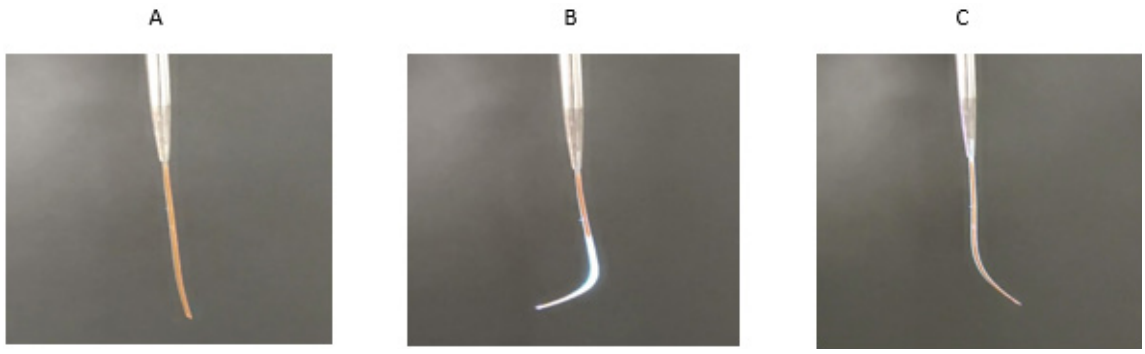

Figure 5. Photoactuation of the film printed on PEI in air (printed film on the left side): bending triggered by 385 nm light incident from the left. A) light off, starting position, B) light on bending through the light source C) light off, bending away from the light source after irradiation.

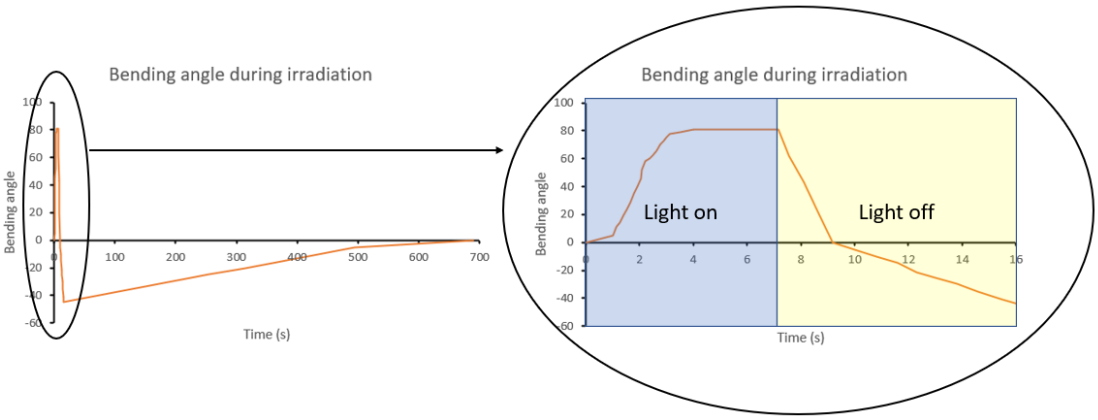

Figure 6. The SB film tip vertical displacement during and after the irradiation with 385 nm 550 mW cm^{-2} light

Response to water submersion

The SB film showed interesting behaviors when submerged in water at temperatures between 0 and 20 C° in the absence of light exposure, it rolls with the substrate on the inside of the curl. Once dried, both films recover their initial shapes. The films take about 20 minutes to reach their maximum displacements and another 20 minutes to return to their original shapes when removed from the water (the curling and uncurling of the substrate-attached film is seen in **Figure 7**).

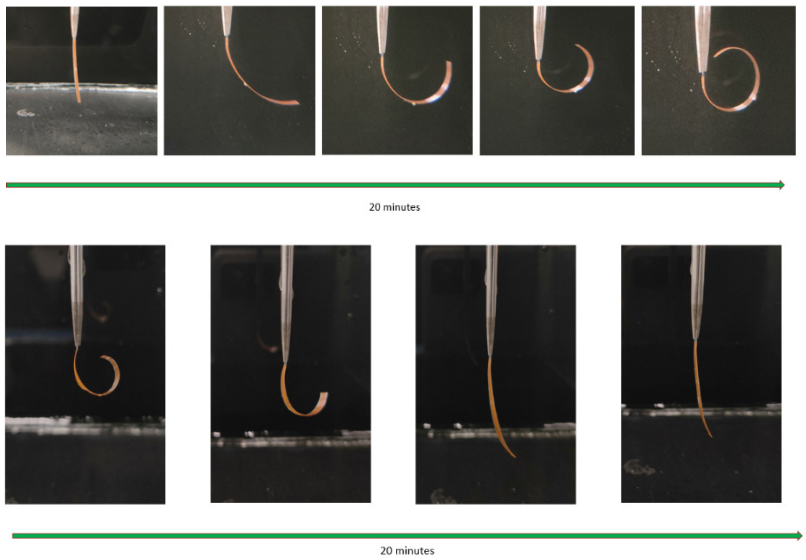

Figure 7. (Top) Actuation of the substrate-bound film during 20 minutes under water at 15°C. The DIW polymer is on the left. (Bottom) Uncurling of the substrate-bound film to the original shape after removal from water.

Increasing the water temperature led to a contraction of the printed polymer: the SB film reaches a vertical steady-state between 32 and 45 C° and rolls on the polymer side above this temperature (**Figure 8**). Samples were viewed under POM to ascertain if the liquid immersion disrupted the order of the liquid crystalline molecules: no obvious changes were observed. Macroscopically, the samples appeared to respond identically whether submerged in basic (pH 8-14) or acidic (pH 6-1) solutions. This gradual change of shape driven by the contact with water at room temperature or below is an unusual behavior, and to the best of our knowledge has not been reported, with the exception of liquid crystal polymers containing dimers of carboxyl acids, whose pairing can be influenced by pH [27]; an explanation for this odd behavior was therefore sought. As a reference experiment, films containing (4,4′-bis(6-acryloyloxyhexyloxy) azobenzene) as photoresponsive chromophore and Irgacure 819 as photoinitiator produced following reported procedures were prepared [8]; and once submerged, these samples absorbed water and became scattering/opaque but didn't undergo any shape change. In contrast, films using the new **2** remain shiny/translucent and demonstrate significant bending underwater. The extent of water absorption in the samples containing **2** is minimal: their weight does not change significantly after submersion; an increase of only 3% was recorded after 20 minutes of immersion. LC networks made up of similar monomers (**1,3**) and photoresponsive (4,4′-bis(6-acryloyloxyhexyloxy)azobenzene) moieties have shown a response when subjected to moisture but not when submersed in water [28]: IR spectra were used to evaluate if there were differences in carbonyl and ethereal bonds stretching frequencies between the current dry and the moist films. No significant changes were observed, ruling out changes in hydrogen bond arrangements between **1** and **2** as the origin of the effect.

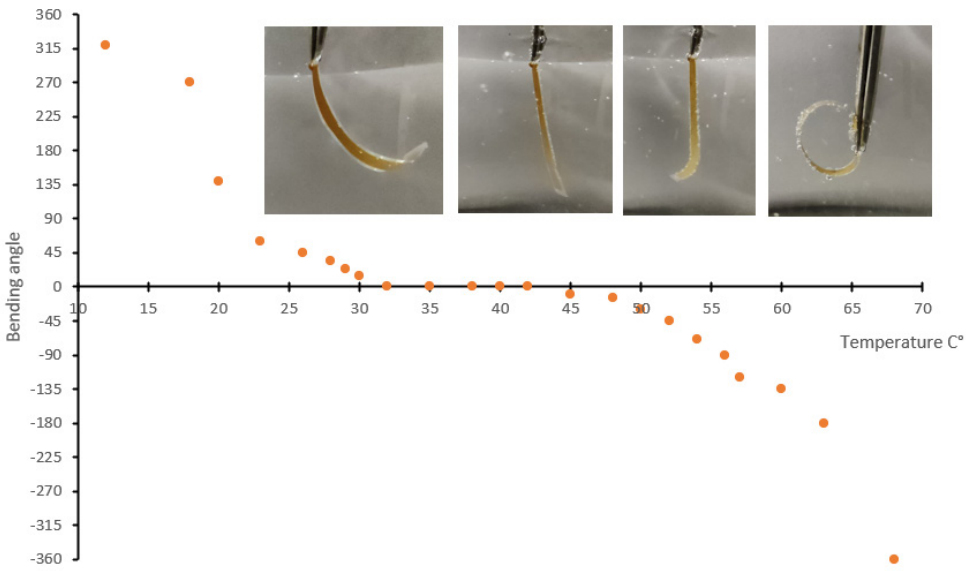

Figure 8. Underwater change in shape of SB actuator driven at different water temperatures. At low temperature the expansion of the polymer leads to a bending to the substrate side, while at higher temperatures the contraction of the polymers makes to device to bend to the polymer side. (Inset) Photographs of sample in round beaker displaying actuation at the three temperature stages.

We propose that the observed phenomena at low temperature are driven by a superficial expansion of the film caused by changes in supramolecular interactions on the surface in contact with water. Water forms hydrogen bonds with the hydroxyl groups on the azobenzoic ring previously engaged in bonding with nitrogen: the rearrangement of those bonds induces a nanoscale expansion of the AZO monomer, leading to a macroscopic expansion of the polymer surface.

The substrate bound films underwater photoactuation of the SB was investigated. The films did not show any actuation when irradiated with low intensity 385 nm light. However, replacing this lamp with a 1760 mW cm^{-2} 365 nm lamp resulted in photomechanical actuation and bending under water as shown in **Video 3**. Once the light is switched off, the return to the starting position is almost instantaneous: the polymer needs only few second to recover its initial shape, because of the fast *cis* to *trans* isomerisation of o-azophenols [26]. Bending and reversion occur at any environmental water temperature ranging from 0° to 50 °C (above this temperature, the bending of the film is at such a steep angle it is physically no longer possible to illuminate the film). The maximum bending angles induced by illumination underwater vary: bending is greater at lower water temperatures and decrease as the temperature rises. When the film is subjected to a previous bending due to thermal shrinkage the contraction results lower, moreover at high temperature the thermal return from cis to trans form is faster [25], making harder to isolate an high cis isomer percentage during the irradiation .

Conclusion

A novel oligomeric ink in which the proprieties of photoresponsive moieties are influenced by a hydrogen bond was synthesized for the fabrication of thermal, light and water sensitive LCE films via DIW. The LCE performs multiple roles if triggered in different environments or conditions: it can rapidly change its shape up to a bend of almost 80 degrees if irradiated in air or undergoes a shrinkage of about 50% of its length when heated. Moreover, the film can assume different shapes in water depending on environmental temperature and can work as an amphibious “fast shape recovering” actuator. This first attempt to include supramolecular structures in ink for DIW opens new possibilities for fabrication of devices for soft robotics, such e as light driven swimming objects. The film can also be coupled with other photoresponsive stripes to develop a “double way activation” bilayer.

Methods and materials

Materials

1,4-Bis-[4-(6-acryloyloxyhexyloxy) benzoyloxy]-2-methylbenzene (**1**, RM82) was purchased from Merck. 3,6-Dioxa-1,8-octanedithiol (**3**, DODT) and 1,8-diazabicyclo[5.4.0] undec-7-ene (DBU) were obtained from Sigma-Aldrich. DMPP Catalyst was obtained from Merk. Photoinitiator Irgacure 784 was purchased from Ciba. Polyvinylpyrrolidone with an average molecular weight of 40,000 g mol^{-1} was purchased from Sigma-Aldrich. Solvent, dichloromethane (DCM) was obtained from Biosolve.

Synthesis of compounds

1-(buta-1,3-dien-2-yloxy)-6-chlorohexane (5)

6-choro-exan-1-ol (2.048 g, 15 mmol, 1eq) was dissolved in 230 mL of THF under argon atmosphere, stirred and cooled to 0°C. Et_3N (4.186 mL, 30 mmol, 2 eq) was added and the mixture was left stirring for 30 min. Acryloyl chloride (1,22 mL, 15 mmol, 1 eq) was added dropwise leading to the production of a white precipitate. After 30 min the mixture was filtered and the resulting crude solution was subjected to chromatography column (Ethyl acetate: cyclohexane 1:9) Rf product = 0.82. The desired compound was obtained as a colorless oil with a yield of 87%, 2.45 g.

4-[(1E)-2-(4-hydroxyphenyl) diazen-1-yl]benzene-1,3-diol (4)

4-aminophenol (15 mmol, 1.6 g, 1 equiv.) was suspended in water (4.1 mL). The reaction mixture was stirred and cooled to 0 °C with an ice bath. Concentrated HCl (4.1 mL) was added dropwise dissolving 4-aminophenol. After 10 min of stirring, a solution of sodium nitrite (17 mmol, 1.14 g, 1.1 equiv.) in water (3.5 mL) was added dropwise into the mixture. The solution was stirred for 2 h at 0 °C. Then, this solution was added dropwise over 2 h to a solution of resorcinol (15 mmol, 1.6 g, 1 equiv.) dissolved in water (3.5 ml) and NaOH (37.5 mmol, 1.5 g, 2.5 equiv.) at 0 °C. Stirring was continued for 3 h while the mixture was warmed to room temperature. The solution was acidified with 1 M HCl and a red solid precipitated was obtained as the pure product with a yield of 85% 2,96 g.

(E)-6-(4-((4-((6-(acryloyloxy)hexyl)oxy)-2hydroxyphenyl)diazenyl)phenoxy)hexyl acrylate (2)

4-[(1E)-2-(4-hydroxyphenyl)diazen-1-yl]benzene-1,3-diol (0.43 mmol, 100 mg, 1 eq.), 6-Chlorohexylacrylate (0.86 mmol, 160 mg, 2 eq.), potassium carbonate (0.86 mmol, 120 mg, 2 eq.) and sodium iodide (catalytic amount) were suspended in DMF (5 mL) under an argon atmosphere and heated at 80 °C for 24 h. The mixture was cooled, filtered, and concentrated under vacuum. Chloroform was added to the mixture and the organic layer was washed with saturated $NaHCO_3$ solution. The organic layer was dried over magnesium sulphate and concentrated. The crude mixture was subjected to chromatography column (dichloromethane: cyclohexane 4:1), Rf product = 0.5. The fractions containing the product were pooled and dried under vacuum, the resulting orange powder was crystalized with methanol. The desired compound was obtained with a yield of 60%, 140 mg.

Oligomer synthesis

1 4-Bis-[4-(6-acryloyloxyhexyloxy) benzoyloxy]-2-methylbenzene (3.747g, 1 eq., 5,575mmol), **2** *(E)-6-(4-((4-((6-(acryloyloxy)hexyl)oxy)-2-hydroxyphenyl)diazenyl)phenoxy)hexyl Acrylate* (0,300g, 0.1 eq., 0.557 mmol), **3** 3,6-dioxa-1,8-octanedithiol (1.014g, 0.9eq., 5.575 mmol) where dissolved in 40 ml of DCM under Argon in a one neck flask. Argon was bubbled in the stirring solution for 45 min causing the evaporation of the solvent and consequent decrease in temperature, Dmpp (0,0075g) was added and then the solution was heated to RT . The reaction was left stirring overnight at room temperature. The next day Irgacure 784 (0,1g, 0,033eq., 0,187mmol) was added and the flask was moved into darkness to avoid polymerization. The mixture was poured in a Teflon dish and covered with aluminum foil with little holes to evaporate the solvent overnight. The removal of the residual solvent was conducted in a vacuum oven at room temperature.

Preparation and deposition of the Ink

The oligomer, the synthesis of whic is described in the previous paragraph, was used as ink.

Direct Ink Writing was performed using a commercial 3D printer (EHR, Hyrel 3D). The ink was loaded into the stainless-steel reservoir at room temperature and extruded using a nozzle diameter of 335 μm at 60 °C. The printing speed was 1.2 cm s^{-1}. Films ranging from 2 × 20 mm^2 to 5 x 20 mm^2 were printed on top of a PVP-coated glass and on a PEI substrate. The printing path was controlled by a G-code generated by the printer software. The distance between the deposited lines was set to 0.28 mm, while the distance between nozzle and the bed was 110 μm. After printing samples were photopolymerized in a glass box under nitrogen at room temperature with 40 mW cm^{-2} of 530 nm collimated light LED (ThorLabs) to induce polymerization, the power controller (ThorLabs DC4104) used to tune the intensity. After exposure for 2 h, in which the sample was flipped every 30 min, the film's thickness and birefringence were characterized via a profiling system and a microscope, respectively. To obtain a freestanding film, the PVP layer was dissolved by immersing the sample in water at room temperature and subsequently dried at room temperature overnight, while films printed on PEI were cut with a laser cutter.

Characterization instruments

^{1}H NMR spectra were collected on a 400 MHz Bruker Advance III HD spectrometer with chloroform/dichloromethane as solvent. GPC with was performed on a Shimadzu apparatus to evaluate the number average molecular weight (*M*n), weight average molecular weight (*M*w), and polydispersity index (PDI) of oligomers using polystyrene (PS) with an average *M*w of 350 000 g mol^{-1} as reference. DSC measurements used a TA Instruments DSC Q1000. All microscopy images were taken with a Leica DM 2700M equipped with two polarizers that were operated either crossed or parallel. The thickness of the film was determined via a Bruker DektakXT contact profile system. For actuation in air, films were placed at 20.0 cm distance from collimated UV light (365 nm, Thorlabs M365L2). A camera (Nikon D7200, Olympus OM-D E-M10 Mk III) was used to record the light-driven deformation. The temperature of the surface of the film was measured using a Gobi camera from Xenics. Underwater actuation was conducted inside a transparent beaker.

GPC Spectrum

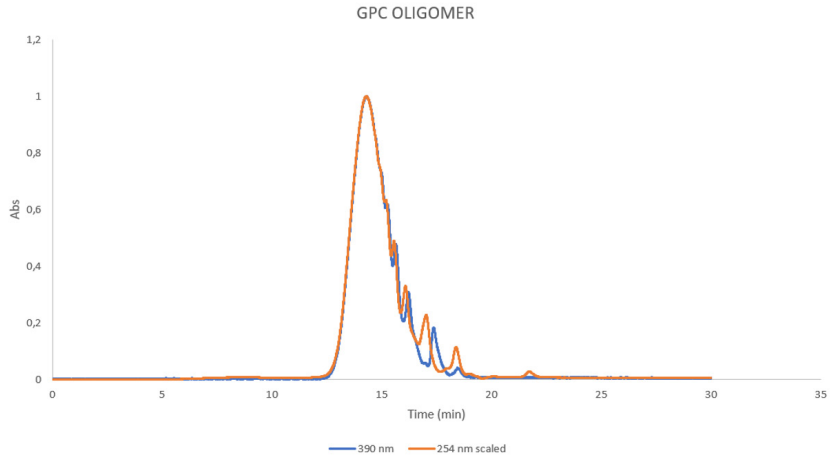

NMR Spectrum

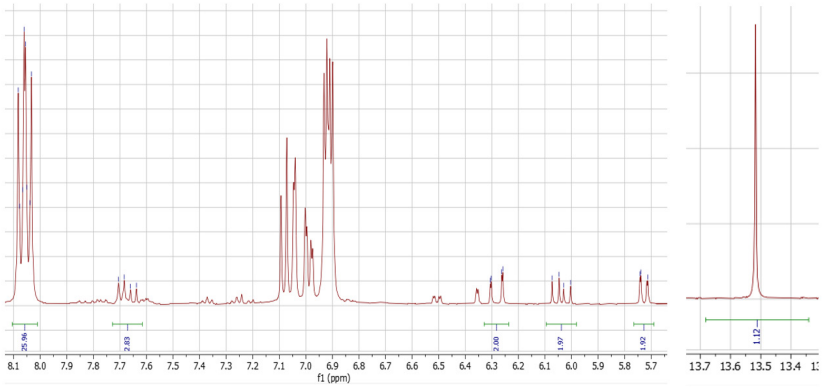

DSC Spectrum

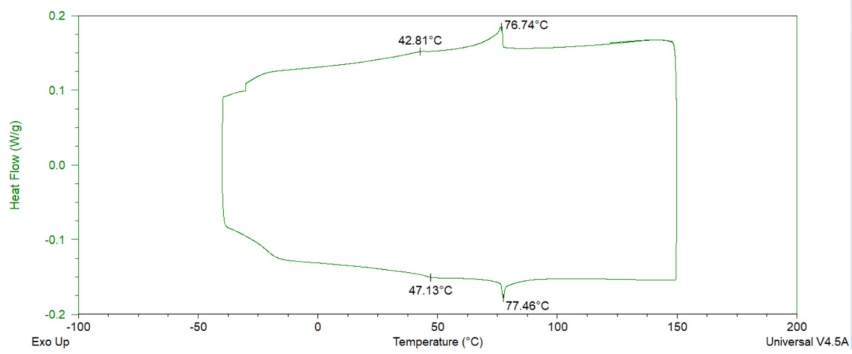

Irradiation set-up

Film was placed at 20.0 cm distance from collimated UV light (385 nm, Thorlabs M385L2). A controller (ThorLabs DC4104) was used to tune the intensity of the lights. A camera (from Real time GT master edition) was used to record the light-driven deformation. The temperature of the surface of the film was controlled using a Gobi camera from Xenics.

Underwater actuation was conducted inside a transparent beaker; the temperature was controlled by an ot plate connected to a thermocouple (Nika). The 365 nm UV lamp ((Hamamatsu LC-L1V3, 365 nm) was placed at 3 cm distance from the sample and the actuation was recorded with the same camera.

Multimedia Files

Video 1. Irradiation cycles in air

Video 2. Single pulse irradiation in air

Video 3. Underwater irradiation at 20°C

References

[1] Truby, R. L., & Lewis, J. A. (2016). Printing soft matter in three dimensions. Nature, 540, 371–378.

[2] Lee, J.-Y., An, J., & Chua, C. K. (2017). Two-photon polymerization of photo-curable polymer for three-dimensional microstructures. Applied Materials Today, 7, 120–133.

[3] Mechtcherine, V., Bos, F. P., Perrot, A., da Silva, W. R. L., Nerella, V. N., Fataei, S., Wolfs, R. J. M.,Sonebi, M., & Roussel, N. (2020). Cementitious materials in the digital age. Cement and Concrete Research, 132, 106037.

[4] del Pozo, M., Sol, J. A. H. P., Schenning, A. P. H. J., & Debije, M. G. (2022). Programmable morphing of large-area, 3D liquid crystal polymer sheets. Advanced Materials, 34, 2104390.

[5] López-Valdeolivas, M., Liu, D., Broer, D. J., & Sánchez-Somolinos, C. (2018). Light-induced shape change and actuation in liquid crystal polymers. Macromolecular Rapid Communications, 39, 3–9.

[6] Zhang, Y., Huang, L., Song, H., Ni, C., Wu, J., & Zhao, Q. (2019). Structural color patterns in liquid crystalline elastomer films with chemical patterns. ACS Applied Materials and Interfaces, 11,32408–32413.

[7] Nishiguchi, A., Zhang, H., Schweizerhof, S., Schulte, M. F., Mourran, A., & Möller, M. (2020). Multiresponsive anisotropic hydrogels with reversible shape-memory behavior. ACS Applied Materials and Interfaces, 12, 12176–12185.

[8] del Pozo, M., Liu, L., Pilz da Cunha, M., Broer, D. J., & Schenning, A. P. H. J. (2020). Light-driven motion of large-area, liquid crystal polymer actuators with patterned molecular alignment. Advanced Functional Materials, 30, 2005560.

[9] Sol, J. A. H. P., Smits, L. G., Schenning, A. P. H. J., & Debije, M. G. (2022), Direct Ink Writing of 4D Structural Colors. Adv. Funct. Mater., 32, 2201766.

[10] Zhu, P., Yang, W., Wang, R., Gao, S., Li, B., & Li, Q. (2018). Asymmetric actuation in thin film composite hydrogels. ACS Applied Materials and Interfaces, 10, 36435–36442.

[11] Wang, G., & Zhang, J. (2012). Photoresponsive polymer materials: Light-induced reversible changes of their optical and physical properties. Journal of Photochemistry and Photobiology C: Photochemistry Reviews, 13, 299–309.

12] Pilz Da Cunha, M., van Thoor, E. A. J. A. J., Debije, M. G. G., Broer, D. J. J., & Schenning, A. P. H. J. P. H. J. (2019). Thermosensitive and Photoswitchable Liquid-Crystalline Polymer Networks Based on Azobenzene Functionalized Poly(ethylene glycol) and Poly(butylene terephthalate). Journal of Materials Chemistry C, 7(44), 13502–13509.

[13] White, T. J. (2018). Structured Soft Materials via Directed Folding. Journal of Polymer Science Part B: Polymer Physics, 56(11), 695–705.

[14] Lee, K. M., & White, T. J. (2011). Self-Healing Polymers from Supramolecular Interlocking of Polymer Chains. Polymers, 3(3), 1447–1457.

[15] Yamada, M., Kondo, M., Mamiya, J. I., Yu, Y., Kinoshita, M., Barrett, C. J., & Ikeda, T. (2008). Photomobile Polymer Materials: Towards Light-Driven Plastic Motors. Angewandte Chemie International Edition, 47(26), 4986–4988.

[16] Pilz da Cunha, M., Kandail, H. S., den Toonder, J. M. J., & Schenning, A. P. H. J. (2020). Anisotropic and Tunable Elasticity of Supramolecular Liquid-Crystalline Polymer Networks Based on Molecular Orientation. Proceedings of the National Academy of Sciences, 117(30), 17571–17577.

[17] Sun, D., Zhang, J., Li, H., Shi, Z., Meng, Q., Liu, S., Chen, J., & Liu, X. (2021). Light-Driven Soft Robots

with an On-Board Photothermal Evaporation Engine. Polymers, 13(11), Article 1889.

[18] Dong, L., & Zhao, Y. (2018). Advances in the Design and Application of Photoresponsive Liquid Crystalline Polymer Materials. Materials Chemistry Frontiers, 2(10), 1932–1943.

[19] Oscurato, S. L., Salvatore, M., Maddalena, P., & Ambrosio, A. (2018). Liquid Crystalline Elastomers: Recent Trends in Materials and Applications. Materials, 7(4), Article 59.

[20] White, T. J., & Broer, D. J. (2015). Dynamic control over shape and size of cholesteric liquid crystal elastomers. Nature Materials, 14(10), 1087-1098.

[21] Sol, J. A. H. P., Douma, R. F., Schenning, A. P. H. J., & Debije, M. G. (2022). Organic Light-Emitting Diodes with Enhanced Outcoupling Efficiency Enabled by Ordered Surface Gratings. Advanced Materials Technologies, n/a, 2200970.

[22] Ceamanos, L., Kahveci, Z., Lopez-Valdeolivas, M., Liu, D., Broer, D. J., & Sanchez-Somolinos, C. (2020). Color-tunable photonic polymer coatings based on cholesteric liquid crystals. ACS Applied Materials & Interfaces, 12(39), 44195-44204.

[23] Crespi, S., Simeth, N. A., & König, B. (2019). Photonic materials by the self-assembly of inorganic nanosheets. Nature Reviews Chemistry, 3(3), 133-146.

[24] Garcia-Amorós, J., Sánchez-Ferrer, A., Massad, W. A., Nonell, S., & Velasco, D. (2010). Singlet Oxygen Production in Liquid-Crystalline Azobenzene Derivatives. Physical Chemistry Chemical Physics, 12(44), 13238-13242.

[25] Gelebart, A. H., Mulder, D. J., Varga, M., Konya, A., Vantomme, G., Meijer, E. W., Selinger, R. L. B., & Broer, D. J. (2017). Making waves in a photoactive polymer film. Nature, 546(7656), 632-636.

[26] Garcia-Amorós, J., & Velasco, D. (2014). The role of ground-state dipole moment in photonic properties of liquid crystalline azobenzene derivatives. Physical Chemistry Chemical Physics, 16(7), 3108-3114.

[27] Wani, O. M., Verpaalen, R., Zeng, H., Priimagi, A., & Schenning, A. P. H. J. (2019). Dynamic control of structural color in a photoresponsive liquid crystalline polymer film with variable wavelength selectivity. Advanced Materials, 31(20), 1805985.

[28] Liu, Y., Xu, B., Sun, S., Wei, J., Wu, L., & Yu, Y. (2017). Phototunable multicolor molecular switches based on diarylethenes. Advanced Materials, 29(38), 1604792.

[29] Verpaalen, R. C. P., Pilz da Cunha, M., Engels, T. A. P., Debije, M. G., & Schenning, A. P. H. J. (2020). Liquid crystalline elastomer microstructures with programmed director orientation. Angewandte Chemie International Edition, 59(12), 4532-4536.

[30] Pilz da Cunha, M., Foelen, Y., van Raak, R. J. H., Murphy, J. N., Engels, T. A. P., Debije, M. G., & Schenning, A. P. H. J. (2019). An untethered magnetic- and light-responsive rotary gripper: shedding light on photoresponsive liquid crystal actuators. Adv. Opt. Mater., 7.

[31] del Pozo, M., Sol, J. A. H. P., van Uden, S. H. P., Peeketi, A. R., Lugger, S. J. D., Annabattula, R. K., Schenning, A. P. H. J., & Debije, M. G. (2021). Patterned Actuators via Direct Ink Writing of Liquid Crystals . 59381–59391. ACS Appl. Mater. Interfaces, 13.

CHAPTER 4

Light-induced reversible actuation of shape memory polymer for artificial muscles

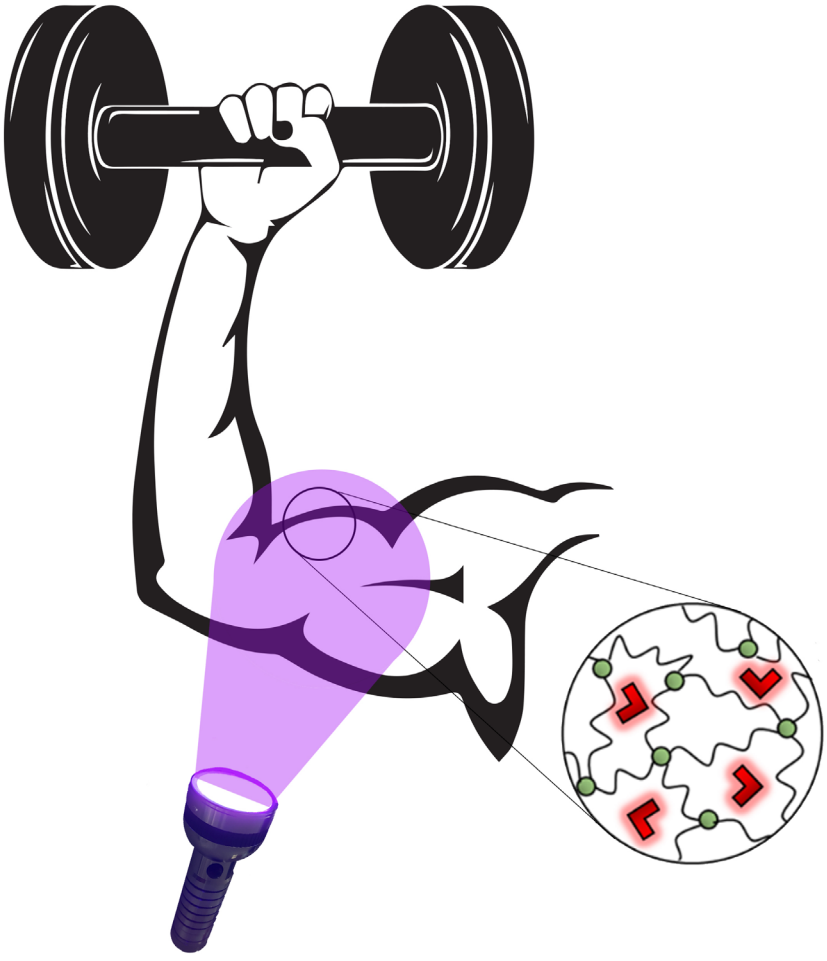

This project was carried out in collaboration with Michele Zanoni, Maurizio Toselli, Marco Montalti, Maria Letizia Focarete, Stefano Masiero and Chiara Gualandi.

Introduction

The interest in soft robotics has been growing steadily in recent years. Building soft actuators to develop precise machines that can overcome or assist human manufacturing ability represents a great challenge for the scientific community [1]. These devices aim to become technological innovations of various kinds that lead to the development of human "friendly robotics", at least partially replacing the rigid and non-ductile machines present in today's plants. Among various uses of soft actuators there is the conversion of energy from one form to another, ranging from the creation of mechanical energy from chemicals to the activation of artificial muscles by light [2]. Artificial muscles are of particular interest due to their multiple applications in both mechanical and clinical fields: in fact, they can replace various biological or mechanical components, carrying out reproducible processes with high energy conversion efficiency without showing any deterioration. Most of the artificial muscles described in the literature rely on shape memory polymers; these materials can keep a temporary shape and then recover the original one when subjected to an external stimulus such as magnetic field, moisture, light or heat [3]. The deformation in these polymers is driven by nanoscale molecular changes, which lead to macroscopic activation of the devices [4]. In light-triggered systems photoresponsive chromophores [5] can be used either as dopants or as monomers directly bonded to the polymer backbone. Azobenzenes (AZO) are interesting photoresponsive molecules, which can undergo a reversible photoinduced isomerization between their trans and cis configurations: this leads not only to an alteration of their physico-chemical characteristics but also to a change of shape, allowing them to drastically reduce their dimensions[6-7]. When azobenzenes are included into polymeric materials this change at the molecular level leads to a macroscopic variation of the morphology. During photoisomerization the azobenzenes not only change their configuration upon light absorption, but also release heat during the process.

Functionalized azobenzene cores have been chosen as the "power unit" of several devices such as transporters [8-11], motors [12], sensors [13] and artificial muscles [14]. Yet, these devices still show low energy conversion efficiency or very slow actuation. Thus, developing new photoresponsive functional materials represents an important goal.

The electrospinning technique was used to achieve this result. Electrospinning involves an electro-hydrodynamic process. A concentrated or semi-dilute polymer solution is placed in the syringe and pumped through a needle, on the tip of which a droplet is formed. The application of an electric field, generated by a high-voltage power supply (DC or AC), between the needle and the manifold is essential. Upon electrification, electrostatic repulsion between surface charges of the same sign deforms the droplet into a Taylor cone, from which a charged jet is ejected. Because the jet is charged, the electrostatic repulsion forces on the surface stretch the yarn; the high volume-to-surface area ratio allows rapid evaporation of the solvent. On the surface of the jet, the density of charges increases rapidly, resulting in an even stronger electrostatic repulsion effect that causes instability, so the yarn acquires a large-scale sussultatory motion. During propagation, the jet thins as the solvent evaporates until it reaches the collector in the form of fibers.

In this work we have selected a well-known system based on PCL [15,16] crosslinked with sol-gel reaction as a polymer to be used in electrospinning. It exploits the low-temperature crystal-melt transition for one-way and two-ways shape memory effect under a thermal stimulus. The photo-responsiveness has been conferred by adding an AZO compound that isomerizes during irradiation with UV light releasing heat. This photothermal effect has been exploited to develop light responsive actuators as thin films and as nonwovens made of microfibers. The reversible actuation of these systems has been thoroughly characterized and it was demonstrated that those materials could become functional in multiple fields.

Results and discussion

This shape memory system is based on a PCL network crosslinked through silica-based netpoints (**Figure 1a** and **1c**), both in form of thin film and electrospun mat. This system displays one-way and two-ways shape memory behavior under a thermal trigger. As a further development, to confer photo responsiveness, the system was doped with an AZO compound (**Figure 1a**). Azobenzene with short-lived cis isomer was proposed as photothermal-driven photo-switch, with the heat released by cis-trans isomerization fueling actuation [17]. The cis isomer lifetime can be reduced by adding an electron-donating and an electron-withdrawing substituent in 4 and 4' positions of the azobenzene core, generating a "push-pull" AZO [18-19]. The AZO compound selected for this work belongs to this category and can undergo a fast thermal cis-to-trans isomerization not only in solution but also in glassy and liquid-crystalline polymers [20].

The mode of action of the light-responsive shape memory actuators proposed in this work is schematically represented in **Figure 1**. Under UV irradiation (**Figure 1d**), the heat released by the trans-cis-trans cyclic isomerization locally increase the temperature of the polymer (**Figure 1e**), inducing the melting of PCL crystal phase (**Figure 1f**). The concentration of the AZO dopant was set at 4 %wt for both film and mat stripes. At this stage, the sample, subjected to an increasing load, experiences a decrease in Young's modulus and reaches a certain deformation (ε^1_{ON}, **Figure 1g**) that depends on the applied stress. By keeping the sample under a constant load, when light is turned off the temperature of the system decreases and the polymer crystallizes under stress, leading to the well-known phenomenon of crystallization-induced elongation (CIE) [21], reaching a higher value of strain ε^1_{OFF} (**Figure 1g**). By switching on the UV lamp, the PCL crystal phase melts again, leading to the melting-induced contraction (MIC) of the sample. This procedure can be repeated for many cycles (**Figure 1g**). The actuation reversibility depends on the stability of the crosslinking points and the fast cis-to-trans isomerization of the AZO dopant, that, once the light is turned off, allows a fast recovery of the initial trans state without the need of reconfiguring the system with visible light, as instead necessary for other AZOs systems, an example is reported in reference [22].

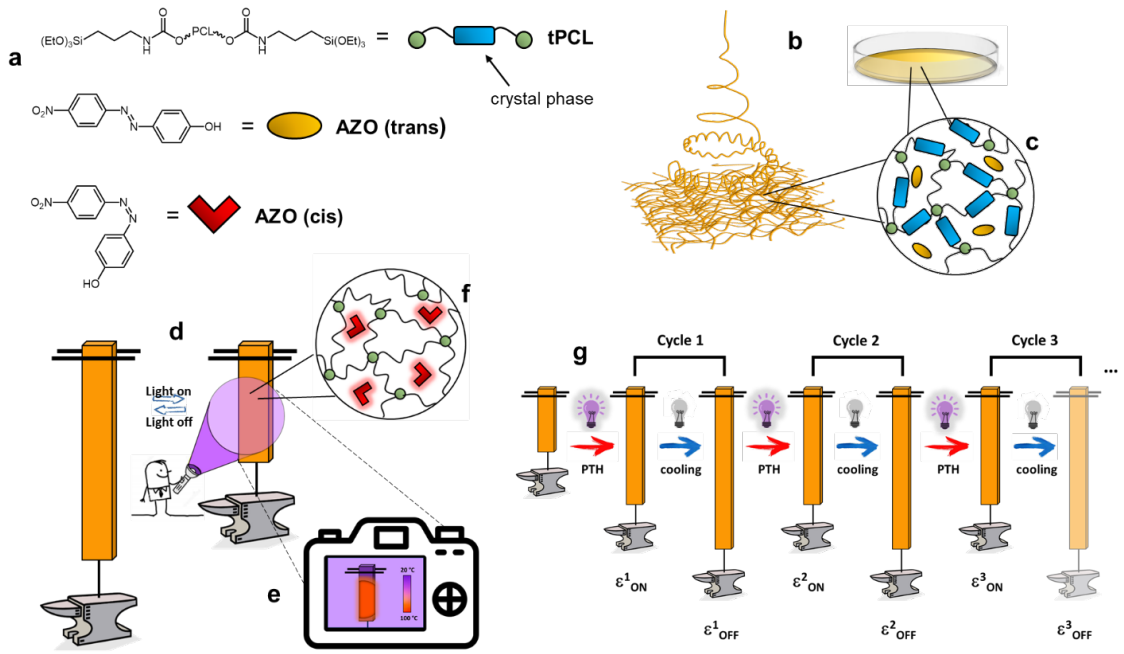

Figure 1. Sketch describing the photo-activated two-way shape memory system: (a) chemical structures of tPCL (poly-ε-caprolactone) and AZO (trans and cis forms) used to produce (b) non-woven mats (by electrospinning) and thin films (by solvent-casting); (c) the resulting materials consist of a network of chemically crosslinked semicrystalline PCL chains doped with 4wt% of AZO; (d) both systems are tested under a constant load for two-way shape memory behavior using UV irradiation while measuring the temperature of the sample with a thermal camera (e); UV light induces trans-to-cis isomerization of the dispersed AZO, whose cis form spontaneously reverts to the trans one releasing heat, with the consequent melting of PCL crystal phase (f); (g) both systems are tested up to 11 cycles by applying different pre-stretch strains, ε^1_{ON}.

Figure 2a-d reports representative SEM images of the electrospun fibers before and after the crosslinking treatment. The average fiber diameter does not significantly change after the crosslinking treatment and it is in the range 2-3 μm. Both electrospun mats and films show orange color (insets in **Figure 2e** and **2f**) due to the inclusion of AZO dopant. The presence of the AZO compound in the samples is also confirmed spectroscopy by ATR-IR. Indeed, the IR peaks characteristic of AZO (C-N stretching at 1605 cm^{-1}; aromatic C-C stretching at 1588 cm^{-1}; N-O asymmetric and symmetric stretching at 1516 and 1331 cm^{-1}, respectively; out-of-plane bending of aromatic C-H at 863 and 845 cm^{-1}) are clearly visible in tPCL-AZO-ES-Cr (crosslinked azo doped poly-ε-caprolacton electrospun mat) and tPCL-AZO-Film (azo doped poly-ε-caprolacton film), together with the peaks assigned to PCL (C=O stretching at 1723 cm^{-1}; C-O-C asymmetric and symmetric stretching at 1240 and 1162 cm^{-1}, respectively). Even if the AZO compound could participate in the sol-gel reaction, it can be easily removed when the samples are immersed in THF (see the loss of orange color in pictures of **Figure 2e** and **2f** and the disappearance of the AZO infrared peaks in tPCL-AZO-ES-Cr and tPCL-AZO-Film washed in THF), clearly demonstrating that it is not covalently linked to the polymeric network.

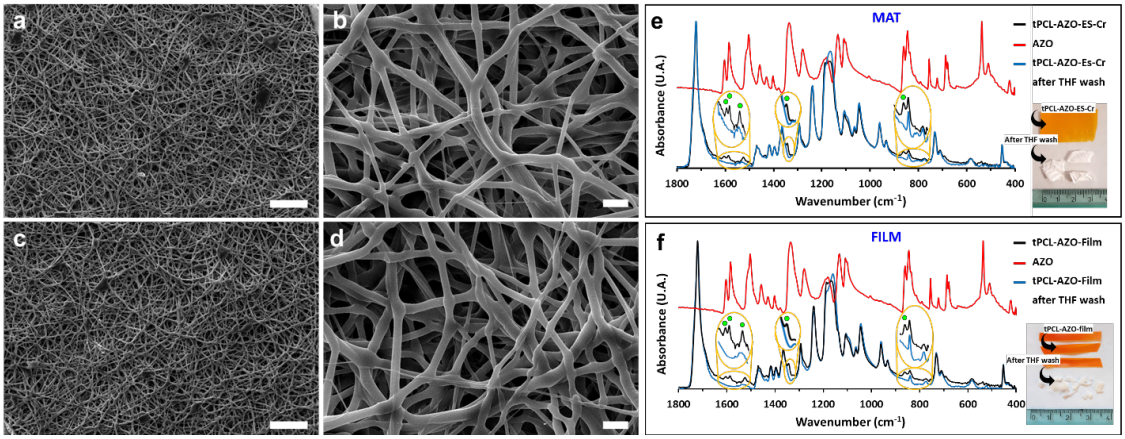

Figure 2. Representative SEM images of tPCL-AZO-ES (electospun AZO-doped poly-ε-caprolactone) (a, b) and tPCL-AZO-ES-Cr (crosslinked electospun AZO-doped poly-ε-caprolactone) (c, d). e) ATR-IR spectroscopy of tPCL-AZO-ES-Cr (black), the same sample after THF immersion (blue), and AZO compound (red); pictures of tPCL-AZO-ES-Cr before and after THF immersion are reported on the right. f) ATR-IR spectroscopy of tPCL-AZO-Film (crosslinked solvent-casted AZO-doped poly-ε-caprolactone) (black), the same sample after THF immersion (blue), and AZO compound (red); pictures of tPCL-AZO-Film before and after THF immersion are reported on the right.

As a general consideration, in two-ways shape memory systems, the extent of the actuation (ε_{OFF} - ε_{ON}) is governed by the amount of crystal phase that melts and crystallizes in the MIC and in the CIE phases, respectively. For those systems, the effectiveness of the crosslinking procedure was verified by DSC and gel content measures. **Figure 3** reports the DSC curves of tPCL-AZO-ES-Cr and tPCL-AZO-Film, together with tPCL-AZO-ES (azo doped poly-ε-caprolacton electrospun mat) to assess the effect of post-crosslinking on the fibers. For each sample the calorimetric data are reported in **Table 1**. Data related to the first heating scans are highly dependent on the different thermal histories of the samples, while the second heating scans allow a more reliable comparison between the samples and better represent the thermal behavior of the actuators since, before applying the pre-stretching, their thermal history is erased by melting above T_m. In the second heating scan, the melting enthalpy of tPCL-AZO-ES (ΔH_m = 63 J g^{-1}) decreases after post-crosslinking (ΔH_m = 51 J g^{-1}), resulting in the reduction of the crystallinity, showing a value similar to that of the film (ΔH_m = 54 J g^{-1}). This trend demonstrates the effectiveness of the post-crosslinking in improving the netpoint density in the mat, to reach a crosslinking degree comparable to that of the film. Indeed, the presence of netpoints reduces the local chain mobility necessary for crystal growth, similar to what is found when comparing tPCL-ES and crosslinked tPCL-ES-Cr. In **Figure 3** it is highlighted than the melting phenomenon for both crosslinked mat and film ends at 55°C in the 2nd heating scan (T_m^{end}, dashed black line). This aspect will be considered in the following discussion about the photothermal effect. The gel fraction, i.e. the insoluble portion of the sample, was in the range 88-95% for both systems. Being both gel content and melting enthalpy of the crosslinked film and mat similar, a direct comparison of actuation performance is thus possible.

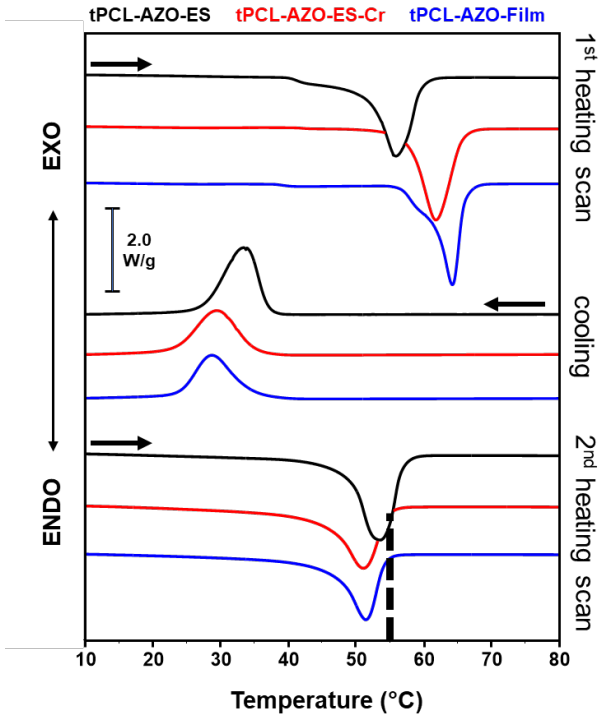

Figure 3. DSC 1st heating scans (top), cooling scans (middle), and 2nd heating scans (bottom) of tPCL-AZO-ES (black), tPCL-AZO-ES-Cr (red) and tPCL-AZO-Film (blue). The dashed black line crossing the 2nd heating scans at 55 °C indicated the end of the melting phenomenon for crosslinked mat and film (red and blue curves, respectively), T_m^{end} = 55°C.

	1st heating scan			*cooling*		*2nd heating scan*		
Sample	T_g [°C]	T_m [°C]	ΔH_m [J g^{-1}]	T_c [°C]	ΔH_c [J g^{-1}]	T_g [°C]	T_m [°C]	ΔH_m [J g^{-1}]
tPCL-AZO-ES	-51	56	85	33	63	-54	54	63
tPCL-AZO-ES-Cr	-51	62	72	28	51	-53	51	51
tPCL-AZO-Film	-54	64	73	29	51	-51	51	54

Table 1. Relevant calorimetric data of tPCL-AZO samples (before and after the post-crosslinking) and film.

In shape memory azo-based materials activated by the photothermal effect, the intensity of the radiation is another parameter that affects the actuation since it influences the sample temperature [23]. The photothermal effect promoted by the AZO on crosslinked PCL film and mat has been recorded at different radiation intensities, by changing the distance of the UV source from the samples. A thermal camera was used to measure the temperature of the stripes both on the side directly illuminated by the lamp (front) and on the opposite one (back). For both samples (e.g. film and mat), when the lamp is turned on, the temperature of the two surfaces immediately rises, reaching a plateau value after about 15 and 10 seconds on the front and back sides, respectively, albeit at the greater distances the temperature takes a bit more time

to stabilize over a constant value (**Figure 4**). As expected, the closer the sample to the UV source the higher the temperature. When the light is turned off, the temperature rapidly decreases. **Figure 4a** and **b** report the plateau temperatures measured on the front and back sides of both mat and film as a function of light intensity and distance from the UV source, respectively. The temperature is linearly correlated with the light intensity and the value measured on the side under direct irradiation is significantly higher than that on the back side. Interestingly, this temperature gradient across sample thickness is remarkably higher in the mat than in the film. Moreover, by keeping constant the distance from the lamp, the temperature of the irradiated side of the mat is higher than the one of the film. These results are somehow counterintuitive, as one would expect, by comparing mat and film, that the highly porous mat should display a lower temperature at the front side, because of a lower AZO density per unit area. Moreover, since the AZO density per unit volume is lower in the porous mat compared to the film, a lower temperature gradient is expected in the mat, because of a lower light absorption across the sample. These opposite results can be rationalized by considering the optical behaviour of electrospun mats, known to be highly reflective thanks to their ability to scatter light. Multiple absorption of reflected UV light can thus justify the higher temperature recorded at the front surface of the mat compared to the film. The higher temperature gradient recorder for the mat can instead be explained by the low thermal diffusivity of the air entrapped within mat pores, which contributes to thermally isolating the cold back side of the mat from the hot front side.

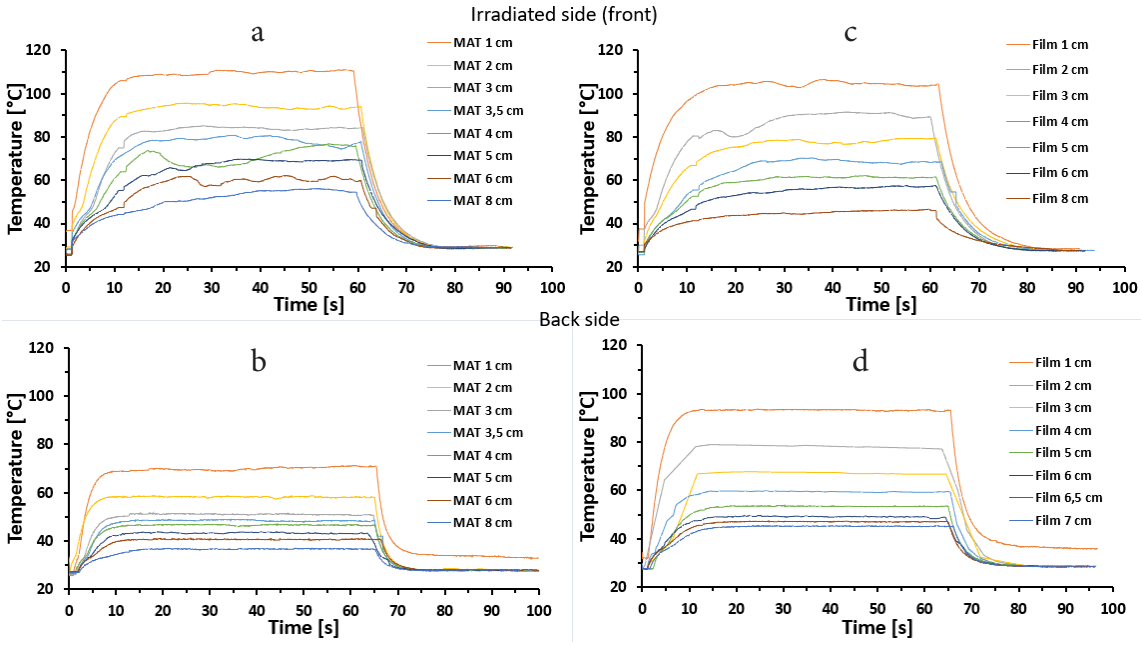

Figure 4. Temperature at the surface of the sample measured by the thermal camera as a function of time and by positioning the lamp at different distances from the sample. The UV light was turned on a t = 0 s and turned off at t = 60 s: a) front side of electrospun mat; b) back side of the electrospun mat; c) front side of the film; d) bask side of the film.

The most important consequence of the photothermal effect is the melting of PCL crystal phase and, consequently, the change of sample mechanical properties. **Figure 5** shows the tensile stress-strain curves for the mat and the film. It is evident that both samples experience a large decrease in Young's modulus and strength under UV light. Interestingly, the mat displays

a progressive reduction of mechanical properties by decreasing lamp distance from 6 to 5 cm, while from 4 cm onwards the stress-strain curves are overlapped. In contrast, the maximum reduction of film mechanical properties occurs already at 6 cm and the decrease of lamp distance does not contribute to further reducing the mechanical properties.

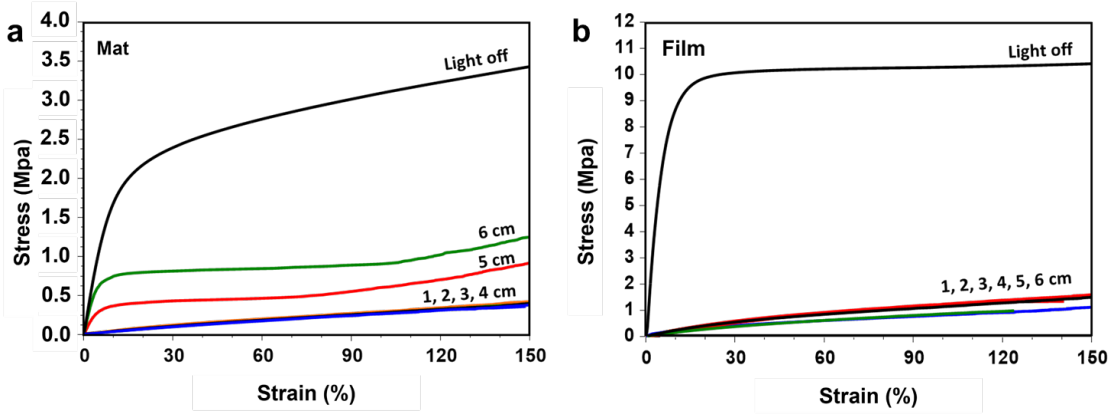

Figure 5. Stress-strain curves of (a) electrospun mat tPCL-AZO-ES-Cr and of (b) tPCL-AZO-Film determined under UV irradiation positioning the lamp at different distances from the sample.

This is evident by considering how the Young's modulus of film and mat changes as a function of light intensity and lamp distance **(Figure 6c** and **6d**, respectively). This different trend of the elastic moduli is ascribable to the above explained photothermal behavior and can be easily rationalized by considering the average temperature (T_{aver}) reached by the samples irradiated at different distances (**Figure 6b**, dashed curves). The T_{aver} of the film is always higher than 55°C (T_m^{end} of PCL melting), differently the T_{aver} of the mat is higher than 55°C at distances shorter than 4 cm. In other words, at large distances the PCL crystal phase in the fibers is not entirely melted. The data related to the photothermal effect allowed us to properly set up the experimental conditions for actuation experiments. The most critical parameter is the distance between the sample and the UV source as it determines both the light intensity, thus the sample temperature, and the light spot size, thus the portion of the sample that can effectively be photoactivated. In order to maximize the spot size and to ensure the complete melting of PCL crystal phase in both film and mat leading to uneven contraction, the actuation experiments were carried out by positioning the UV lamp at 3.5 cm from the samples to ensure a high enough light intensity to melt PCL crystal and a spot dimension big enough to irradiate all the sample between DMTA (Dynamic Mechanical Thermal Analysis) clamps.

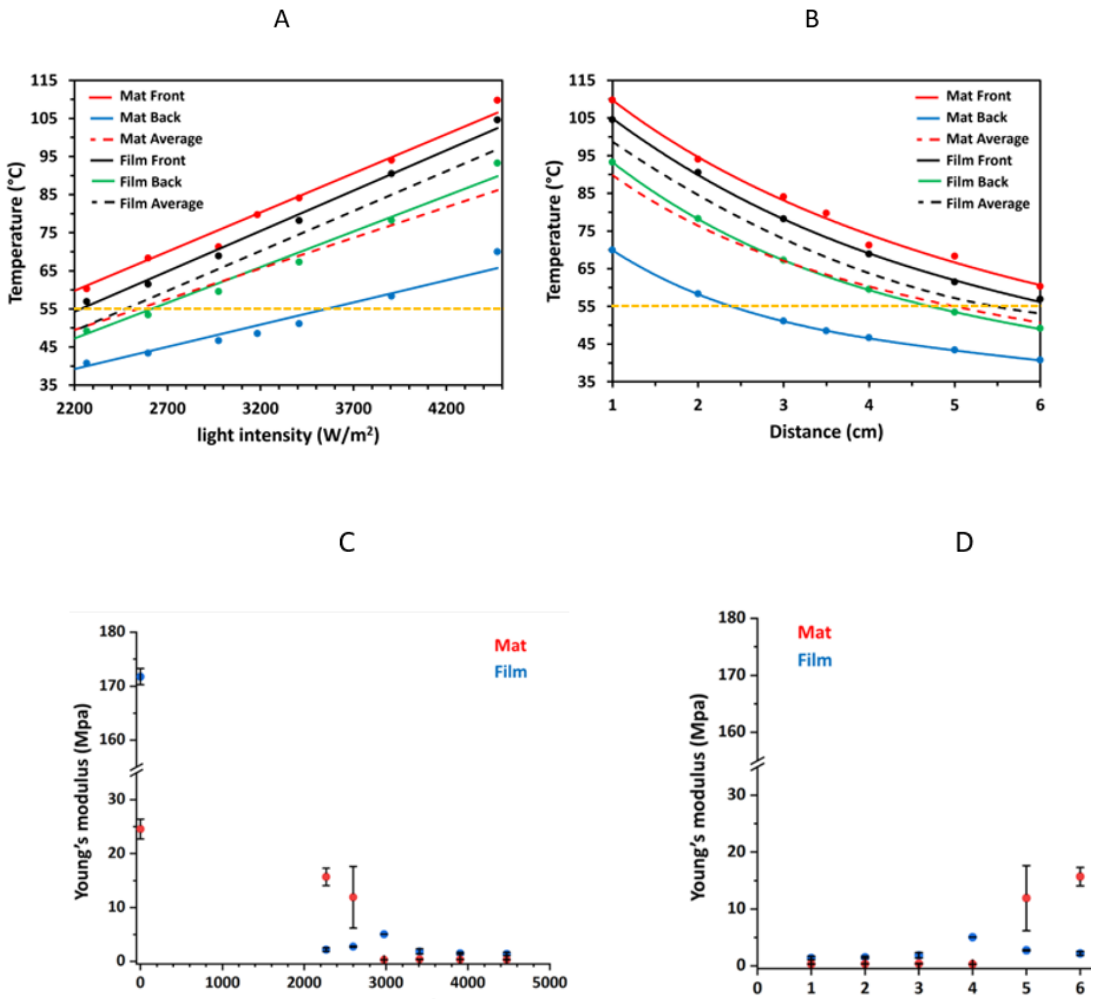

Figure 6. Temperature of tPCL-AZO-ES-Cr electrospun mat (red) and of tPCL-AZO-Film (blue) measured by the thermal camera both on the front and back sides of UV-irradiated samples: A) T as a function of light intensity and B) T as a function of lamp distance. Young's moduli of UV-irradiated samples of tPCL-AZO-ES-Cr electrospun mat (red) and of tPCL-AZO-Film (blue) as a function of light intensity (C) and as a function of lamp distance (D).

Stress-strain test, actuation and device assembly

Tensile stress-strain tests and two-ways shape memory actuation were carried out on tPCL-AZO-ES-Cr and tPCL-AZO-Film. The samples were cut as rectangular strips (20 mm length x 5mm width), heated at 80 °C, allowed to shrink to constant length, then cooled to RT. For a correct evaluation of mechanical performance and reliable comparison between the different samples, this treatment is needed to stabilize the dimension of the electrospun specimens that present a significant contraction at first heating above T_m, due to relaxation of the oriented chain segments. Tensile stress-strain measurements were performed by DMTA, a preload force of 0.005 N was used and a ramp force of 0.15 N min^{-1} was set. As shown in **Figure 5**, both mat and film can undergo several irradiation cycles (light on 6 s, light off 30 s) maintaining their efficiency and without showing any signs of fatigue at different pre-stretch values (ε^1_{ON}).

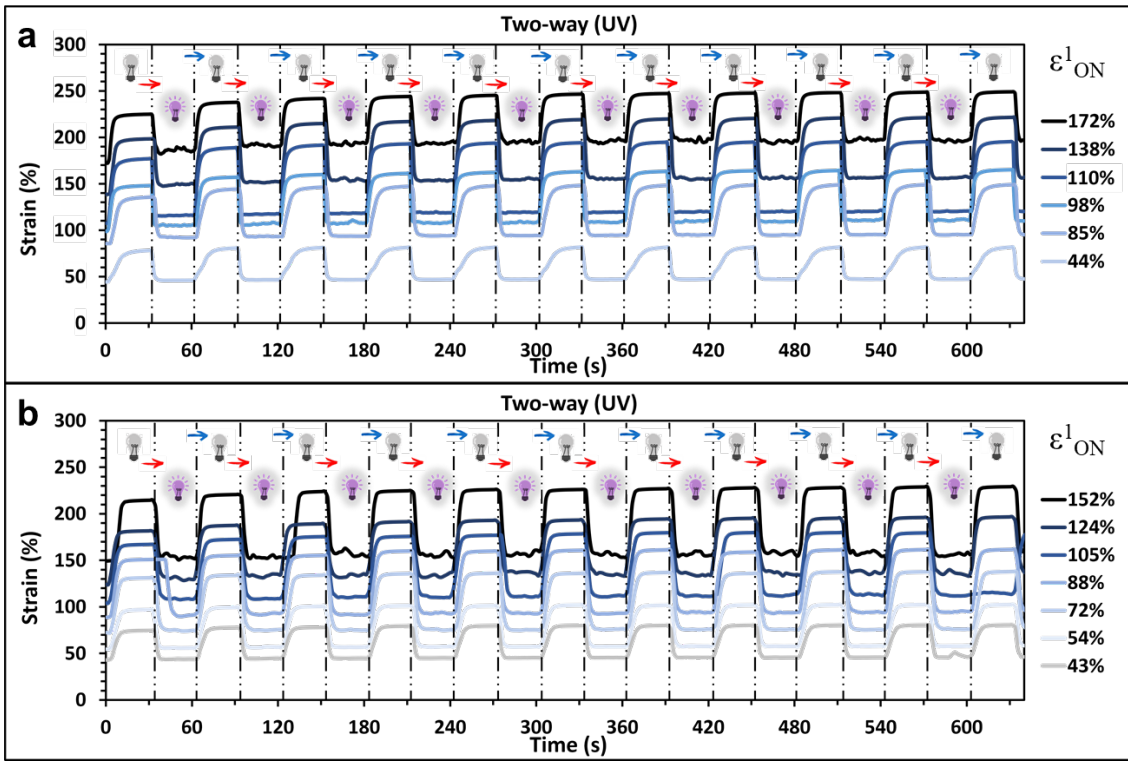

Figure 7. Actuation experiments performed on tPCL-AZO-ES-Cr electrospun mat (a) and on tPCL-AZO-Film (b) by applying different stresses to achieve different values of pre-stretch (ε^1_{ON}). In each experiment the stress was kept constant while the UV lamp was alternatively turned on and off every 30 s, over 11 cycles.

The stress produced by the shape memory polymer contraction during irradiation was evaluated as a function of the % pre-stretch values. Mat showed a stress increase proportional to % pre-stretch values: remarkably, it turns out to be able to work at regimes similar to that of a human muscle. Film showed much better performance in strength, but the correlation with pre-stretch values is not linear, as shown in **Figure 8**.

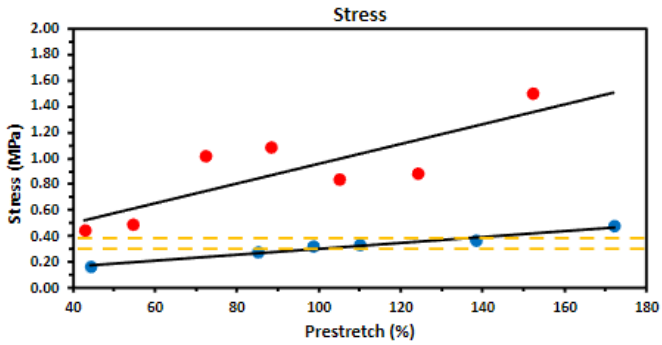

Figure 8 Produced stress in tPCL-AZO-ES-Cr electrospun mat (Blue) and tPCL-AZO-Film (red) as a function of % pre-stretch value. The dashed yellow line represents the values expressed by human muscle.

To Exploit the efficiency of this innovative polymer, a home-made wireless lifter in the form of a class one lever was fabricated as a model of practical application in soft robotics. A swinging wooden arm (total length 22 cm, made of wooden sticks) was anchored to a circular iron bar, the latter acting as the fulcrum. The fulcrum was not positioned at the center of the wooden arm, but 9 cm from one end. A hook was placed at the end of the long arm (13 cm) to hang a weight; therefore a perfectly balanced lever was created (**Figure 9A**). The photoresponsive polymer stripe tPCL-AZO-ES-Cr (5 x 0.5 cm) was glued between the base of the device and the short arm of the lever at 1 cm from the fulcrum: this is not the most advantageus positioning of the effort force. The UV lamp was placed at 3.5 cm distance from the photoactive polymer (**Figure 9B**), to perform the irradiation cycles under the best conditions identified by DMTA, and a 4 g weight was attached to the hook. After a first irradiation to obtain the pre-stretch necessary for a correct actuation, the device was able to repeatedly lift the weight to a height of 10 cm (**Figure 10**). Actuation cycles of the device are shown in **Video 1**.

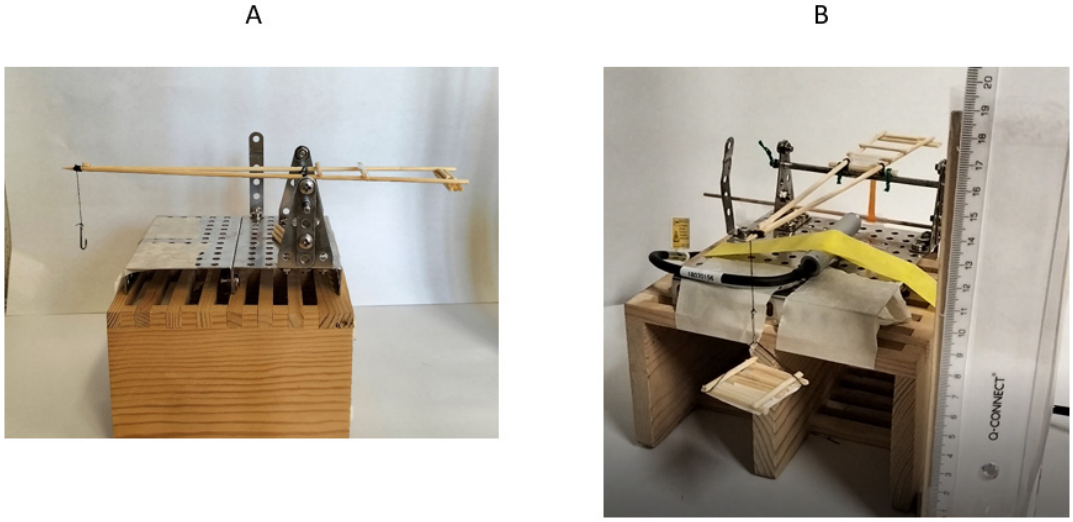

Figure 9. A) Free-standing balanced lever B) Assembled elevator

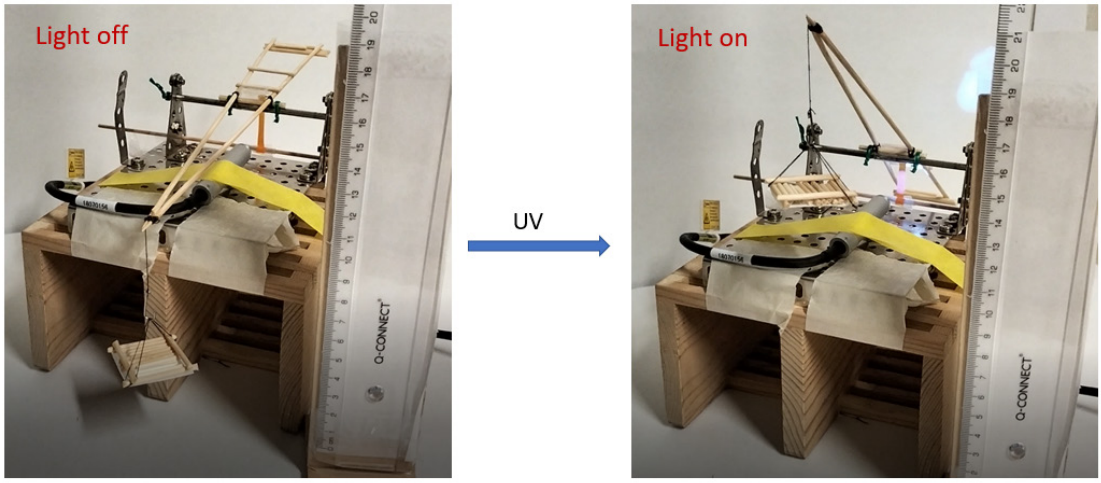

Figure 10. Device actuation. Contraction of the polymer (90 mg) leads to a 4 g counterweight lift of about 10 cm.

Conclusion

Combining a shape-memory polymer with a photoresponsive azobenzene-based dopant, an innovative artificial muscle was manufactured. The polymeric material was fabricated following two different methods, electrospinning and solvent casting, obtaining a nonwoven made up of microfibers and a uniform film, respectively. Both samples are triggered by UV irradiation, but have different characteristics; in fact the film generate a greater but inconstant stress during irradiation and can be exploited the soft-robotic industry to carry high loads, while the mat has a behavior similar to a human muscle and may find applications in the clinical field.

Experimental section

Materials

α,ω-Triethoxysilane-terminated poly(ε-caprolactone) (tPCL, **Figure1**a) was synthesized starting from an α,ω-hydroxyl-terminated poly(ε-caprolactone) (M_n = 10000 g mol^{-1}) and 3-(triethoxysilyl)propyl isocyanate (ICPTS), as previously reported by Paderni *et al*. [24]. Other reagents and solvents were purchased from Merck and used without any further purification.

Synthesis of 4-(4-nitrophenylazoyl)-phenol) (AZO). This compound was prepared according to a previously reported procedure. 4-Nitroaniline (3 g, 0.022 mol) was added to a hydrochloric acid aqueous solution (10%, 50 mL) and was stirred until dissolution was complete. Sodium nitrite (1.95 g, 0.029 mol) was dissolved in water (40 mL). Both solutions were cooled in an ice bath, then the nitrite solution was added dropwise to the aniline solution within 1 h, then stirred for another 30 min, keeping the temperature below 0 °C. Phenol (2.66 g, 0.028 mol) and sodium hydroxide (1.11 g, 0.028 mol) were dissolved in water (40 mL) and the resulting solution was cooled in an ice bath. The diazonium salt solution was added dropwise to the phenol one within 1 h, keeping the temperature below 0 °C. The reaction was left under stirring for another 3 h below 2 °C the left at room temperature for 24 h. A dark orange product precipitated and was collected by filtration to afford the title compound. Yield: 96%. Mp: 218–220 °C.

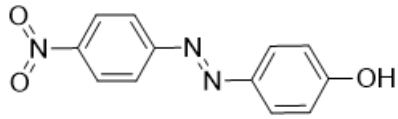

Preparation of tPCL-AZO-ES mats. The home-made electrospinning apparatus was composed of a SL 50 P10/CE/230 high-voltage power supplier (Spellman, New York, USA), a KDS-200 syringe pump (KDScientific Inc., Massachusetts, USA), a glass syringe containing the polymer solution, a stainless-steel needle (with an inner diameter of 0.5 mm) connected with the power supply electrode set at 15 kV, and a grounded plate collector positioned at a distance of 25 cm from the needle. tPCL was dissolved in a mixture of THF:DMF (80/20 v/v) at a concentration of 30 % w/v by stirring for 2 h at room temperature. After complete dissolution, the AZO compound was added to the solution to get a final concentration of 4

%wt in the fibers. The solution was transferred to the syringe and pumped out at the rate of 0.5 mL h^{-1}. The obtained mat, labelled tPCL-AZO ES, was stored in an oven to complete the sol-gel reaction, in the presence of an acid environment, at 50 °C for 72 h (post-crossliking). To this aim, the mat was hung to a glass rod at the top of a 500 mL beaker. The beaker was filled with 100 mL of distilled water and 3 mL of HCl 37%. The electrospun mat was not in direct contact with the acid solution but only with its acidic steams. The final crosslinked mat was labelled tPCL-AZO-ES-Cr.

Preparation of tPCL-AZO Film. tPCL was dissolved in THF at a concentration of 13 % w/v. Water, ethanol and HCl were added at the following molar ratios EtO: EtOH: H_2O: HCl = 1: 1: 1: 0.01. In a typical preparation, 0.78 g of PCL were dissolved in 6 ml of THF and stirred at RT for 2 h. After the complete dissolution of the polymer, 4.2 mg of HCl 3.7%, 19.7 mg of EtOH, 3.7 mg of H_2O and 31.5 mg of AZO compound were added and stirred at RT for 10 min. The final concentration of AZO in the film was 4 wt%. The solution was transferred into a silicone petri dish and covered with a watch glass for 6 h. Then the watch glass was removed, and the film was left to dry overnight. The sol-gel reaction was carried out in oven at 50 ° C for 72 h. The obtained film was labelled tPCL-AZO-F-Cr.

Gel content. Specimens of tPCL mats and film were weighed to get their initial weight (m_0) and then immersed in 15 mL of THF. After 2 h the THF was replaced with fresh THF and further stirred for 10 min.: this step was repeated twice. The samples were then dried under vacuum for 1 h and weighed to determine the residual mass (m_d). The gel content (G) was then calculated according to Equation 1:

$$G = \frac{m_d}{m_0} \times 100 \quad \text{Eq. [1]}$$

Characterization methods. ***Scanning Electron Microscopy.*** Sample morphology was observed with a scanning electron microscope (SEM, Leica Cambridge Stereoscan 360) at an accelerating voltage of 20 kV. Before SEM analysis, the samples were sputtered with gold. The distribution of fibre diameters was determined through the measurement of about 200 fibres and the results are given as the average diameter ± standard error of the mean (sem).

Fourier-transform infrared spectroscopy. FTIR spectra were collected using a BRUKER model ALPHA spectrophotometer equipped with ATR in the range 4000-400 cm^{-1} with a resolution of 3 cm^{-1}.

Differential Scanning Calorimetry. DSC measurements were carried out using a TA Instruments Q2000 DSC, equipped with a Refrigered Cooling System (RCS). Samples were subjected to a first heating scan at 10 °C min^{-1} from -90°C to 120 °C, a controlled cooling at 10 °C min^{-1} down to -90 °C and a second heating scan at 10 °C min^{-1}, under nitrogen atmosphere. The melting (T_m) and the crystallization (T_c) temperatures were determined. The melting enthalpy (ΔH_m) was also measured, and the crystallinity content (χ_c) was evaluated by considering the ΔH_m of a 100% crystalline PCL equal to 134.9 J g^{-1} [25].

Actuation tests were performed by irradiating the samples using a UV lamp (Hamamatsu LC-L1V3, 365 nm). The light intensity at different distances from the lamp was measured by using a luxometer (DeltaOHM, HD 2302.0).

The photothermal effect was assessed by using a thermal camera (Optris Xi 400). Preliminary to the mechanical tests, a series of experiments were performed on both tPCL-AZO-ES-Cr and tPCL-AZO-Film to record the temperature of the samples under UV light. To this aim, the lamp was positioned at different distances from the sample and the thermal camera was used to record the temperature of the sample's side directly irradiated by the lamp and subsequently to record the temperature of the sample back side.

Tensile stress-strain. Tensile stress-strain measurements were performed by using a Dynamic Mechanical Thermal Analyzer (DMTA, TA Instruments Q800 series) equipped with tension-film clamps. Stress-strain measurements were carried out at RT under UV irradiation at different lamp distances. Moreover, stress-strain measurements were carried out under different controlled temperatures. In this case, the sample was heated to the desired temperature and allowed to equilibrate for 5 min before beginning the test. A preload force of 0.005 N was used and a ramp forse of 0.15 N min^{-1} was set.

Two-way shape memory tests. Specimens were subjected to two-way shape memory cycles using the DMA apparatus working under load control and using the UV lamp positioned 35 mm away from the specimen. For each measurement the following steps were applied: (1) the lamp was turned on (photothermal heating); (2) the specimen was deformed (loading rate: 0.15 N min^{-1}) up to various levels of pre-strech strain, named prestretch, ε^1_{ON}; (3) the load approached at the end of the deformation step was kept constant; (4) the lamp was turned off for 30 sec (cooling), reaching the deformation ε^1_{OFF}; (5) by maintaining the fixed load conditions, the lamp was turned on again for 30 sec (photothermal heating). The steps 3-5 were repeated 11 times. The materials were tested under different loading conditions, set with the intent to apply different ε^1_{ON} to the same sample. The two-way shape-memory performance was quantified, as suggested in the literature [26], by calculating the absolute magnitude of strain change during cooling, typically referred to as actuation magnitude ($\Delta\varepsilon_{act}$) and during photothermal heating ($\Delta\varepsilon_{PTH}$), typically referred to as actuation magnitudes, as follows:

$$\Delta\varepsilon_{COOL} = \varepsilon^N_{OFF} - \varepsilon^N_{ON} \quad \text{Eq. [2]}$$

$$\Delta\varepsilon_{PTH} = \varepsilon^N_{OFF} - \varepsilon^{N+1}_{ON} \quad \text{Eq. [3]}$$

Multimedia Files

Video 1. Lifter actuation

References

[1] Schmitt, F., Piccin, O., Barbé, L., & Bayle, B. (2018). Soft robots manufacturing: A review. Frontiers in Robotics and AI, 5, 84.

[2] Koerner, H., White, T. J., Tabiryan, N. V., Bunning, T. J., & Vaia, R. A. (2008). Photogenerating work from polymers. Materials Today, 11(7-8), 34-42.

[3] Xia, Y., He, Y., Zhang, F., Liu, Y., & Leng, J. (2021). A review of shape memory polymers and composites: Mechanisms, materials, and applications. Advanced Materials, 33, 2000713.

[4] Lancia, F., Ryabchun, A., Nguindjel, A. D., Kwangmettatam, S., & Katsonis, N. (2019). Mechanical adaptability of artificial muscles from nanoscale molecular action. Nature Communications, 10, 4819.

[5] Wang, G., & Zhang, J. (2007). Photoresponsive molecular switches for biotechnology. Organic Letters, 9(20), 3865-3868.

[6] Schultz, T., Quenneville, J., Levine, B., Toniolo, A., Martínez, T. J., Lochbrunner, S., Schmitt, M., Shaffer, J. P., Zgierski, M. Z., & Stolow, A. (2003). Mechanism and dynamics of azobenzene photoisomerization. Journal of the American Chemical Society, 125(27), 8098-8099.

[7] Henzl, J., Mehlhorn, M., Gawronski, H., Rieder, K. H., & Morgenstern, K. (2006). Reversible cis-trans isomerization of a single azobenzene molecule. Angewandte Chemie International Edition, 45(4), 603-606.

[8] Pilz da Cunha, M., Kandail, H. S., den Toonder, J. M. J., & Schenning, A. P. H. J. (2020). An artificial aquatic polyp that wirelessly attracts, grasps, and releases objects. Proceedings of the National Academy of Sciences of the United States of America, 117(30), 17571-17577.

[9] Pilz da Cunha, M., Foelen, Y., Engels, T. A. P., Papamichou, K., Hagenbeek, M., Debije, M. G., Schenning, A. P. H. J. (2019). On Untethered, Dual Magneto- and Photoresponsive Liquid Crystal Bilayer Actuators Showing Bending and Rotating Motion. Advanced Optical Materials, 7, 1801604.

[10] Pilz da Cunha, M., Ambergen, S., Debije, M. G., Homburg, E. F. G. A., den, J. M. J., Schenning, A. P. H. J. (2020). A Soft Transporter Robot Fueled by Light. Adv. Sci., 7, 1902842.

[11] Yamada, M., Kondo, M., Mamiya, J., Yu, Y., Kinoshita, M., Barrett, C. J., & Ikeda, T. (2008). Photomobile polymer materials: towards light-driven plastic motors. Angewandte Chemie International Edition, 47(27), 4986-4988.

[12] Pozo, M. D., Sol, J. A. H. P., van Uden, S. H. P., Peeketi, A. R., Lugger, S. J. D., Annabattula, R. K., Schenning, A. P. H. J., & Debije, M. G. (2021). Patterned Actuators via Direct Ink Writing of Liquid Crystals. ACS Applied Materials & Interfaces, 13(49), 59381-59391.

[13] López-Valdeolivas, M., Liu, D., Broer, D. J., & Sánchez-Somolinos, C. (2018). 4D Printed Actuators with Soft-Robotic Functions . Macromolecular Rapid Communications, 39, 1700710.

[14] Guo, X., Mao, T., Wang, Z., Cheng, P., Chen, Y., Ma, S., & Zhang, Z. (2020). Fabrication of Photoresponsive Crystalline Artificial Muscles Based on PEGylated Covalent Organic Framework Membranes. ACS Central Science, 6(5), 787-794.

[15] Merlettini, A., Pandini, S., Agnelli, S., Gualandi, C., Paderni, K., Messori, M., Toselli, M., & Focarete, M. L. (2016). Facile fabrication of shape memory poly(ε-caprolactone) non-woven mat by combining electrospinning and sol–gel reaction. RSC Advances, 6, 43964-43974.

[16] Pandini, S., Agnelli, S., Merlettini, A., Chiellini, F., Gualandi, C., Paderni, K., Focarete, M. L., Messori, M., & Toselli, M. (2017). Thermoactive Smart Electrospun Nanofibers. Macromolecular Materials and Engineering, 302, 1600519.

[17] Gelebart, A., Jan Mulder, D., Varga, M., et al. (2017). Making waves in a photoactive polymer film. Nature, 546, 632–636.

[18] Aleotti, F., Nenov, A., Salvigni, L., Bonfanti, M., El-Tahawy, M. M., Giunchi, A., ... Conti, I. (2020). Spectral tuning and photoisomerization efficiency in push-pull azobenzenes: Designing principles. Journal of Physical Chemistry A, 124(46), 9513-9523.

[19] Gentile, M., Spallacci, C., Ventimiglia, A., Cirillo, G., Montali, L., Scurti, S., ... Conti, I. (2020). Spectral Tuning and Photoisomerization Efficiency in Push−Pull Azobenzenes: Designing Principles. J. Phys. Chem. A, 124, 9513−9523.

[20] Garcia-Amoros, J., & Velasco, D. (2014). Understanding the fast thermal isomerisation of azophenols in glassy and liquid-crystalline polymers. Physical Chemistry Chemical Physics, 16, 3108-3114.

[21] Brüning, K., Schneider, K., Roth, S. V., & Heinrich, G. (2012). Kinetics of strain-induced crystallization in natural rubber studied by WAXD: Dynamic and impact tensile experiments. Macromolecules, 45(19), 7914-7919.

[22] Lahikainen, M., Zeng, H., & Priimagi, A. (2018). Reconfigurable photoactuator through synergistic use of photochemical and photothermal effects. Nature Communications, 9, 4148.

[23] Pilz da Cunha, M., van Thoor, E. A. J., Debije, M. G., Broer, D. J., & Schenning, A. P. H. J. (2019). Unravelling the photothermal and photomechanical contributions to actuation of azobenzene-doped liquid crystal polymers in air and water. Journal of Materials Chemistry C, 7, 13502-13509.

[24] Paderni, K., Pandini, S., Passera, S., et al. (2012). Shape-memory polymer networks from sol-gel cross-linked alkoxysilane-terminated poly(ε-caprolactone). Journal of Materials Science, 47, 4354-4362.

[25] Miller, R. L. (1992). Crystallographic data for various polymers. In Polymer Handbook (3rd ed., pp. 519-540). John Wiley & Sons.

[26] Chung, T., Romo-Uribe, A., & Mather, P. T. (2008). Two-way reversible shape memory in a semicrystalline network. Macromolecules, 41(1), 184–192.

Guanosines.

Unity is strength!

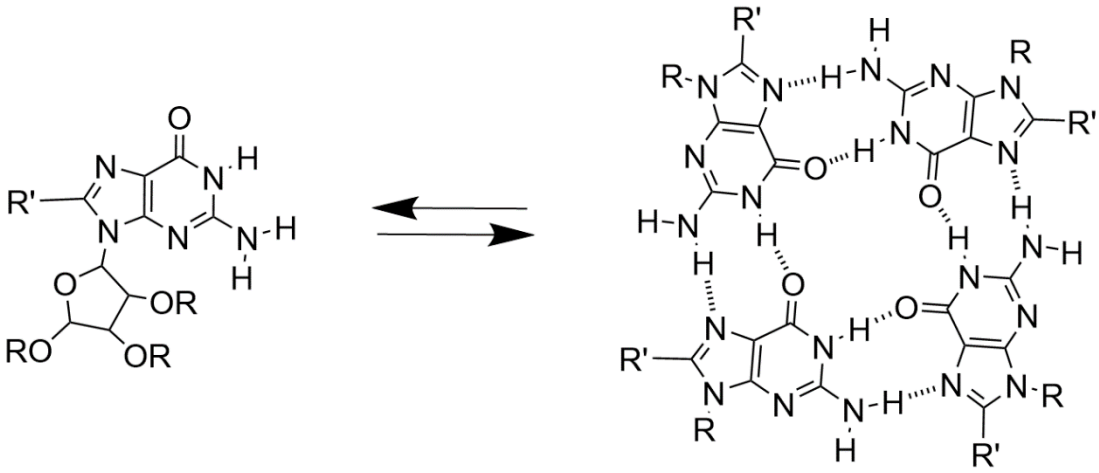

Summary

Although the large variety of supramolecular networks originated by guanosine derivatives has been investigated for a couple of decades, only in recent years research focused on their use in supramolecular chemistry. Guanine moiety is a versatile hydrogen bonding building block. In particular, lipophilic guanosines or guanines can undergo different self-assembly pathways, originating different architectures depending on environmental conditions. Typical assembly structures are ribbons and cyclic G-quartet systems. Furthemore, functionalizing guanosines with sugar hydroxyl groups and aromatic base is quite simple: this makes them a promising building block for the fabrications of complex architectures with functional units located in predetermined positions [1].

Self-assembly of lipophilic guanosines

Self-assembly templated by cation

The ability of guanosines to give supramolecular structures is not limited to the aqueous phase: parallel studies have been carried out on lipophilic derivatives of these molecules (lipoG) to investigate their behavior in organic solvents. These studies led G. Gottarelli and co-workers in 1995 [2] to the demonstration that lipophilic derivatives are capable of extracting ions from aqueous phase to organic solvent: in particular, placing the lipophilic derivative 3',5'-didecanoyl-2'-dG dissolved in chloroform in a test tube in contact with an aqueous solution of K^+ picrate and shaking vigorously, the transfer of the typical yellow coloration of picrate from the aqueous phase to the organic phase is achieved (**Figure 1**).

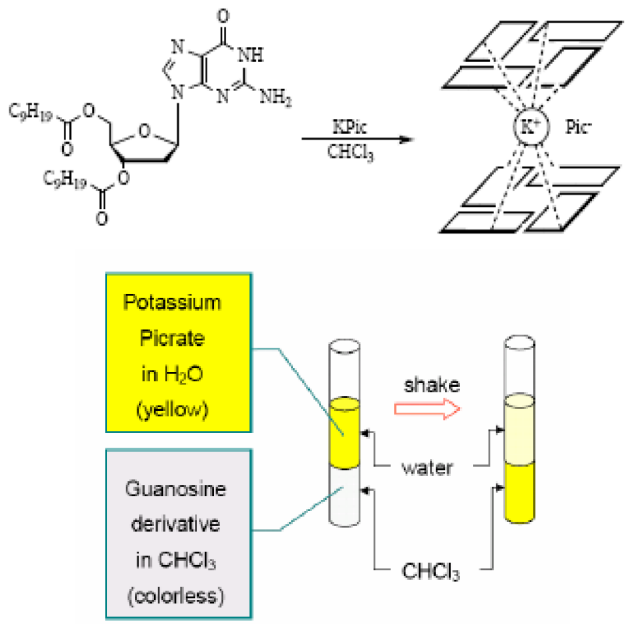

Figure 1. Extraction of ions from the aqueous phase to the organic phase by lipophilic guanosines.

Formation of lipophilic guanosine octamers takes place; each individual quartet consists of guanosine monomers that interact with each other through hydrogen bonds on Hoogsten and Watson-Crick faces: the presence of the ion is essential for multiple quartets of lipoGs to stack on top of each other. This allows lipoGs to be defined as ionophores, although such behavior requires the presence of at least two quartets, which form structures of greater complexity simultaneously with ion capture. Research in this direction, supported by NMR studies, has shown how a well-defined ratio of ion to lipoG is crucial in discriminating between the formation of single octamers and assembly into true pseudopolymers (**Figure 2**).

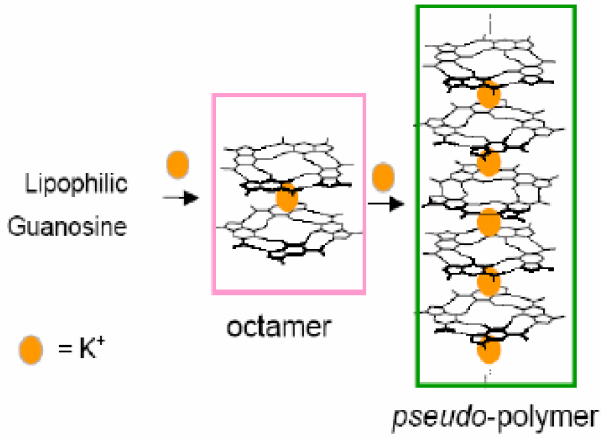

Figure 2. Formation of octamers and pseudopolymers resulting from the self-assembly of lipophilic guanosines in the presence of cation.

It was later shown that such supramolecular aggregates are formed due to the presence of the cation, but are stabilized strongly by the picrate anion [3]. **Figure 3** shows the quadruplex obtained by self-assembly of monomers of 5'-tert-butyldimethylsilyl-2',3'-isopropylidenguanosine, following extraction of K^+ ions from an aqueous solution to a methylene chloride one. In such a structure, each octamer exploits the core-oriented carbonyl oxygens to coordinate a potassium ion: a third ion binds the octamers together, a cesium ion closes the structure, and four picrate anions form hydrogen bonds, reinforced by negative charge, with the exocyclic amino groups. In this way, the structure results in a cation channel surrounded by a lateral belt of picrates.

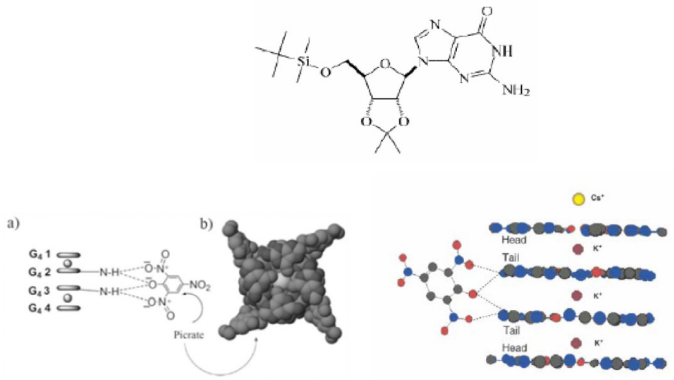

Figure 3. G quadruplex obtained by self-assembly of monomers of 5'-tert-butyldimethylsilyl-2',3'-isopropylidenguanosine.

Subsequently, Rivera's study [4] showed how a substituent inserted at the C8 position of lipoGs contributes positively to the stability of the complex. A substituent containing a hydrogen bond acceptor was chosen, such as the carbonyl group, so that the N2 of the exocyclic amino group of guanine, which does not normally participate in the set of intermolecular bonds that hold the quartet together, was involved. NMR studies at different concentrations and experiments performed by varying temperature led to interesting hypotheses: the substituent at the C8 position drives guanosine to adopt only the *anti* conformation, thus preventing ribbon formation. In addition, individual quartets are stabilized by the presence of four additional hydrogen bonds, while the aromatic ring of the substituent represents an additional π-π surface exploited in stacking between quartets (**Figure 4**).

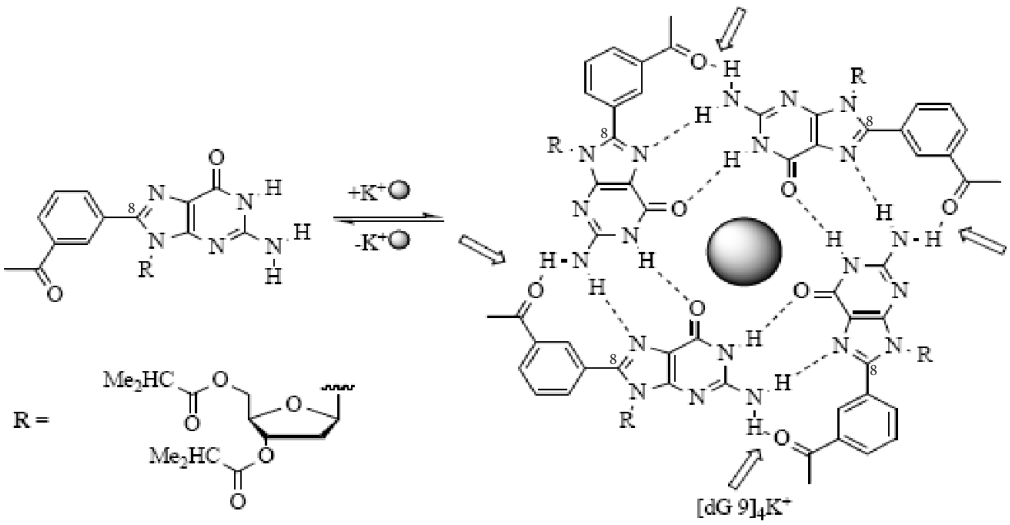

Figure 4. Structure of a single quartet coordinated to a cation.

Regarding quadruplexes in aqueous solution, guanosines bearing sugars in *syn* or *anti* position can be found within a single quartet according to a variety of combinations. In the case of lipoGs, on the other hand, within a single quartet there is conformational homogeneity, only all-*syn* or all-*anti* G-quartets are found [5]. In both the first and the second case, the quartet has two diasterotopic faces defined head and tail: the head is the face of the G quartet in which it is possible to run along hydrogen bonds by moving from NH to CO moving clockwise as shown in **Figure 5**.

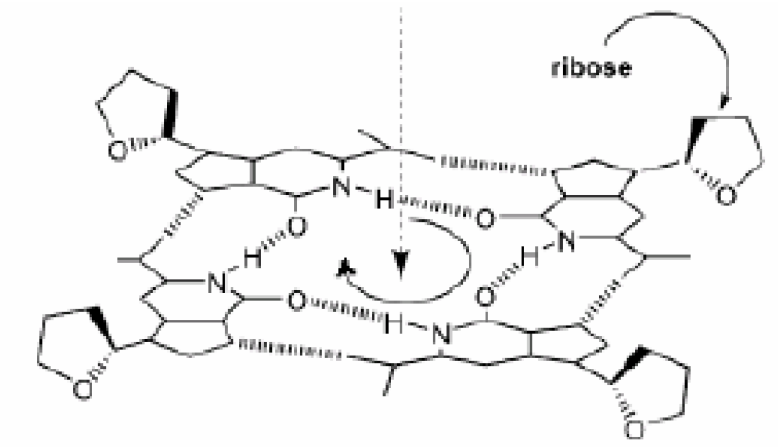

Figure 5. Head face of the quartet.

Although these are supramolecular structures, assembled through noncovalent bonds, the chirality of the sugar is transmitted to the whole system; for both octamers and pseudopolymeric structures, the arrangement of quartets is not randomized [5]. In the structure in **Figure 6**, the hexadecamer consists of the stacking of two head-to-tail octamers, coordinated by the K^+. Furthermore, the tetramers are not perfectly stacked on top of each other, but rather are rotated around an axis perpendicular to them, making the chiral assembly independent of the presence of the sugar unit R (**Figure 6**).

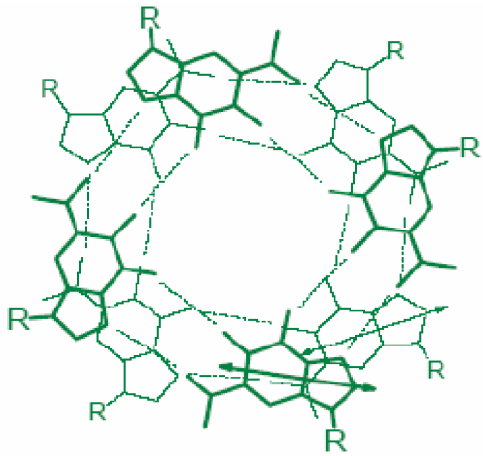

Figure 6. Stacking of tetramers.

Self-assembly in the absence of cation

So far the focus has been on the ability of guanosines, and their lipophilic derivatives, to self-assemble into quartets and pseudopolymers, emphasizing the importance of the cation for the formation of complexes. Such molecules are extremely versatile chemically and are able to generate, in the absence of cation coordination, alternative structures to G-quadruplexes defined ribbons, in which lipoGs are linked by hydrogen bonds but organized differently. The discovery of these ribbons was made by observing under an optical microscope the formation of a lyotropic mesophase obtained by evaporation of the hydrocarbon solvent in which the decanoic diester of deoxyguanosine was dissolved [6]: such liquid crystalline phase could not be due to quartet formation given the absence of cations in solution.

Subsequent ^{1}H-NMR and NOESY spectroscopy studies [7] allowed the structures obtained to be characterized in two types of ribbons named ribbon A and ribbon B (**Figure 7**), which boast different electronic and stability characteristics. The A-ribbon is the most thermodynamically stable structure in solution, while solid samples obtained by slow evaporation of the chloroform solution show the presence of B-ribbon structures. The transition is reversible by solvent removal.

The main difference between the two structures is related to their electron properties. Guanosine has a permanent electric dipole oriented along a straight line bisecting the C5-C6 and C2-N3 bonds: whereas in the B-ribbon the lipoGs are arranged so that the dipolar moments cancel, in the A-ribbon the components of the electric vectors along the axis of elongation add up so that the whole structure is polar (not centrosymmetric). This property has been exploited for the application of A-ribbon in nanotechnology devices.

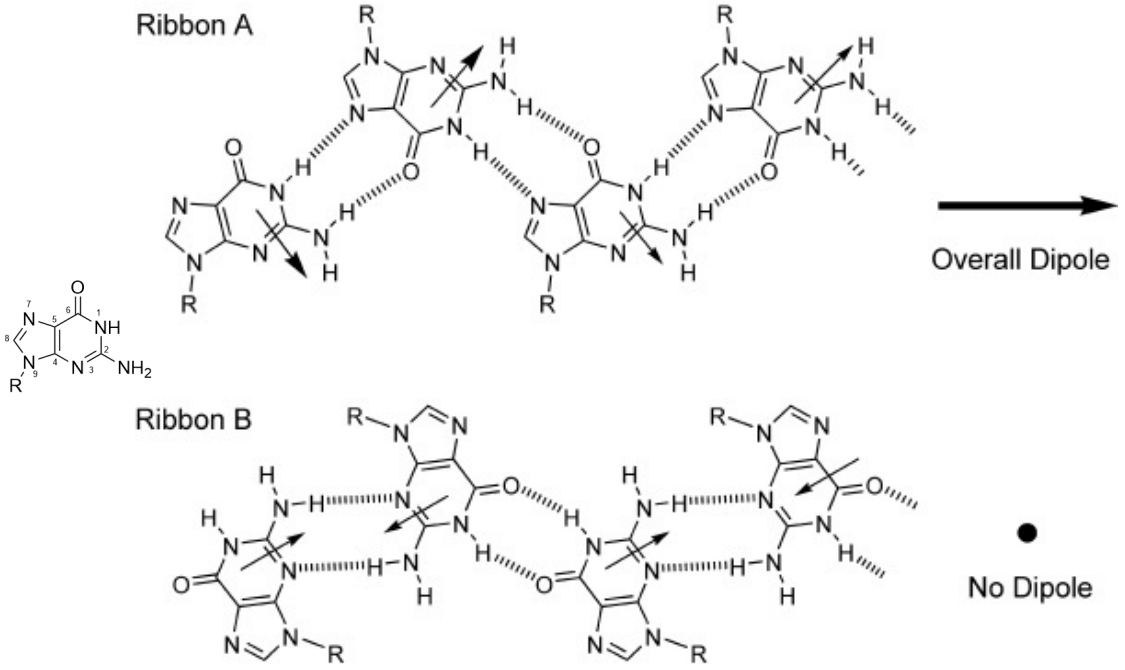

Figure 7. Different electronic characteristics of ribbons A-B: while in ribbon B the dipolar moments cancel out in ribbons A a polar supramolecular structure is generated.

Ribbons can also form two-dimensional gels, as observed by Araki's research group who studied the assembly of alkylsilylated derivatives of deoxyguanosine [8]. The observed supramolecular structure results from the organization of A-ribbons into leaflets placed antiparallel to each other and linked together by hydrogen bonds between the exocyclic amino group and N3 belonging to two adjacent guanosine residues (**Figure 8**).

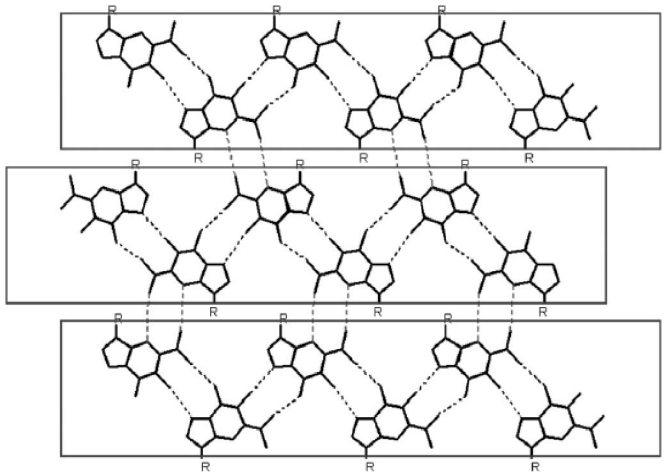

Figure 8. Supromolecular organization of A-ribbons in the formation of two-dimensional gels.

Ribbon structures are most commonly found in lipoGs in the absence of cations, but it is possible to obtain solutions or solid phases consisting of "empty" G quartets, devoid of the cation that usually determines the formation of such a structure. As demonstrated in Sessler's study [9], ribbon formation is sacrificed if bulky substituents are inserted at the C8 position to deoxyguanosine: in this specific case, derivatization with N,N-dimethylaniline groups prevents the molecules from assuming the *anti* conformation because of steric hindrance, forcing them to the *syn* conformation. In such a conformation, the favoured supramolecular structure is the G quartet, albeit without a cation (**Figure 9**).

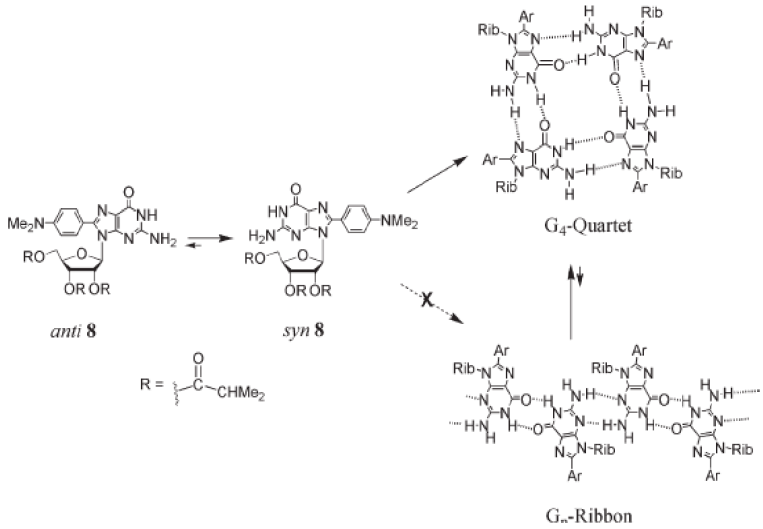

Figure 9. G-quadruplex formation in the absence of cation driven by LipoGs substituted at C8 position.

Application of ribbons in nanotechnology

The self-assembly of lipophilic guanosines into ribbons equipped with polarity has been and is still being exploited for the construction of nanotechnology devices. The first device was proposed by R. Rinaldi and R. Cingolani of the University of Lecce [10-12]: it is a hybrid electronic system consisting of a Silicon substrate in which two Au/Cr electrodes are deposited. Between electrodes is placed a drop of lipophilic guanosine solution then the solvent is removed under vacuum (**Figure 10**).

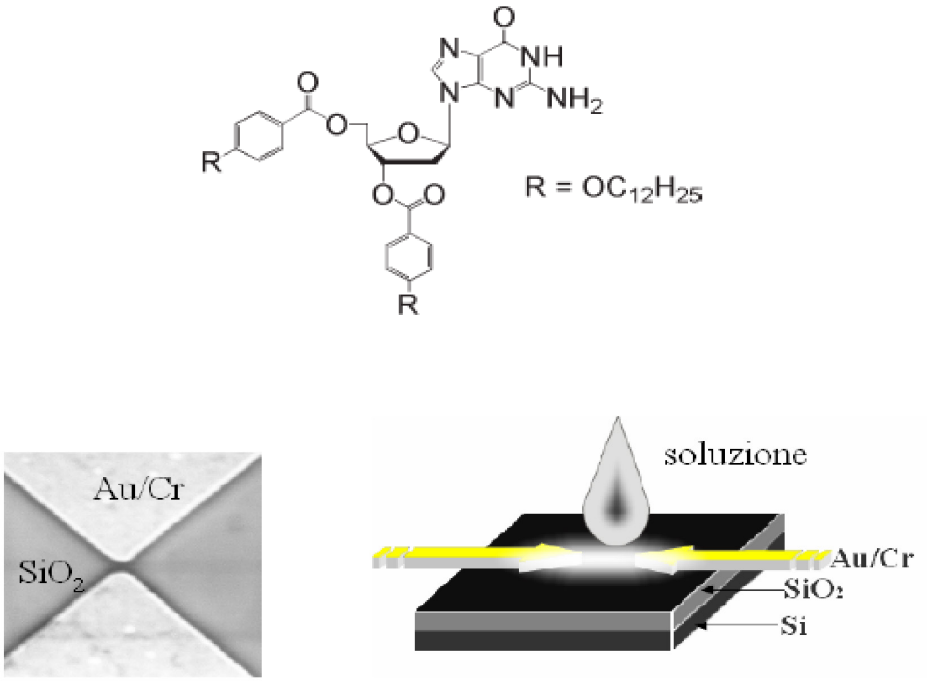

Figure 10. First application of LipoGs ribbons in nanotechnology.

The intensity of the electric current as a function of the applied potential was measured, and depending on the distance between the electrodes, a different response was observed.

At a distance of 800 nm between the electrodes the device behaves as a capacitor, at a distance of 120 nm a response similar to that of a semiconducting metal is obtained, while at distances of less than 60 nm, which allow the deposition of a single crystal, the nanoribbon exhibits the property of a diode to rectify electric current (**Figure 11**).

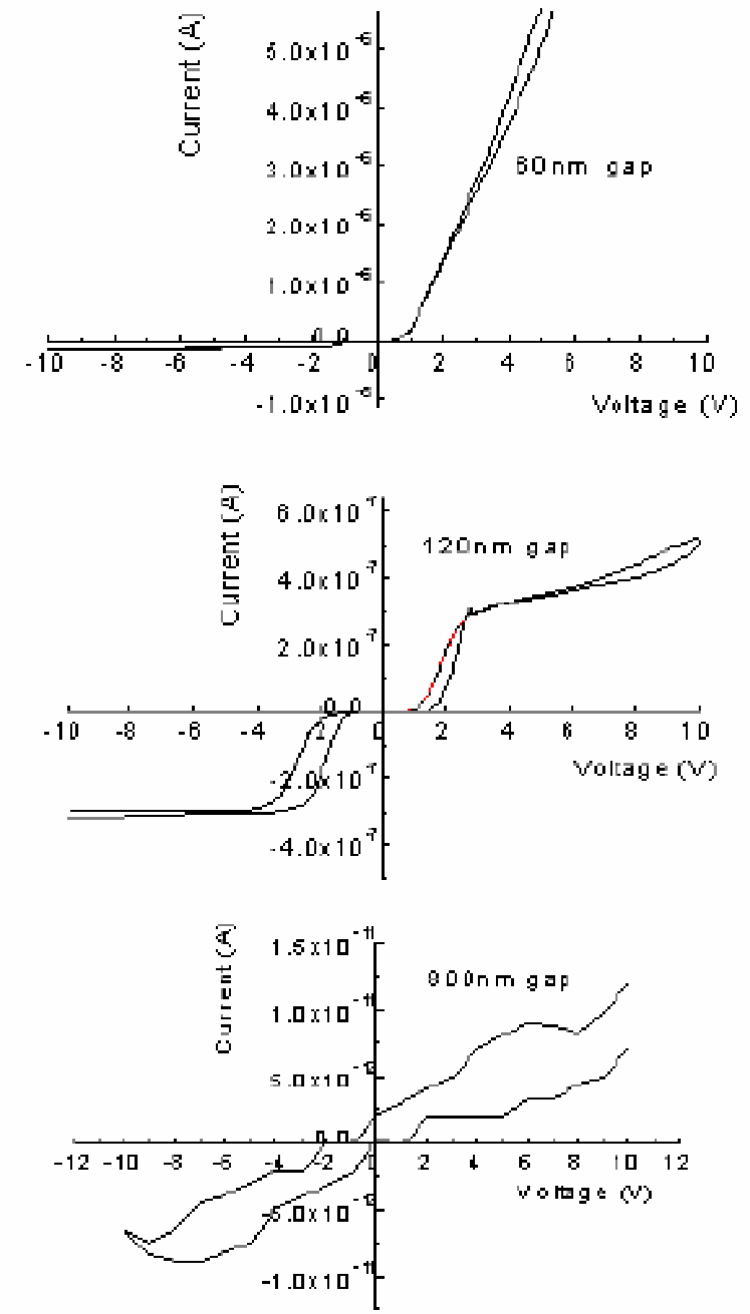

Figure 11. Different behaviors of the device depending on the distance between the electrodes.

Switching between supramolecular assemblies of Lipo-Gs

Controlling molecular assembly into well-defined nanoscale structures is a key step in improving the performance of materials [13,14] to be used, for example, as components of electronic nanodevices, such as solar cells, light-emitting diodes (LEDs) and field-effect transistors (FETs). This control has tremendous potential for materials science by bridging the gap between the molecular and macroscopic scales in terms of structural order when precise control of these self-assembly processes is achieved. Among weak interactions, π-stacking was the first to be employed to guide the self-assembly of conjugated (macro)-molecular systems into well-defined nanoscale assemblies that exhibit a high degree of order at the supramolecular level [15,16]. Further control of nanoarchitectures might be possible by incorporating more specific noncovalent interaction sites in the building blocks [14,17]. Among the various noncovalent interactions, multiple hydrogen bonds have been extensively adopted because of their directionality and selectivity [18]. Many examples of bottom-up nanostructuring of π-conjugated oligomers assisted by multiple hydrogen bonding interactions have been reported [17].

Guanine moiety is a versatile hydrogen bonding building block. In particular, lipophilic guanosines can undergo different self-assembly pathways originating diverse nanoarchitectures, and two typical assemblies are the ribbons and the cyclic G-quartet system previously described. The balance between different nanoarchitectures can be controlled, and as a result, certain physical properties can be tuned, possibly relevant to molecular electronics, organic photovoltaics, photonics and spintronics.

Three types of stimuli will be considered:

- variation of solvent polarity
- light (UV-vis)
- chemical stimulus (namely, addition or removal of cations)

Variation of solvent polarity

Under favorable conditions, a change in solvent properties can also control the type of supramolecular organization of LipoGs [19].

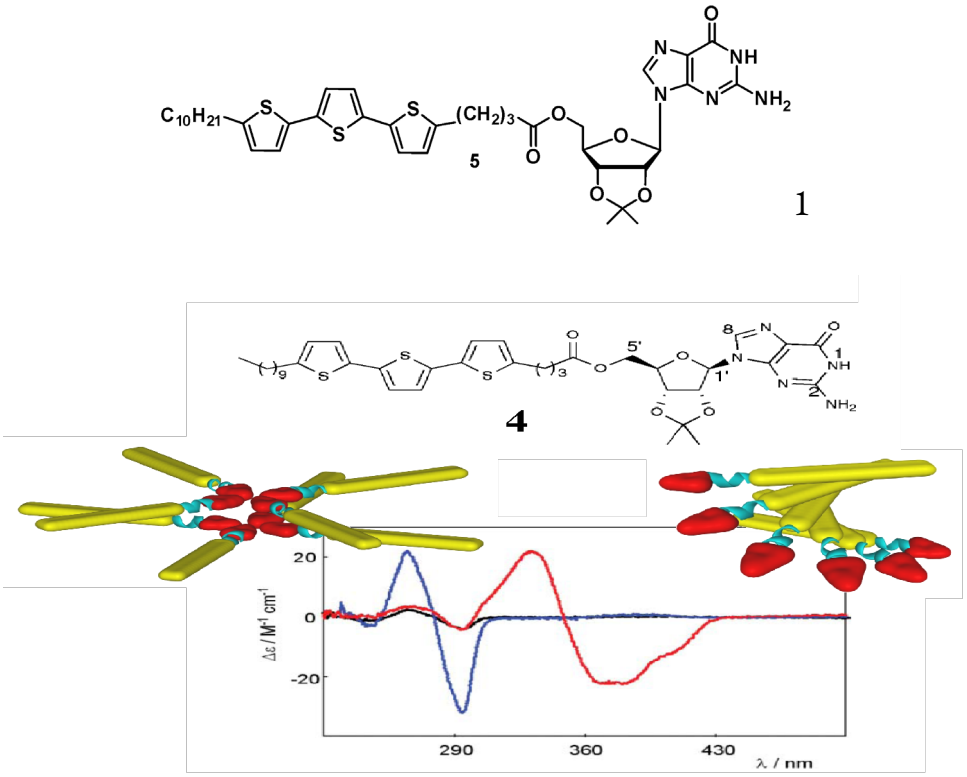

Figure 12. CD spectra of 1 in $CHCl_3$ (blue line) and in $CH_3CN/CHCl_3$ 9/1 (red line). The idealised models represent the supramolecular structures in the two solvent conditions (in red the guanine, in light blue the sugar and in yellow the terthienyl moiety)

An interesting case is LipoG **1** described in **Figure 12**, which has a tertiophene unit that can form a ribbon pattern or a columnar structure based on the G-quartet in THF in the absence or presence of alkali metal ions, respectively [20], thus allowing the control of the inter-oligothiophene interactions. Interestingly, LipoG **1** undergoes a pronounced variation of its supramolecular organization by changing the polarity of the solvent. In chloroform the guanosine derivative, templated by alkali metal ions, assembles via H-bonding in G-quartet based D_4-symmetric octamers; the polar guanine bases are located into the inner part of the assembly and act as a scaffold for the terthienyl pendants. On the other hand, in the more polar (and H-bond competing) acetonitrile (CH_3CN), different aggregates are observed, in which the terthiophene chains are stacked in a helical (left-handed) arrangement in the central core and the guanine bases, without hydrogen bonding, are located at the periphery and exposed to the solvent. The system can switch from one state (guanine-directed) to the other (thiophene-directed) with the alternate addition of chloroform and acetonitrile. Solvent-induced switching can be easily followed by circular dichroism spectroscopy (**Figure 12**): the exciton-paired CD in the absorption region of the guanine chromophore observed in chloroform disappears after

addition of acetonitrile, indicating disassembly of the G-quartet-based octameric structure, while an intense quasi-conservative exciton splitting in the 300-450 nm spectral region becomes predominant in the CD spectrum. This latter strong optical activity can be attributed to the helical packing of the conjugated terthiophene moieties stabilized by -π-π interactions. NMR spectra and photophysical investigations confirm the structures of the guanine- and thiophene-directed assemblies in chloroform and acetonitrile, respectively.

UV-vis irradiation

The photocontrolled self-assembly behavior of LipoG was investigated [21] and is described in **Figure 13**.

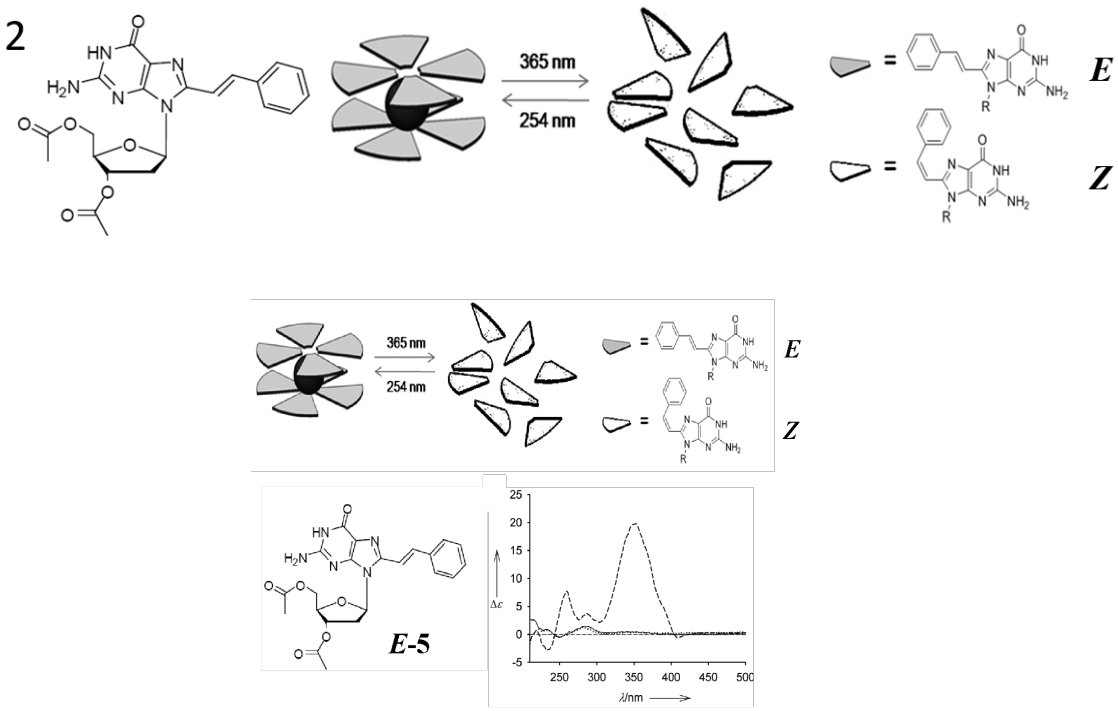

Figure 13. Top: cartoon of the photo-triggering of self-assembly of 2. Bottom: CD spectra of a solution of 2/KI (dashed line), of 2/KI at the *Z*-PSS (dotted line) and 2 at the *Z*-PSS (solid line) in acetonitrile.

When a weighted amount of KI is added to an acetonitrile solution of **2**, ^{1}H-NMR and CD spectra are indicative of the formation of stacked G-quartets templated by the cation. In particular, an octameric species $(2)_8K^+$, consisting of two stacked G-quartets arranged in a D_4 symmetry is formed. Although detailed information on electronic transitions is not available for the 8-stilguanine chromophore, the CD spectral changes observed with the addition of the potassium ion closely resemble those reported for other immodified lipophilic guanosines [1]. The strong increase in the CD signal associated with the formation of the aggregate **2**/K^+ can be similarly attributed to the interchromophore couplings that occur in the stacked complex (see **Figure 13**, dotted line in the CD spectra). When samples of the **2**/K^+ octameric complex are irradiated at 365 nm, photoconversion to the Z isomer takes place and the Z-PSS is reached.

The photoisomerization has a dramatic effect on the assembled species. The CD spectrum of the **2**/KI solution recorded at the Z-PSS shows very weak signals (**Figure 13**, dashed line in the CD spectra): this spectrum is practically superimposable on the CD spectrum of Z-2 before the addition of KI (**Figure 13**, solid line in the CD spectra) and is similar to that of unassembled **2**. The disappearance of the strong CD bands at 255 and 350 nm demonstrates the decomposition of the complex: the stacked G-quartets no longer exist in solution. The absence of G-quartets in the case of Z-2 is probably because in the Z form the phenyl group of the styryl unit is twisted with respect to the plane of the G-quartet. The resulting steric hindrance could force the quartets away from the van der Waals contact or could produce a conformational change around the glycosidic bond, which in turn would hinder stacking. Also, in the Z form, N7 is probably shielded by the styryl unit and is no longer available for H-bonds.

The Z form can be converted back to the E form either photochemically, by irradiating at 254 nm, or thermally. The return to the E isomer results, at the supramolecular level, in the re-formation of the octameric complex: the CD spectrum of the solution at this point overlaps perfectly with the starting $(2)_8K^+$ trace. Therefore, the complex based on the G quartet can be assembled and disassembled cyclically by light.

Addition/removal of cations

Considering that the supramolecular structures obtained in the presence or in the absence of cations are different, an obvious chemical stimulus is represented by the addition and removal of potassium ions to/from a solution of a LipoG.

The addition/removal of K^+ ions can be controlled by means of cryptand [a] [22]. In fact, this cryptand has a high affinity for K^+ and allows its removal from the system. However, the ability of [a] to capture the K ion is pH-dependent and in its protonated form this macrocycle is no longer active as cryptand. This fact can be exploited to switch reversibly from ribbons to G-quartets by successive addition of acid and base [23]. More in detail, the addition of potassium picrate to a chloroform solution of lipoG (**Figure 14**) transforms the supramolecular ribbon into the octameric complex based on the G-quartet motif. Upon subsequent addition to the quadruplex solution of the [a] cryptand, potassium is captured by the cryptand (hence the cryptate is formed) and the system reverts to the original G-ribbon. At this point upon addition of an acid (triflic acid), K^+ is released from the cryptate and the G-quartet based system is regenerated. Finally, adding afterwards a base (triethylamine) the protonated cryptand deprotonates, the free cryptand recaptures K^+ and the G-ribbon is formed again. The acid/base addition steps can be repeated several times.

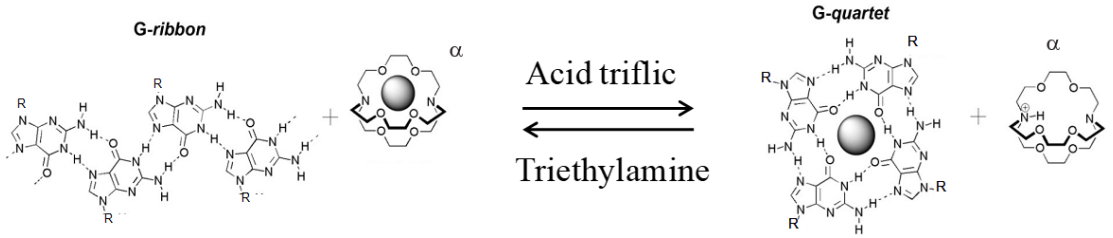

Figure 14. The acid/base controlled interconversion between G-ribbons and G-quartet base structures.

^{1}H-NMR and Circular Dichroism (CD) can be both exploited to monitor the ribbon-quadruplex interconversion. Without considering details, the ^{1}H-NMR spectra of the octamer and the ribbon are different: for example, the former shows a double set of signals (selected signals are marked by triangles in **Figure 15**) resulting from its C_4 symmetry, while the latter shows a single set (marked by a star in **Figure 15**).

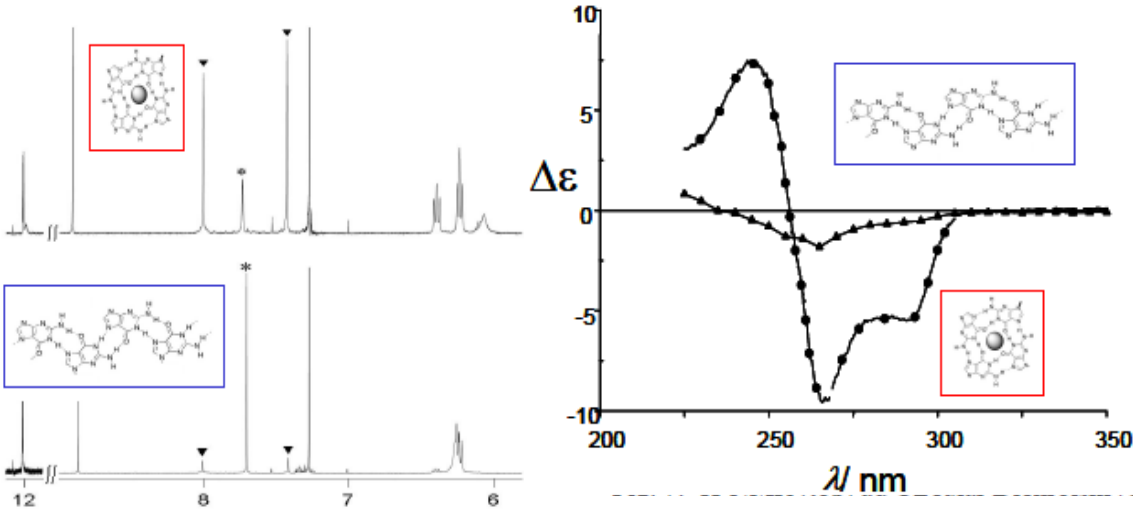

Figure 15 ^{1}H-NMR (left) and Circular Dichroism (right) spectral variation upon reversible quartet-to-ribbon transformation upon acid/base addition.

This same chemical-stimulus-controlled self-assembly has been exploited with guanosine derivatives armed with one or two persistent paramagnetic units, 4-carbonyl-2,2,6,6-tetramethylpiperidine-1-oxyl (TEMPO) [24]. As shown in the ESR spectra, in the absence of metal cations the spectrum of LipoG **3** (**Figure 16**, trace a) is characterized by three equidistant lines (with a broadening between them indicating that intramolecular spin exchange is occurring). In sharp contrast, the ESR spectrum recorded after solid-liquid extraction of potassium picrate shows mainly one very broad signal whose integrated intensity corresponds to the initial number of radicals (**Figure 16**, trace b). The signal broadening is independent of concentration and temperature, and thus inter-assembly interactions and motional broadening can be excluded.

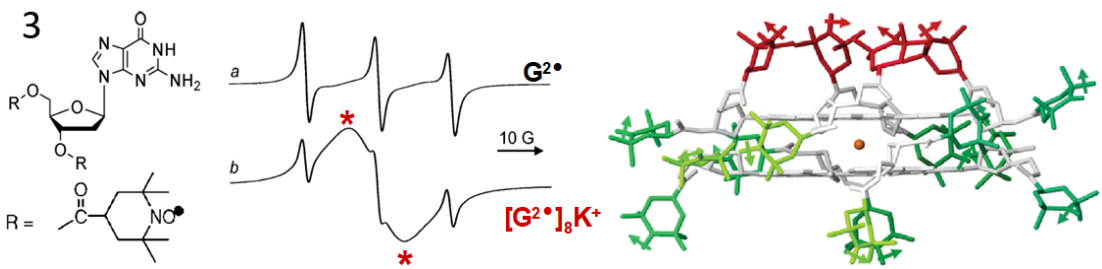

Figure 16. The EPR spectrum of LipoG 3 before and after K+-directed formation of an octameric G-quartet based species. Stars mark the signals due to intermolecular spin-spin exchange. In the right part: a molecular model of the assembled species.

Octameric assembly allows the confinement of 16 paramagnetic units in a small volume, resulting in a remarkable change in magnetic properties upon reversible formation. Since the relative geometry of the radical units is the result of K^+-directed self-assembly, the spin-spin interaction is suppressed by removing the alkaline ion by means of the cryptand/acid-base system described above.

Research aim and thesis outline

The combination of a variety of changes at the molecular level (different substituents in C8 position, functionalization of sugar hydroxyl groups with hydrophobic moieties) and chemical conditions of the environment, can drive guanosines to self-assemble into specific structures. In particular, in this thesis, the structures obtained from self-assembly of guanosines having different substituents at C8 and C5' positions (**Chapter 6**) and the structure obtained from aggregation of LipoG in the presence of the silver cation (**Chapter 7**) were studied.

References

[1] (a)Stefan, L., & Monchaud, D. (2019). Nat. Rev. Chem., 3, 650-668.(b) Davis, J. T., & Spada, G. P. (2007). Chem. Soc. Rev., 36, 296-313.(c) Lena, S., Masiero, S., Pieraccini, S., & Spada, G. P. (2009). Chem. Eur. J., 15, 7792-7806.

[2] Gottarelli, G., Masiero, S., & Spada, G. P. (1995). Self-assembly in organic solvents of a deoxyguanosine derivative induced by alkali metal picrates. Chem. Commun., 2555.

[3] Shi, X. D., Mullaugh, K. M., Fettinger, J. C., Jiang, Y., Hofstadler, S. A., & Davis, J. T. (2003). Cation Exchange in Lipophilic G-Quadruplexes: Not All Ion Binding Sites Are Equal. J. Am. Chem. Soc., 125, 10830.

[4] (a)Betancourt, J. E., Martin-Hidalgo, M., Gubala, V., & Rivera, J. M. (2009). J. Am. Chem. Soc., 131, 3186. (b) Gubala, V., Betancourt, J. E., & Rivera, J. M. (2004). Org. Lett., 6, 4735-4738.

[5] Marlow, A., Mezzina, E., Masiero, S., Spada, G. P., & Davis, J. T. (1999). Cation-Templated Self-Assembly of a Lipophilic Deoxyguanosine: Solution Structure of a K+-dG8 Octamer. J. Org. Chem., 64, 5116

[6] Gottarelli, G., Masiero, S., Mezzina, E., Pieraccini, S., & Spada, G. P. (1999). A new lyotropic liquid crystalline phase formed in hydrocarbon solvents by a deoxyguanosine derivative through extensive hydrogen bonding. Liq. Cryst., 26, 965.

[7] Gottarelli, G., Mariani, P., Masiero, S., Mezzina, E., Recanatini, M., & Spada, G. P. (1998). "The selfassembly of a lipophilic deoxyguanosine derivative and the formation of a liquid crystalline phase in hydrocarbon solvents. Helv. Chim. Acta, 81, 2078.

[8] (a) Araki, K., & Yoshikawa, I. (2005). Top. Curr. Chem., 256, 133.(b) Sato, T., Seko, M., Takasawa, R., Yoshikawa, I., & Araki, K. (2001). J. Mater. Chem., 11, 3018.

[9] Sessler, J. L., Sathiosatham, M., Doerr, K., Lynch, V., & Abboud, K. A. (2000). Dissecting Solvent Effects on Hydrogen Bonding. Angew. Chem. Int. Ed., 39, 1300-1302.

[10] Rinaldi, R., Maruccio, G., Biasco, A., Arima, V., Cingolani, R., Giorgi, T., Masiero, S., Spada, G. P., & Gottarelli, G. (2002). Hybrid molecular electronic devices based on modified deoxyguanosines. Nanotechnology, 13, 398.

[11] Maruccio, G., Visconti, P., Arima, V., D'Amico, S., Biasco, A., D'Amone, E., Cingolani, R., Rinaldi, R., Masiero, S., Giorgi, T., & Gottarelli, G. (2003). Characterization of self-assembled monolayers of porphyrins on gold. Nano Letters, 3(4), 479-483.

[12] Rinaldi, R., Branca, E., Cingolani, R., Masiero, S., Spada, G. P., & Gottarelli, G. (2001). Electrical properties of self-assembled monolayers of aminoporphyrins. Applied Physics Letters, 78(23), 3541-3543.

[13] Grimsdale, A. C., & Müllen, K. (2005). The chemistry of organic nanomaterials. Angewandte Chemie International Edition, 44(36), 5592-5629.

[14] Palermo, V., & Samorì, P. (2007). Supramolecular materials: Self-organization of molecular nanosystems. Angewandte Chemie International Edition, 46(23), 4428-4438.

[15] Samorì, P., Francke, V., Müllen, K., & Rabe, J. P. (1999). Toward functional nanostructures: Self-assembly of supramolecularly engineered architectures using molecular recognition and chemical communication. Chemistry – A European Journal, 5(8), 2312-2321.

[16] Schenning, A. P. H. J., Kilbinger, A. F. M., Biscarini, F., Cavallini, M., Cooper, H. J., Derrick, P. J., Feast, W. J., Lazzaroni, R., Leclère, L., McDonell, L. A., Meijer, E. W., & Meskers, J. S. C. (2002). From functional supramolecular systems to nanotechnology: Application of self-assembly in chemistry and materials science. Journal of the American Chemical Society, 124(6), 1269-1282.

[17] Schenning, A. P. H. J., & Meijer, E. W. (2005). Supramolecular polymer chemistry. Chemical

Communications, (26), 3245-3258.

[18] Lehn, J.-M. (1995). Supramolecular chemistry: Concepts and perspectives. VCH Publishers.

[19] Pieraccini, S., Bonacchi, S., Lena, S., Masiero, S., Montalti, M., Zaccheroni, N., & Spada, G. P. (2010). Solvent-induced switching between two supramolecular assemblies of a guanosine–terthiophene conjugate. Org. Biomol. Chem., 8, 774.

[20] Spada, G. P., Lena, S., Masiero, S., Pieraccini, S., Surin, M., & Samorì, P. (2008). Guanosine-based Hydrogen-bonded Scaffolds: Controlling the Assembly of Oligothiophenes. Adv. Mater., 20, 2433.

[21] Lena, S., Neviani, P., Masiero, S., Pieraccini, S., & Spada, G. P. (2010). Triggering of Guanosine Self-Assembly by Light. Angew. Chem. Int. Ed., 49, 3657.

[22] Lehn, J. M., & Sauvage, J. P. (1975). Cryptates. XVI. [2]-Cryptates. Stability and selectivity of alkali and alkaline-earth macrobicyclic complexes. J. Am. Chem. Soc., 97, 6700.

[23] Ciesielski, A., Lena, S., Masiero, S., Spada, G. P., & Samorì, P. (2010). Dynamers at solid-liquid interface: controlling the reversible assembly-reassembly process between two highly ordered supramolecular gunaine motifs. Angew. Chem. Int. Ed., 49, 1963-1966.

[24] (a) Neviani, P., Mileo, E., Masiero, S., Pieraccini, S., Lucarini, M., & Spada, G. P. (2009). Org. Lett., 11, 3004-3007. (b) Graziano, C., Pieraccini, S., Masiero, S., Lucarini, M., & Spada, G. P. (2008). Org. Lett., 10, 1739-1742.

CHAPTER 6

Self-Assembly of Functionalized Lipophilic Guanosines into Cation-Free Stacked Guanine-Quartets

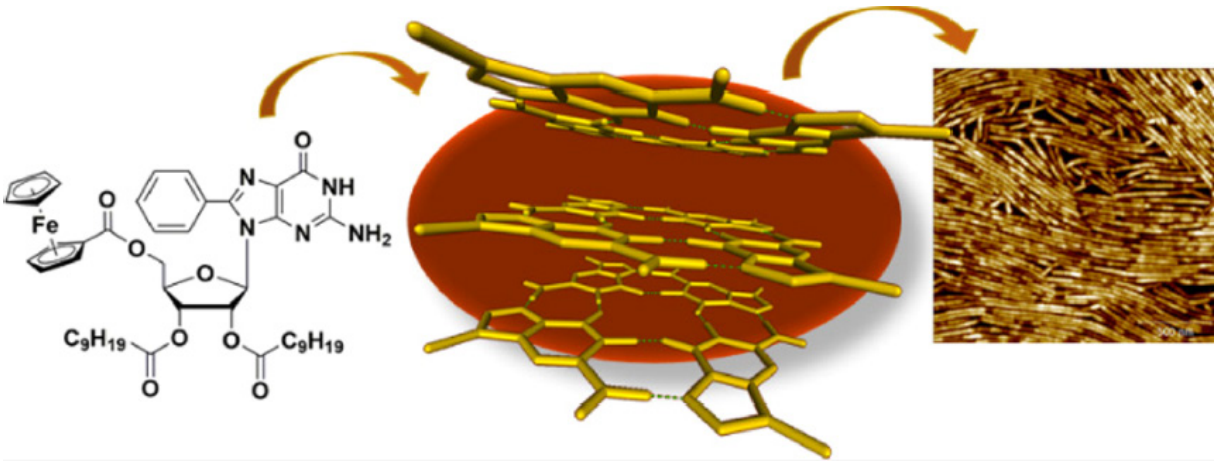

This chapter is reproduced from: Marilena Campitiello, Alessio Cremonini, Marco A. Squillaci, Silvia Pieraccini, Artur Ciesielski, Paolo Samorì, and Stefano Masiero. The Journal of Organic Chemistry 2021 86 (15), 9970-9978

Introduction

Among DNA bases, Guanosine (G) exhibits a unique ability to undergo self-assembly, forming various distinct supramolecular structures [1,2] In particular, lipophilic guanosine derivatives have been reported to generate either supramolecular ribbon-like architectures [3–6] or tetrameric array (G-quartets)-based assemblies [7,8]. The formation of a specific assembly motif is ruled by both the specific chemical structure of the derivative [9,10] and the environmental conditions [10,11]. Among various G assemblies, G-quartet (hereafter G4)-based supra-molecular architectures are by far the most important because of the biological relevance of this structural motif in DNA [12,13]. Many G4-based lipophilic complexes can be found in the literature, ranging from octamers (two stacked G4s) and hexadecamers [14–16], these being the most frequent and studied examples, up to pseudo-polymeric stacked assemblies [17]. All these aggregates form spontaneously only in the presence of a metal cation, with the latter playing a crucial role in templating and stabilizing these architectures. For this reason, simple, isolated G4s are probably the least-described supramolecular structures that originate from guanosine because, in the absence of templating cations, the common self-assembled motif of lipophilic guanosines has a ribbon-like architecture. Isolated G4s as the main species, either in the absence [18–21] or in the presence [22,23] of a metal cation, have been indeed seldom reported. Isolated G4s lacking a templating ion are observed when a bulky substituent is placed at the C8 position of the nucleobase or, more generally, in cases where the formation of *G*-ribbons is hindered by the molecular structure. The ability of isolated G4s, in the absence of a templating cation, to form higher-order organized assemblies has never been reported. Here, we have focused our attention on both 8-ferrocenyl and 8-phenyl functionalized lipophilic guanosines carrying groups with different bulkiness at the 5′ position (**Scheme 1**), and we show that subtle modifications in the molecular structure cause a dramatic change in the propensity of the molecules to undergo a hierarchical self-assembly. In particular lipophilic guanosine derivative **1** (**8Ph5Fc**) was found to form isolated G4s, which further self-assemble into stacked cation- free architectures. Conversely, derivatives **2–8**, and derivative **8** (**8Fc5Ph**) especially, where phenyl and ferrocenyl substituents are swapped with respect to **1**, exhibit no clear tendency to form supramolecular assemblies arising from piling up of G4s.

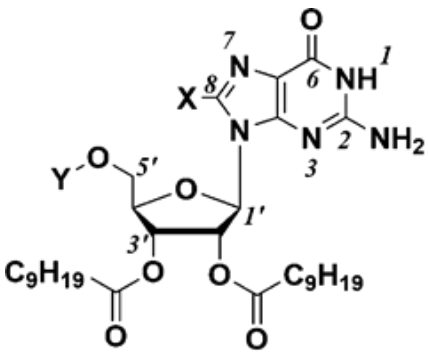

1 (8Ph5Fc) X = Ph, Y = CO-Fc
2 (8Ph5OH) X = Ph, Y = H
3 (8Ph5Si) X = Ph, Y = TBDMS
4 (8Ph5C10) X = Ph, Y = CO-C_9H_{19}
5 (8Fc5C10) X = Fc, Y = CO-C_9H_{19}
6 (8Fc5Si) X = Fc, Y = TBDMS
7 (8Fc5OH) X = Fc, Y = H
8 (8Fc5Ph) X = Fc, Y = CO-Ph

Scheme 1. Chemical Structures of the Investigated Guanosine Derivatives.

Results and discussion

All investigated G derivatives were synthesized, starting from commercial guanosine, as described in synthetic schemes.

The circular dichroism (CD) spectrum of all compounds in CH_2Cl_2 shows only a weak molecular induced circular dichroism (ICD) band, attributed to the chiral perturbation of the guanine chromophore by the chiral sugar residue, and does not change upon the addition of either MeOH or cryptand: this rules out the presence of templating ions residual from synthetic procedures. In contrast, deliberate addition of KI produces a strong excitonic spectrum, characteristic of G4 stacking [24].

A typical feature of the ^{1}H-NMR spectra of G4 structures is the splitting of the signal for exocyclic amino protons into two signals as hydrogen bonding produces a large downfield shift of the proton involved in G4 formation [16]. Usually, this signal splitting is not observed at room temperature because the two protons are in fast exchange regime, but it can be easily monitored by lowering the temperature. Signals that can be ascribed to amino groups start to appear at −5 to −20 °C both in the 9−10 ppm and in the 5−5.5 ppm ranges, and they become progressively sharper upon further lowering the temperature. In the case of **8Ph5Fc**, the amino proton signal is baseline-broadened in the CD_2Cl_2 room temperature spectrum. At −5 °C, two signals start to appear at 9.8 and 5.5 ppm for bound-N(2)H and free-N(2)H, respectively, and they shift slightly downfield and upfield, respectively, by further lowering the temperature. Moreover, the N(1)H imino proton signal resonates at 12.6 ppm at room temperature and undergoes deshielding upon lowering the temperature. The same signal resonates at 10.9 ppm in DMSO-d6, suggesting that in CD_2Cl_2, G is H-bonded already at room temperature. All the other investigated compounds show the same behavior, yet they differ in two aspects. First, the two amino signals start to appear only at lower temperatures (compare −20 °C, NMR spectra). Second, imino and amino signals of the second assembled species (NMR spectra) become visible in most cases (with the exception of the two 5'OH derivatives **8Ph5OH** and 8Fc5OH, see below) in the downfield portion of the spectrum. No clear evidence could be obtained on the architecture of these minor species. Nonetheless, this suggests a higher stability for the aggregate formed by **8Ph5Fc**, while for derivatives 2−8, other, although minor, self-assembly pathways are viable. Further evidence of the existence of self-assembled species in solution is given by nuclear Overhauser effect (NOE) spectra (**Figure 1**). As the first general observation, in all cases, NOE spectra display cross-peaks having the same phase as the diagonal. This feature is characteristic of a slow tumbling regime, implying that the objects in the solution have a molecular weight above ca. 2000 Da [25] whereas the molecular weight of an isolated molecule of 1−8 falls in the range of 667−929 Da. Another common feature of the main species formed by all of the investigated compounds is their preference for the syn conformation around the glycosidic bond. **Figure 1b**,c shows selected one-dimensional NOE spectroscopy (1D- NOESY) spectra of 1 recorded at −20 °C as an example. The interaction between "o" and H1' protons, already strong at room temperature (not shown), and the absence of any correlation between H5'/H5" and phenyl protons points to an exclusive syn conformation for 1, as depicted in the inset of Figure 1a.In the case of derivatives **8Ph5OH** and **8Fc5OH**, lacking a bulky substituent at the 5′ position, the syn conformer is possibly stabilized by an intramolecular H-bond between 5'OH and N(3) (see spectrum **Figure 2a,b,c,d**).

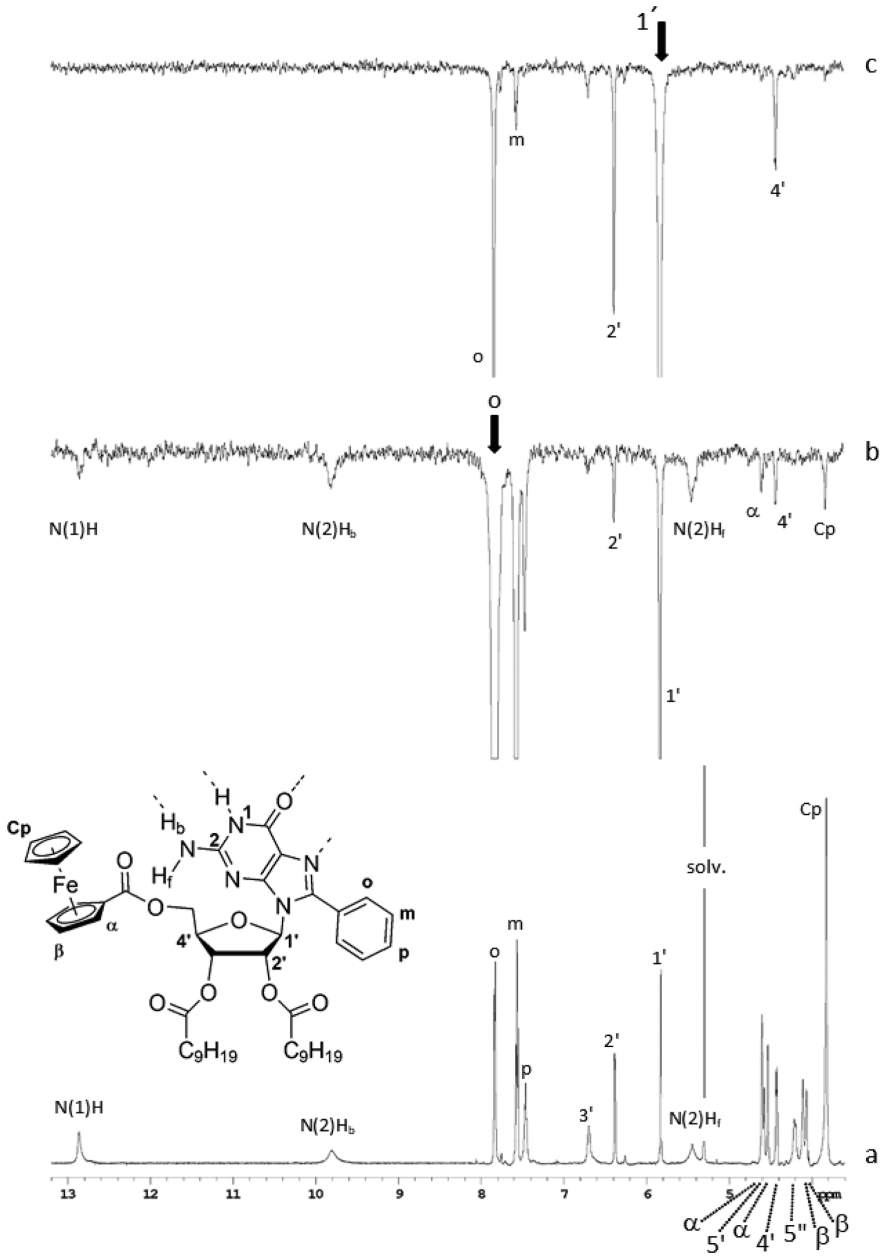

Figure 1. (a) Downfield portion of the 600 MHz ^{1}H-NMR spectrum of **8Ph5Fc** in CD_2Cl_2 (4.3 mM) at −20 °C and signal assignment (diastereotopic protons were not assigned); (b) NOESY-1D spectrum of the same sample upon irradiation at 7.83 ppm ("o" protons); (c) NOESY-1D spectrum of the same sample upon irradiation at 5.82 ppm (1′ proton). In each NOE spectrum were used 512 coadded transients, a recycle delay of 0.6 s, a mixing time of 0.6 s, and a 50 Hz shaped pulse. Irradiated frequencies are indicated with an arrow.

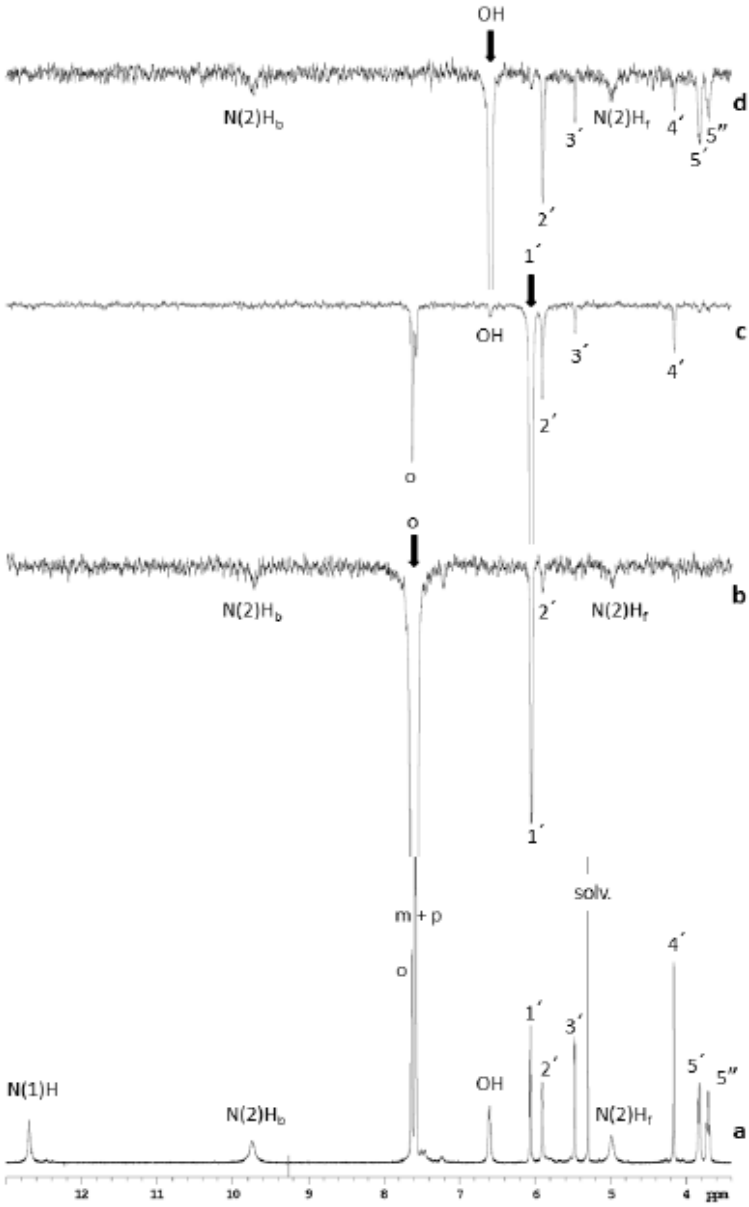

Figure 2. a) Downfield portion of the 600 MHz ^{1}H-NMR spectrum of **8Ph5OH** in CD_2Cl_2 (5 mM) and signals assignment (diastereotopic protons were not assigned); b), c), d): selected NOESY-1D spectra of the same sample. Irradiated signals are indicated by an arrow. In each NOE spectrum were used at least 1024 coadded transients, a recycle delay of 1 sec, a mixing time of 0.25 sec and a 20-50Hz shaped pulse. All spectra were recorded at -40°C.

It is known [26] that a downfield shift of the ribose H2' proton parallels an increase in the percentage of syn conformer population. In particular, 8-bromoguanosine (δH2' = 5.01 ppm in DMSO-d6) is ca. 90% syn, while guanosine (δH2' = 4.429 ppm) is only 40% syn. Although a direct comparison with these figures is not possible, an analysis of the observed chemical shifts for derivatives 1–8 (see table 1) allows some qualitative conclusions. The introduction of ferrocenyl substituent at the 8-position exhibits a marked effect on the chemical shift of both H1' and H2' sugar protons, which move downfield by about 1 ppm. On the other hand, the 8-phenyl substituent exhibits a smaller effect and is limited to the H2' and H3' protons. Taking this result into account, it is possible to notice that the H2' proton tends to resonate at lower fields than H1' for the 8-phenyl derivatives, while 8-ferrocenyl derivatives show the same chemical shift order (δH1' > δH2' > δH3') as the reference compounds (entries h–n in Table 1). This suggests that the phenyl ring has a higher ability to drive the conformational equilibrium toward the syn isomer than the ferrocenyl substituent. In particular, the unique sequence δH3' > δH2' > δH1' shown by **8Ph5Fc** in CD_2Cl_2 should be noticed.

	Compound	solvent	δ(1')	δ(2')	δ(3')	δ sequence
a	**8Ph5Fc**	dmso	5.808	6.31	5.83	2'>3'>1'
		dcm	5.86	6.43	6.48	3'>2'>1'
b	**8Ph5OH**	dmso	5.78	5.496	5.186	1'>2'>3'
		dcm	6.2	6.04	5.588	1'>2'>3'
c	**8Ph5Si**	dmso	5.75	6.36	6.17	2'>3'>1'
		dcm	5.75	6.26	5.63	2'>1'>3'
d	**8Ph5C10**	dmso	-	-	-	-
		dcm	5.86	6.29	6.16	2'>3'>1'
i	**8Fc5C10**	dmso	6.75	6.58	5.74	1'>2'>3'
		dcm	6.95	6.59	6.12	1'>2'>3'
e	**8Fc5Si**	dmso	6.747	6.69	5.71	1'>2'>3'
		dcm	6.82	6.74	6.18	1'>2'>3'
f	**8Fc5OH**	dmso	6.86	5.61	5.3	1'>2'>3'
		dcm	7.22	6.12	5.71	1'>2'>3'
g	**8Fc5Ph**	dmso	6.77	6.63	5.99	1'>2'>3'
		dcm	6.9	6.63	6.51	1'>2'>3'
h	8-Bromo-2,3,5-tri-O-decanoylguanosine [1]	dmso	5.84	6.02	5.68	2'>1'>3'
i	2,3,5-tri-O-decanoylguanosine [2]	dmso	5.96	5.81	5.52	1'>2'>3'
l	2,3,5-tri-O-acetylguanosine	dmso [3]	6.007	5.809	5.515	1'>2'>3'
m	8-Bromoguanosine 9	dmso [4]		4.89		
		dmso	5.68	5.01	4.14	1'>2'>3'
n	Guanosine	dmso [4]		4.36		
		dmso [3]	5.723	4.429	4.113	1'>2'>3'

Table 1 Room atemp. chemical shifts* for sugar protons.

NOE spectra also provide unambiguous information on the structure of the main self-assembled species in solution. Another feature common to the main species formed by **1–8** is the dipolar coupling between the protons of the substituent at the C(8) position and the exocyclic amino group. For example, the case of **8Ph5Fc**, the o protons interact with both exocyclic amino and ferrocene protons (**Figure 1b**). These proximities can only occur at the intermolecular level and rule out G-ribbon assemblies but point to a G4 structure (such as the one presented in **Figure 2** in the case of **8Ph5Fc**) as the main self-assembled aggregate formed by all the derivatives.

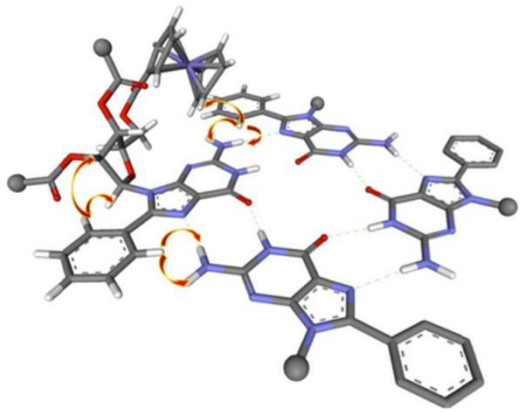

Figure 2. Proposed model for the isolated G_4 formed by 8Ph5Fc. Arrows indicate selected NOEs. Some atoms are omitted for clarity.

Stabilization of this structure by residual water [27] seems unlikely because in no case did we observe in NOE spectra a signal in the 1.5–2.5 ppm region, except for the expected exchange signals with N(1)H and N(2)H. To gain deeper insights into the propensity of the derivatives to undergo self-assembly, we have extended our study to atomic force microscopy (AFM) imaging. In addition to **8Ph5Fc**, derivatives **8Fc5C10** and **8Ph5C10** were studied for comparison. The samples were prepared by drop-casting 150 μL of guanosine solutions in CH_2Cl_2 (concentration 0.6 mg/ mL) onto the basal plane of thermally grown SiO2/Si (230 nm SiO_2 on Si [100]). Prior use, the substrates were cleaned and functionalized with a monolayer of hexamethyldisilazane (HMDS), covalently bonded to the pending SiOH groups, in order to render the surface hydrophobic and to avoid the formation of hydrogen bonds between the molecules and the substrate. **Figure 3** displays the topographical AFM images of films of **8Ph5Fc** (**Figure 3 a,c**) and **8Fc5C10** (**Figure 3 b,d**) prepared using the same experimental conditions.

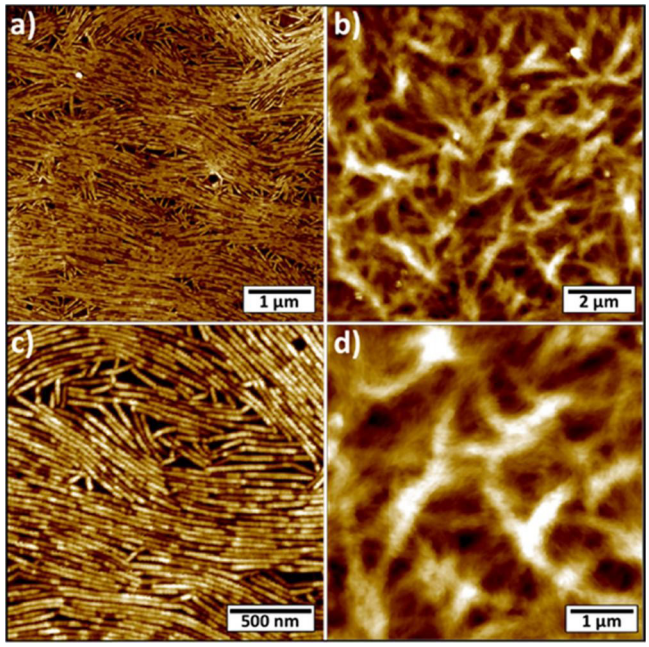

Figure 3. AFM images of supramolecular metal-free G aggregates drop-cast from CH_2Cl_2 0.6 mg/mL on HMDS-functionalized SiO_2. (a,c) Molecule **8Ph5Fc**. (b,d) Molecule **8Fc5C10**. Images Z-scales: (a) 10 nm; (b) 140 nm; (c) 7 nm; and (d) 110 nm.

The observed morphologies are markedly different. Molecule **8Fc5C10** forms a disordered network of entangled bundles of fibers, while **8Ph5Fc** self-assembles into layers of ordered and well-aligned fibers possessing an average height of 4.1 ± 0.5 nm (measured with respect to the widest empty areas) and an average width of 32 ± 4 nm. Being the lateral size of the fibers comparable to the curvature radius of the used AFM tips (nominal radius 7 nm), the measured width value must be corrected to exclude the broadening artifact given by the mechanical convolution effect. Considering the measured width and an inter fiber penetration of the tip of about 1.8 nm, we can apply well-established models [28] to conclude that the real width of such fibers amounts to 19 ± 4 nm. As the radius of the G-quartet structure in columnar aggregates, both in water [29] and in organic solvents [17] amounts to 12.5 Å and a fully elongated decanoyl residue measures ca.12 Å, it is possible to estimate a diameter of 4.8 nm for the G4s formed by **8Ph5Fc**. This value is in good agreement with the average measured height for the fibers. Assuming a 3.3 Å spacing (characteristic of optimal nucleobase stacking [30]), the cylindrical fibers shown in **Figure 3a,c** are composed on an average of six stacked G4s. To promote the aggregation into more stable and ordered supramolecular structures, the films were then exposed to solvent vapor annealing (SVA) in CH_2Cl_2 for 48 h under ambient conditions. Such a method makes it possible to trigger the molecular reorganization toward the generation of thermodynamically favored architectures. It is noteworthy that this method has previously been successfully used to finely tune the self-assembly of various molecular systems, including n-type perylene nanowires [31] p-type pentacene [32] hexa-peri- hexabenzocoronene (HBC) [33] structures, and porphyrins [34]. **Figure 4** portrays the AFM images of the **8Ph5Fc** (a,c) and **8Fc5C10** (b,d) fibers formed on the surface after the SVA treatment.

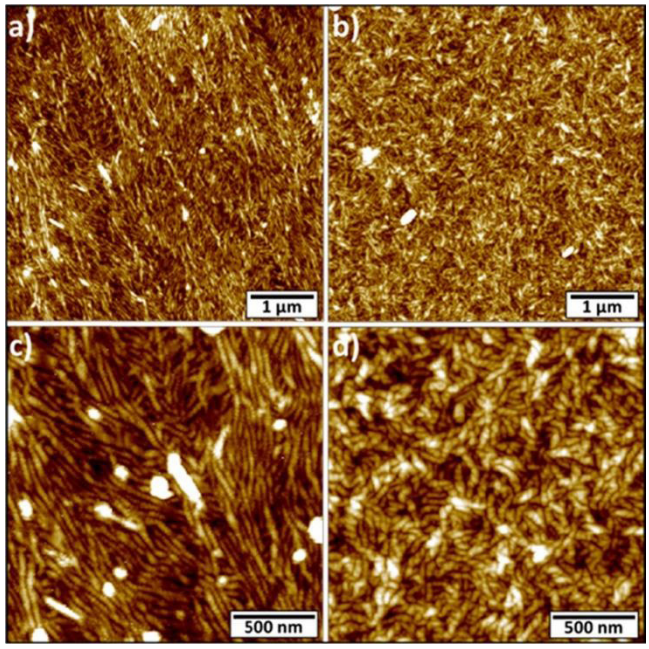

Figure 4. AFM images of supramolecular metal-free G aggregates drop-cast from CH_2Cl_2 0.6 mg/mL on HMDS-functionalized SiO2 after SVA (CH_2Cl_2 for 48 h). (a,c) Compound 8Ph5Fc. (b,d) Compound 8Fc5C10. Images Z-scales: (a) 13 nm; (b) 25 nm; (c) 12 nm; and (d) 20 nm.

Interestingly, the two compounds showed a similar behavior: in both cases, SVA caused an increased entanglement of the fibrillar structures, resulting in an extremely uniform coverage of the underneath substrate, which is no longer exposed. In particular, in the case of 8Ph5Fc, the as-deposited fibers show high rigidity and no tendency to entangle, causing the formation of holes and discontinuities in the resulting films, as shown in **Figure 3a,c**. After the SVA treatment, the fibers assemble into less-ordered bundles, forming a multilayered uniform film (**Figure** 4-2a,c). In the latter case, the fibers feature an average measured width of 41 ± 3 nm, suggesting that the packing at the molecular level is not affected by the SVA treatment, but it is not possible to correct the data with the previously used model because of the multilayer nature of the film after SVA. In the case of compound **8Fc5C10**, the SVA process exhibits a strong impact over the morphology of the films that undergo a dramatic decrease in roughness from 23.2 nm (before SVA, **Figures 3b,d**) to 4.15 nm (after SVA, **Figures 4b,d**). Moreover, the compound **8Fc5C10** fibers show completely different conformations: before SVA, the fibrillar structure is hardly visible, while after that, the fibrillar units are extremely well defined and form a strongly entangled network. On the other hand, samples of **8Ph5C10** showed no tendency to form crystalline structures. In this case, AFM characterization has not revealed any well-defined structures, and the films look amorphous.

Conclusion

In summary, we have designed and synthesized several organic soluble guanosines carrying either a phenyl or a ferrocenyl group at the C(8) position. Their self-assembly has been studied in solution by NMR and in thin films by means of AFM. Derivative **8Ph5Fc** shows the exclusive existence of isolated G4s in the CD_2Cl_2 solution, while compounds **8Fc5C10** and **8Ph5C10** do form isolated G4s as well, but another aggregated species is present in equilibrium in solution. The hierarchical self-assembly of **8Ph5Fc** and **8Fc5C10** leads to the formation of fibers, which can be deposited and characterized on surfaces. Guanosine **8Fc5C10** shows the formation of a disordered film, arising from the coexistence of different self-assembled species (probably a mixture of stacked G4s and H-bonded dimeric/oligomeric ribbon-like aggregates), whereas **8Ph5Fc** cleanly assembles into unprecedented, stacked cation-free G4 architectures. The ferrocenyl moiety of **8Fc5C10** seems to be not large enough to drive the self-assembly toward the exclusive existence of isolated G4s in solution, while its shape seems to hamper π-stacking and hence a shift in equilibria toward (stacked) quartets in the solid state. On the other hand, the results obtained for **8Ph5C10** indicate that the self-assembly is not ruled uniquely by the nature of the C(8) substituent: the behavior observed only for **8Ph5Fc** suggests that also the nature of the 5′ substituent, although irrelevant for G4 formation, affects the subsequent self-assembly. These results further expand the range of supramolecular architectures that can be obtained in thin films and provide unambiguous evidence for the key role played by the subtle design of guanosine starting building blocks to control the hierarchical self-assembly motifs that can be attained.

Experimental Section

General Methods.

All the reactions requires anhydrous conditions were carried out under a dry argon atmosphere in oven- dried glassware. Macherey-Nagel polygram silica gel plates (layer thickness 0.20 mm) were used for thin layer chromatography (TLC) analyses. Column chromatography was performed on Geduran silica gel 60 (40–63 μm). Reagents and solvents, including dry solvents, were purchased from Sigma-Aldrich or TCI. Electrospray ionization (ESI) mass spectra were obtained from methanol solutions in either the positive or negative mode, with Micromass ZMD 4000 or ZQ- 4000 instruments. High-resolution mass spectrometry (HRMS) spectra were recorded on a Waters Xevo G2-XS QTof system. Nuclear magnetic resonance (NMR) spectra were recorded on Varian Inova (600, 400, or 300 MHz) spectrometers and referenced to the residual solvent resonance (s = singlet, bs = broad singlet, d = doublet, t = triplet, q = quartet, qi = quintet, m = multiplet; coupling constant are in Hz). Structural assignments were made with additional information from gCOSY (gradient-selected correlation spectroscopy), gHSQC (gradient-selected heteronuclear single-quantum corre- lation), and gHMBC (gradient-selected heteronuclear multiple bond correlation) experiments. Diastereotopic protons/carbons were not assigned. CD spectra were recorded on a Jasco J-710 spectropolarimeter. Synthetic schemes with compound numbering are reported in the following information.

Microscopy Studies.

The AFM study of the self-assembled 1, 4, and 5 was performed using Veeco/Bruker Dimension 3100 that runs with a Nanoscope IV controller. Solutions of investigated molecules were prepared in 0.6 mg/mL CH_2Cl_2 and deposited by drop-casting (150 μL) on clean SiO_2/Si (230 ± 10 nm SiO_2 on [100] Si) functionalized with a monolayer of HMDS. The SVA treatment was performed by placing the compound films in a sealed environment and saturating with CH_2Cl_2 vapor under ambient conditions, for 48 h. The raw AFM data were processed through the application of background flattening.

Synthesis

8-Bromo Guanosine 9. The compound was prepared according to a literature procedure [35]. Thus, commercial guanosine 5 (1.00 g, 3.53 mmol) was suspended in 60 mL of an acetonitrile/water 2:1 mixture, and N-bromosuccinimide (943 mg, 5.3 mmol, 1.5 eq) was added in three portions over 20 min. Stirring was continued until TLC (DCM/MeOH 8:2) revealed the disappearance of the starting material (2 h). Solvents were then removed in vacuo, and the pale yellow solid thus obtained was suspended in acetone (20 mL) and stirred at room temperature for 2 h. The flask was then placed in a refrigerator and left overnight at −20 °C. The precipitate was filtered and washed several times with cold acetone to afford 1.09 g, 3.02 mmol (yield 86%) of 8-bromo guanosine 9 as a white solid.

8-Bromo-5'-O-tert-butyldimethylsilyl Guanosine 10. 8-Bromo guanosine 9 (1.274 g, 3.52 mmol) was dried at 50 °C over P_2O_5 in vacuo for 2 h and dissolved in dimethylformaimde (DMF) (17 mL). Imidazole (491 mg, 7.21 mmol, 2.05 eq) was added. To the resulting mixture was then added dropwise a solution of t-butyldimethylsilyl chloride (558 mg, 3.70 mmol, 1.05 eq.) in tetrahydrofuran (THF) (9 mL), and stirring was continued for 2 h. As TLC (CH_2Cl_2/MeOH 8:2) revealed the presence of unreacted starting material, an extra amount of imidazole (120 mg, 1.76 mmol, 0.5 eq.) and tbutyldimethylsilyl chloride (266 mg, 1.76 mmol, 0.5 eq.) was added, and reaction was continued for 2 h. The crude mixture was poured into water (50 mL), and the precipitate was filtered, washed with water and Et2O, and dried to afford the product (1.04 g, 2.19 mmol, 62%) as a white solid. RF = 0.6 (CH_2Cl_2 /MeOH 8:2).

8-Phenyl-5'-O-tert-butyldimethylsilyl Guanosine 11. PdCl2(PPh3)2 (59.0 mg, 0.084 mmol, 0.2 eq.) was added to a degassed solution of 10 (200 mg, 0.421 mmol), phenylboronic acid (77 mg, 0.630 mmol, 1.5 eq.), and K_3PO_4 (223 mg, 1.05 mmol) in 7 mL of a 6:1 mixture of dioxane/water. The mixture was heated at 95 °C for 22 h in an oil bath. After cooling to room temperature, solvents were removed by distillation, the dark residue was suspended in 50 mL of Et_2O and filtered. The filtrate was washed with brine (40 mL) and 1 N HCl (6 mL) and then dried over $MgSO_4$. The precipitate was washed with a CH_2Cl_2/MeOH 4:1 mixture; washings were combined with the ethereal residue, and solvents were removed in vacuo. The residue was purified by column chromatography on silica gel (CH_2Cl_2/MeOH 95:5), and the product was obtained in a 61% yield (121 mg, 0.256 mmol) as a white solid. RF = 0.2 (CH_2Cl_2/MeOH 9:1).

8-Phenyl-5'-O-tert-butyldimethylsilyl-2',3'-O-didecanoyl Guanosine 3 *(8Ph5Si).*
8-Phenyl-5'-O-tert-butyldimethylsilyl guanosine 11 (100 mg, 0.211 mmol) was dried in vacuo over P_2O_5 at 50 °C for 1 h and dissolved in 15 mL of an acetonitrile/toluene 2:1 mixture. Decanoic anhydride (163 μL, 0.444 mmol, 2.10 eq.), Et_3N (64 μL, 0.444 mmol, 2.10 eq.), and a small amount of 4-dimethylaminopyridine (DMAP) were then added, and the mixture was heated at 80 °C in an oil bath for 7 h. After cooling to room temperature, MeOH (0.5 mL) was added, and stirring was continued for 20 min. Solvents were removed by distillation, the residue was dissolved in CH_2Cl_2, washed with 5% $NaHCO_3$ and brine, and dried over $MgSO_4$. After the removal of solvents, the residue was purified by chromatography on silica gel (CH_2Cl_2/MeOH 99:1), and the product (120 mg, 0.153 mmol) was obtained as a white solid in 72% yield. RF = 0.36 (CH_2Cl_2/MeOH 97:3).

8-Phenyl-2',3'-O-didecanoyl Guanosine 2 (8Ph5OH). To a solution of 3 (120 mg, 0.153 mmol) in THF (4 mL) were added 72.5 mg (0.230 mmol, 1.5 eq) of tetra-n-butylammonium fluoride (TBAF). The mixture was stirred at room temperature until TLC (DCM/MeOH 92:8) showed complete disappearance of the starting material. The reaction mixture was concentrated, redissolved in DCM, and washed with sat. $NaHCO_3$ (3 × 10 mL). The organic phase was dried over $MgSO_4$, and solvents were removed by distillation. The residue was purified on silica gel by first eluting with Et_2O and then with DCM/MeOH 95:5. The product was obtained as a white solid in a 73% yield (75 mg, 0.112 mmol). RF = 0.28 (CH_2Cl_2/MeOH 92:8).

8-Phenyl-5'-O-ferrocenoyl-2',3'-O-didecanoyl Guanosine 1 *(8Ph5Fc).* Ferrocene carboxylic acid (77.5 mg, 0.337 mmol, 1.3 eq.) was dried in vacuo at 50 °C for 1 h and dissolved in THF (9 mL). Et_3N (175 μL, 1.217 mmol, 4.7 eq.) was added, and the resulting solution was cooled to 0 °C. Methanesulfonyl chloride (25.5 μL, 0.311 mmol, 1.2 eq.) was added, and the mixture was allowed to warm to room temperature and stirred for 2 h. A solution of vacuum-dried 8-phenyl-2',3'-O-didecanoyl guanosine 2 (173 mg, 0.259 mmol) in THF (6 mL) was then added, followed by a catalytic amount of DMAP. Stirring was continued for 24 h, MeOH (0.5 mL) was added, and the reaction mixture was concentrated in vacuo. The residue was dissolved in CH_2Cl_2, washed with water, and dried over $MgSO_4$. The solvent was removed by distillation, and the residue was purified by chromatography on silica gel (gradient from CH_2Cl_2 to CH_2Cl_2/MeOH 99:1), affording the product (85 mg, 0.097 mmol) as a yellow solid in 38% yield. RF = 0.24 (CH_2Cl_2/MeOH 9:1).

8-Phenylguanosine 12. To a degassed mixture of 9 (273 mg, 0.754 mmol), phenylboronic acid (110 mg, 0.902 mmol), Na_2CO_3 (160 mg, 1.51 mmol), tris(3-sulfonatophenyl)phosphine (TPPTS) (11 mg, 0.0194 mmol) in H_2O (2.4 mL), and acetonitrile (1.2 mL) were added 44 mg (0.0196 mmol) of $Pd(OAc)_2$, and the reaction mixture was stirred at 83 °C in an oil bath overnight. TLC (RP18, H_20/CH_3OH 1:1) confirmed the disappearance of the starting material. The reaction mixture was then cooled to room temperature and diluted with water (20 mL). The pH was adjusted to 7 with 1 N HCl. The resulting suspension was refluxed for a short time, cooled to room temperature, and maintained at 4 °C for 2 h. The precipitate was filtered, washed with water, and air-dried to afford the product as a white solid in 80% yield (216 mg, 0.60 mmol). The compound was sufficiently pure and was used in the following step without further purification.

8-Phenyl-2',3',5'-O-tridecanoyl Guanosine 4 (8Ph5C10). To a stirred suspension of 12 (97 mg, 0.27 mmol) in MeCN (4 mL) were added Et_3N (0.19 mL, 1.35 mmol), decanoic anhydride (0.33 mL, 0.89 mmol), and a catalytic amount of DMAP. The mixture was stirred at room temperature and monitored by TLC (DCM/MeOH 8:2). After 2 h, the mixture was concentrated under reduced pressure, and the resulting oil was partitioned between DCM and water. The organic layer was collected, the solvent was removed by distillation, and the residue was purified by column chromatography on silica (DCM/acetone 9:2.5 to remove decanoic acid and then DCM/ MeOH 9:1) to afford triester 4 as a white waxy solid in 59% yield (131 mg, 0.16 mmol).

8-Ferrocenylguanosine 13. A mixture of 9 (0.300 g, 0.83 mmol), dimethoxyethane (DME) (12 mL), ferroceneboronic acid (0.286 g, 1.24 mmol, 1.5 eq), and NaOH (3 M, 5.25 mL, 15.75 mmol) was degassed with a stream of Ar for 40 min in an ultrasonic bath. $PdCl_2(PPh_3)_2$ (0.058 g, 0.1 eq) was added, and the resulting solution was refluxed at 85 °C under argon in an oil bath for 48 h. The solvent was then removed under reduced pressure, the reaction mixture was neutralized with 10% HCl, and the solid was filtered, washed with water, and dried. The product thus obtained was used in the subsequent step without further purification. An analytical sample was obtained by chromatography on silica (DCM/MeOH 8:2). RF = 0.17 (DCM/MeOH 9:1).

8-Ferrocenyl-2′,3′,5’-O-tridecanoyl Guanosine 5 (8Fc5C10). Crude 8-ferrocenylguanosine 13 (0.430 g, 1.0 eq, 0.92 mmol) was dried over P_2O_5 in vacuo for 2 h at 55 °C and then suspended in 30 mL of an acetonitrile–toluene 1:1 mixture. Decanoic anhydride (443 μL, 3.15 eq, 2.90 mmol) and triethylamine (209 μL, 3.15 eq, 2.90 mmol) were then added, followed by a catalytic amount of 4- dimethylamino pyridine. The mixture was stirred under argon for 14 h at 80 °C in an oil bath. A second aliquot of decanoic anhydride (443 μL, 3.15 eq, 2.90 mmol) and triethylamine (TEA) (209 μL, 3.15 eq, 2.90 mmol) was added, and stirring was continued for 12 h at the same temperature. The solvent was removed under reduced pressure, and the crude was dissolved in dichloromethane and extracted with a sat. $NaHCO_3$ and brine. The organic layer was dried over $MgSO_4$. The crude reaction mixture was then applied to a silica gel column packed in DCM and eluted with a mixture of DCM–methanol (from 99:1 to 95:5). The product was obtained as an orange glass in 23% yield (196 mg, 0.21 mmol).

8-Ferrocenyl-5’-O-tert-butyldimethylsilyl Guanosine 14. A mixture of 13 (0.135 g, 0.29 mmol), imidazole (39 mg, 0.58 mmol), and t-butyldimethylsilyl chloride (48 mg, 0.32 mmol) in DMF (3 mL) was stirred at room temperature for 2 h. After the completion of the reaction (TLC DCM/MeOH 8:2), water (10 mL) was added, and the resulting precipitate was filtered and washed with water. The dry residue was purified by column chromatography (DCM/MeOH 92:8) to afford the product as a white solid in 62% yield (104 mg, 0.18 mmol). RF = 0.6 (CH_2Cl_2/MeOH 8:2).

8-Ferrocenyl-5’-O-tert-butyldimethylsilyl-2′,3’-O-didecanoyl Guanosine 6 (8Fc5Si). To a suspension of 14 (71 mg, 0.12 mmol) in MeCN (4 mL) were added Et_3N (45 μL, 0.32 mmol), decanoic anhydride (100 μL, 0.27 mmol), and a catalytic amount of DMAP. The mixture was stirred at room temperature for 4 h. MeOH (0.2 mL) was then added, and solvents were removed under reduced pressure. The residue was partitioned between DCM (20 mL) and water (10 mL). The organic layer was further washed with water (10 mL) and concentrated in vacuo to give an orange glassy solid, which was purified by column chromatography on silica (gradient from pure DCM to DCM/MeOH 97:3). Pure DCM (300 mL ca.) was used to elute decanoic acid, and then, DCM/MeOH 97:3 was used to elute two orange bands: the first one consisting of pure 6 (55 mg, 0.06 mmol, yield 50%), while the second one containing the desilylated derivative 7 formed during work-up.

8-Ferrocenyl-2′,3’-O-didecanoyl Guanosine 7 (8Fc5OH). To a solution of 6 (55 mg, 0.06 mmol) in 3 mL of THF were added 30 mg (0.09 mmol) of TBAF.$3H_2O$, and the mixture was stirred at room temperature for 20 h. The solvent was removed by evaporation, and the residue was dissolved in DCM (15 mL) and washed sequentially with 5% $NaHCO_3$ (5 mL) and water (5 mL, 4 times). The organic fraction was then dried over Na_2SO_4, and the solvent was removed by distillation. The residue was purified by chromatography on silica gel (gradient from pure DCM to DCM/MeOH 96:4) to afford 7 (33 mg, 0.04 mmol) as yellowish glass in 69% yield. RF = 0.32 (DCM/MeOH 95:5).

8-Ferrocenyl-5'-O-benzoyl-2',3'-O-didecanoyl Guanosine 8 (8Fc5Ph). Guanosine derivative 7 (54 mg, 0.07 mmol) was dried in vacuo over P_2O_5 at 50 °C for 2 h and then dissolved in DMF (1 mL). To the resulting solution were added Et_3N (15 μL, 0.10 mmol), benzoic anhydride (21 mg, 0.09 mmol), and a catalytic amount of DMAP. The mixture was stirred at room temperature for 8 h, and then, water (10 mL) and DCM (10 mL) were added. The organic phase was washed with water (10 mL), and the combined aqueous fractions were washed with DCM (2 × 5 mL). The organic fractions were combined, and solvents were removed under reduced pressure. The residue was purified by chromatography on silica (DCM/MeOH 96:4) to afford derivative 8 (52 mg, 0.06 mmol) as a yellow–orange solid in 85% yield. RF = 0.13 (DCM/MeOH 96:4).

Synthetic schemes

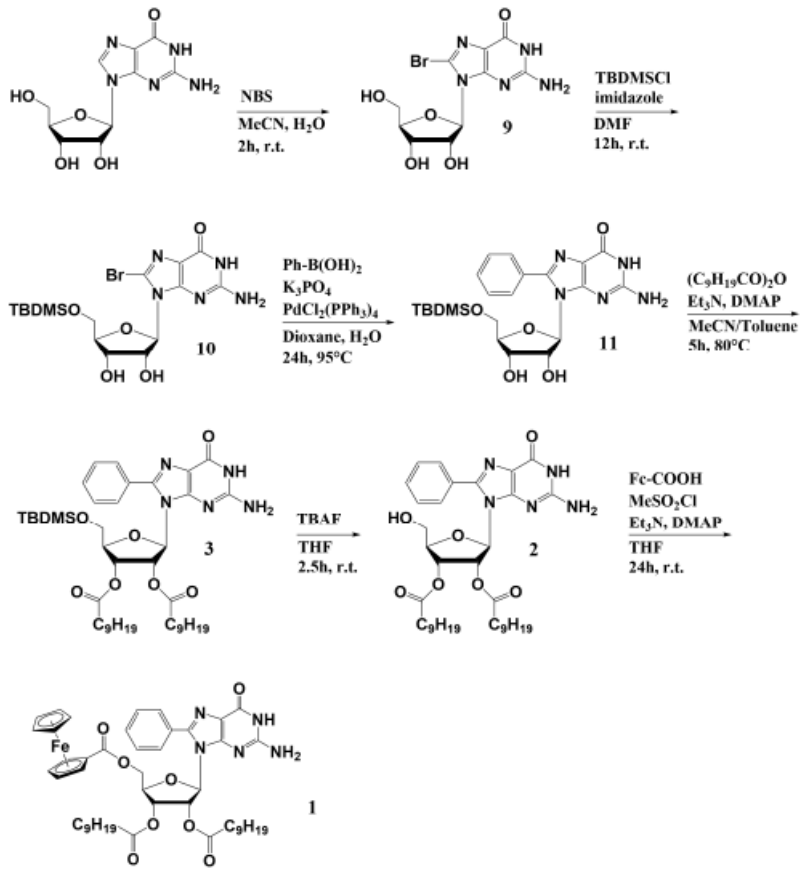

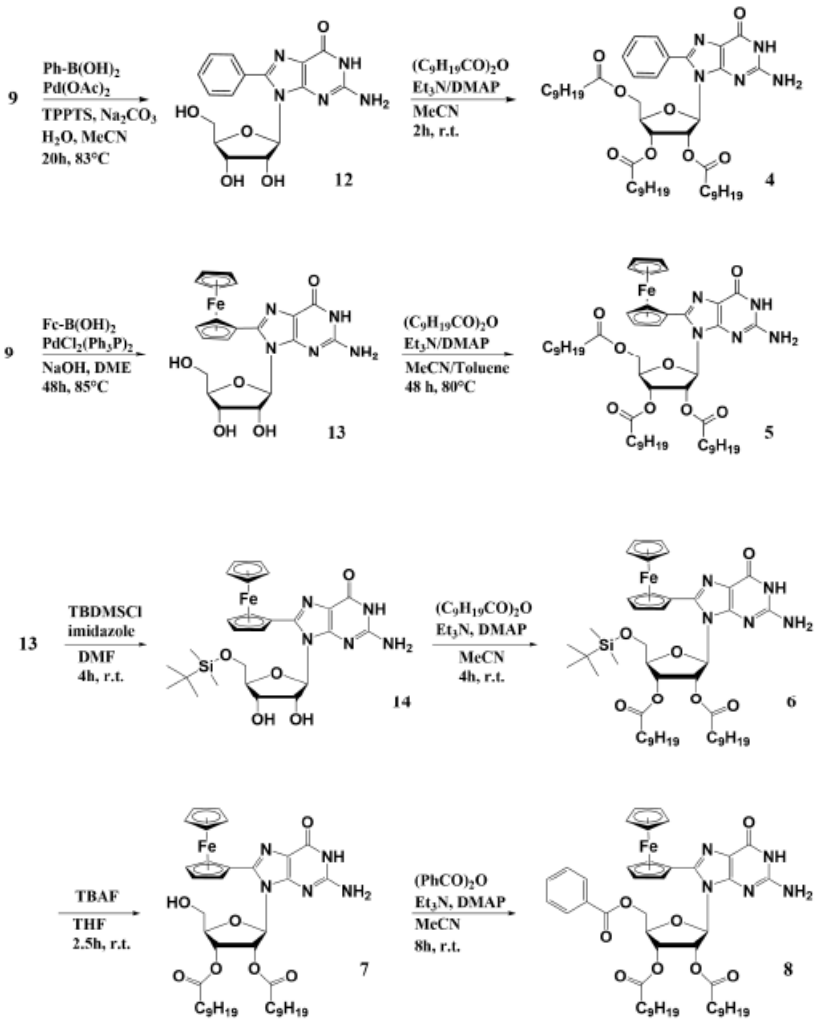
9
Ph-B(OH)2
Pd(OAc)2
TPPTS, Na2CO3
H2O, MeCN
20h, 83°C
12
(C9H19CO)2O
Et3N/DMAP
MeCN
2h, r.t.
4
9
Fc-B(OH)2
PdCl2(Ph3P)2
NaOH, DME
48h, 85°C
13
(C9H19CO)2O
Et3N/DMAP
MeCN/Toluene
48 h, 80°C
5
13
TBDMSCl
imidazole
DMF
4h, r.t.
14
(C9H19CO)2O
Et3N, DMAP
MeCN
4h, r.t.
6
TBAF
THF
2.5h, r.t.
7
(PhCO)2O
Et3N, DMAP
MeCN
8h, r.t.
8

References

[1] Stefan, L., & Monchaud, D. (2019). Applications of guanine quartets in nanotechnology and chemical biology. Nature Reviews Chemistry, 3, 650-668.

[2] Davis, J. T., & Spada, G. P. (2007). Supramolecular architectures generated by self-assembly of guanosine derivatives. Chemical Society Reviews, 36, 296-313.

[3] Arnal-Herault, C., Pasc, A., Michau, M., Cot, D., Petit, E., & Barboiu, M. (2007). Functional G-Quartet Macroscopic Membrane Films. Angewandte Chemie International Edition, 46, 8409-8413.

[4] Yoshikawa, I., Sawayama, J., & Araki, K. (2008). Highly stable giant supramolecular vesicles composed of 2D hydrogen-bonded sheet structures of guanosine derivatives. Angewandte Chemie International Edition, 47, 1038-1041.

[5] Sakaino, H., Sawayama, J., Kabashima, S., Yoshikawa, I., & Araki, K. (2012). Dry micromanipulation of supramolecular giant vesicles on a silicon substrate: highly stable hydrogen-bond-directed nanosheet membrane. Journal of the American Chemical Society, 134, 15684-15687.

[6] Ciesielski, A., El Garah, M., Masiero, S., & Samorì, P. (2016). Self-assembly of natural and unnatural nucleobases at surfaces and interfaces. Small, 12, 83-95.

[7] Sutyak, K. B., Lee, W., Zavalij, P. V., Gutierrez, O., & Davis, J. T. (2018). Templating and catalyzing [2+2] photocycloaddition in solution using a dynamic G-quadruplex. Angewandte Chemie International Edition, 57, 17146-17150.

[8] Lena, S., Neviani, P., Masiero, S., Pieraccini, S., & Spada, G. P. (2010). Triggering of guanosine self-assembly by light. Angewandte Chemie International Edition, 49, 3657-3660.

[9] Lena, S., Masiero, S., Pieraccini, S., & Spada, G. P. (2009). Guanosine hydrogen-bonded scaffolds: A new way to control the bottom-up realization of well-defined nanoarchitectures. Chemistry - A European Journal, 15, 7792-7806.

[10] Ciesielski, A., Lena, S., Masiero, S., Spada, G. P., & Samorì, P. (2010). Dynamers at the solid-liquid interface: Controlling the reversible assembly/reassembly process between two highly ordered supramolecular guanine motifs. Angewandte Chemie International Edition, 49(11), 1963-1966.

[11] Gonzalez-Rodriguez, D., Janssen, P. G. A., Martin-Rapun, R., De Cat, I., De Feyter, S., Schenning, A. P. H. J., & Meijer, E. W. (2010). Persistent, well-defined, monodisperse, π-conjugated organic nanoparticles via G-quadruplex self-assembly. Journal of the American Chemical Society, 132(13), 4710-4719.

[12] Rhodes, D., & Lipps, H. J. (2015). G-quadruplexes and their regulator roles in biology. Nucleic Acids Research, 43(18), 8627-8637.

[13] Rivera, J. M. (2013). In Guanine quartets: Structure and application (Fritzsche, W. & Spindler, L. Eds.), (pp. 15-27). RSC Publishing.

[14] Sutyak, K. B., Zavalij, P. Y., Robinson, M. L., & Davis, J. T. (2016). Controlling molecularity and stability of hydrogen bonded G-quadruplexes by modulating the structure's periphery. Chemical Communications, 52(74), 11112-11115.

[15] Martin-Hidalgo, M., Garcia-Arriaga, M., Gonzalez, F., & Rivera, J. M. (2015). Tuning supramolecular G-quadruplexes with mono- and divalent cations. Supramolecular Chemistry, 27(3-4), 174-180.

[16] Marlow, A. L., Mezzina, E., Spada, G. P., Masiero, S., Davis, J. T., & Gottarelli, G. (1999). Cation-templated self-assembly of a lipophilic deoxyguanosine: Solution structure of a K+-dG8 octamer. The Journal of Organic Chemistry, 64(15), 5116-5123.

[17] Mezzina, E., Mariani, P., Itri, R., Masiero, S., Pieraccini, S., Spada, G. P., Spinozzi, F., Davis, J. T., & Gottarelli, G. (2001). The Self-Assembly of a Lipophilic Guanosine Nucleoside into Polymeric Columnar Aggregates: The Nucleoside Structure Contains Sufficient Information To Drive the Process towards a Strikingly Regular Polymer. Chem. –Eur. J., 7, 388–395.

[18] Bare, G. A. L., Liu, B., & Sherman, J. C. (2013). Synthesis of a Single G-Quartet Platform in Water. J. Am. Chem. Soc., 135, 11985−11989.

[19] El Garah, M., Perone, R. C., Santana-Bonilla, A., Haar, S., Campitiello, M., Gutierrez, R., Cuniberti, G., Masiero, S., Ciesielski, A., & Samori, P. (2015). Guanosine-based hydrogen-bonded 2D scaffolds: metal-free formation of G-quartet and G-ribbon architectures at the solid/liquid interface. Chem. Commun., 51, 11677−11680.

[20] Inui, Y., Shiro, M., Fukuzumi, S., & Kojima, T. (2013). Quartet formation of a guanine derivative with an isopropyl group: crystal structures of "naked" G-quartets and thermodynamics of G-quartet formation. Org. Biomol. Chem., 11, 758−764.

[21] Sessler, J. L., Sathiosatham, M., Doerr, K., Lynch, V., & Abboud, K. A. (2000). A G-Quartet Formed in the Absence of a Templating Metal Cation: A New 8-(N,N-dimethylaniline]guanosine Derivative. Angew. Chem., Int. Ed., 39, 1300−1303.

[22] Murat, P., Gennaro, B., Garcia, J., Spinelli, N., Dumy, P., & Defrancq, E. (2011). The Use of a Peptidic Scaffold for the Formation of Stable Guanine Tetrads: Control of a H-bonded Pattern in Water. Chem. – Eur. J., 17, 5791−5795.

[23] Nikan, M., & Sherman, J. C. (2009). Cation-Complexation Behavior of Template-Assembled Synthetic G-Quartets. J. Org. Chem., 74, 5211−5218.

[24] Masiero, S., Trotta, R., Pieraccini, S., De Tito, S., Perone, R., Randazzo, A., & Spada, G. P. (2010). A non-empirical chromophoric interpretation of CD spectra of DNA G-quadruplex structures. Org. Biomol. Chem., 8, 2683−2692.

[25] Claridge, T. D. V. (1999). High-Resolution NMR Techniques in Organic Chemistry (3rd ed.). Pergamon-Elsevier.

[26] Buerkle, L. E., von Recumab, H. A., & Rowan, S. J. (2012). Toward potential supramolecular tissue engineering scaffolds based on guanosine derivatives. Chem. Sci., 3, 564−572.

[27] Kotch, F. W., Sidorov, V., Lam, Y.-F., Kayser, K. J., Li, H., Kaucher, M. S., & Davis, J. T. (2003). Water-Mediated Association Provides an Ion Pair Receptor. J. Am. Chem. Soc., 125, 15140−15150.

[28] Liscio, A., Palermo, V., & Samorì, P. (2008). Probing Local Surface Potential of Quasi-One-Dimensional Systems: A KPFM Study of P3HT Nanofibers. Adv. Funct. Mater., 18, 907−914.

[29] Ciuchi, F., Dinicola, G., Franz, H., Gottarelli, G., Mariani, P., Bossi, M. G. P., & Spada, G. P. (1994). Self-Recognition and Self-Assembly of Folic Acid Salts: Columnar Liquid Crystalline Polymorphism and the Column Growth Process. J. Am. Chem. Soc., 116, 7064−7071.

[30] Hobza, P., & Šponer, J. (1999). Structure, Energetics, and Dynamics of the Nucleic Acid Base Pairs: Nonempirical Ab Initio Calculations. Chem. Rev., 99, 3247−3276.

[31] De Luca, G., Liscio, A., Maccagnani, P., Nolde, F., Palermo, V., Müllen, K., & Samorì, P. (2007). Nucleation-Governed Reversible Self-Assembly of an Organic Semiconductor at Surfaces: Long-Range Mass Transport Forming Giant Functional Fibers. Adv. Funct. Mater., 17, 3791−3798.

[32] Kim, D. H., Lee, D. Y., Lee, H. S., Lee, W. H., Kim, Y. H., Han, J. I., & Cho, K. (2007). High-Mobility Organic Transistors Based on Single- Crystalline Microribbons of Triisopropylsilylethynyl Pentacene via Solution-Phase Self-Assembly. Adv. Mater., 19, 678−682.

[33] De Luca, G., Liscio, A., Nolde, F., Scolaro, L. M., Palermo, V., Müllen, K., & Samorì, P. (2008). Self-assembly of discotic molecules into mesoscopic crystals by solvent-vapour annealing. Soft Matter, 4, 2064−2070.

[34] El Garah, M., Bonilla, A. S., Ciesielski, A., Gualandi, A., Mengozzi, L., Fiorani, A., Iurlo, M., Marcaccio, M., Gutierrez, R., Rapino, S., Calvaresi, M., Zerbetto, F., Cuniberti, G., Cozzi, P. G., Paolucci, F., & Samorì, P. (2016). Molecular design driving tetraporphyrin self-assembly on graphite: A joint STM, electrochemical and computational study. Nanoscale, 8(25), 13678-13686.

[35] Gillet, L. C. J., & Schärer, O. D. (2002). Preparation of C8-amine and acetylamine adducts of 2'-deoxyguanosine suitably protected for DNA synthesis. Organic Letters, 4(24), 4205-4208.

CHAPTER 7

Unraveling the structure of Silver(I)-Guanosine complex

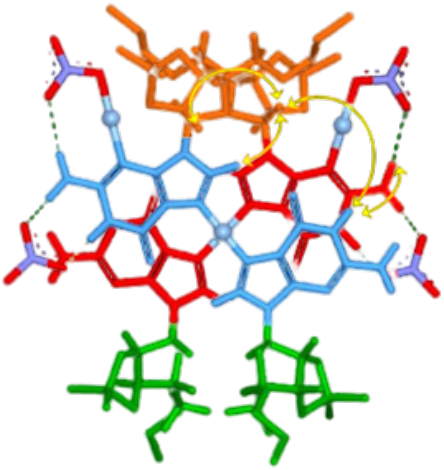

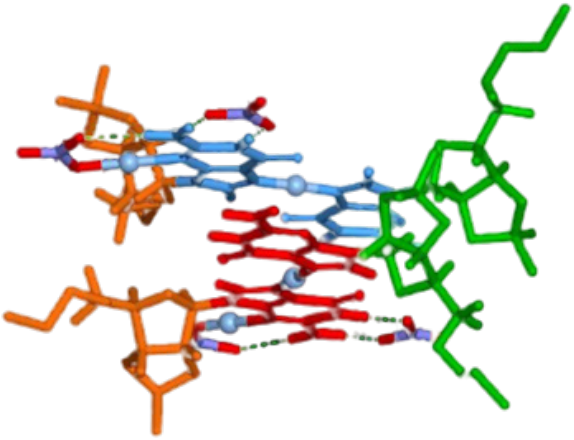

This project was carried out in collaboration with Stefano Masiero, Silvia Pieraccini and Andrea Mazzanti.

Introduction

The effect of metal ions on DNA and RNA structure and function is well documented in its biological aspects and has found many clinical applications. In recent years, researchers in biotechnology, analytical sensors and materials science have also turned their attention to this field [1], attracted by the possibilities stemming from a programmed introduction of metal ions into nucleic acids sequences [2]. While platinum and gold are the most common metals found in pharmaceutically active organometallic complexes, the use of silver as an antibacterial has been known since long and many promising anticancer and antifungal silver complexes have been proposed in recent years [3] Although a complete understanding of the mechanism of action of silver-containing drugs is still lacking, there are evidences that silver antimicrobial activity can result from Ag(I) interaction with microbial DNA [4]. Among DNA nucleobases, Guanosine (G) derivatives are particularly interesting because the peculiar sequence of H-bond donors and acceptors present in the nucleobase, together with its aromatic surface, allows the controllable formation of several different self-assembled architectures [5]. Analogously to what happens for the hydrophilic counterparts, for lipophilic guanosine derivatives in the presence of alkali metal ions (e.g. K^+, Na^+, Cs^+, Ca^{2+}, Sr^{2+}) the formation of H-bonded cyclic tetramers (G-quartets) is normally observed. The metal ion has a templating effect, by coordinating the oxygen atoms of the nucleobases. These G-quartets, depending on experimental conditions, can pile up giving rise to highly ordered helically stacked arrays (G-quadruplexes) [6]. In the absence of metal ions the formation of G-quartets is seldom observed [7] and other H-bonded structures such as dimers, ribbons, 2D-sheets [8] are normally formed. Coordination to a transition metal ion (Ag^+, Cu^+, Hg^{2+} or Pt^{2+}) can further expand the library of supramolecular architectures obtainable from G derivatives, because these metals coordinate to electron-rich atoms of the nucleobase and strongly influence its H-bonding and recognition properties. In particular, it is known [9] that in G-rich (or C-rich) DNA sequences, Ag(I)-induced base pairing produces highly stable DNA duplexes, outpowering both Watson-Crick duplexes and G-quadruplexes. Given the robustness of these self-assembled structures, they have been proposed [10] as a tool in dynamic DNA nanomaterials. While the Ag-C complex has been studied in detail [2a, 11] there is no agreement in the literature on the Ag^+/G complex structure. Over the years, several structures have been proposed, on the basis of results obtained from solution studies, X-ray data or calculations on G derivatives ranging from model compounds to G-rich DNA sequences (**Figure 1**).

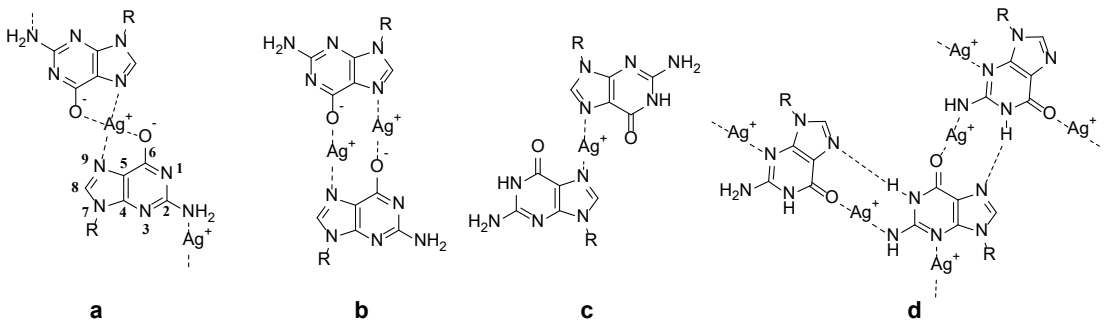

Figure 1. proposed structures for the G/Ag(I) complex.

From solution NMR experiments on guanosine in DMSO, Cini et Al. suggested a polymeric aggregate arising from dimeric chelate complexes (**Figure 1a**), involving both N7 and O6 with an overall Ag/G 1:1 stoichiometry. In this structure, nucleobases are in the anionic enolate form because preparation of the samples involved solubilisation of the nucleoside at pH 10 [12]. A dimeric chelate structure involving N7 and O6 (in enolate form, **Figure 1b**), with Ag/G 1:1 stoichiometry, was suggested for 5'-GMP (1-0.1 mM) at pH 8 (pK_A for 5'-GMP is 10.00) on the basis of rheological, calorimetric and electronic spectroscopy data [13]. In this paper, evidences for a base stacked aggregate were also reported. The existence of stacked aggregates was demonstrated by the formation of hydrogels from 5'-GMP:Ag(I) 1:1 complex at higher concentrations [14]. In this paper the same structure 1b for the complex was proposed, but Authors noted that, upon complex formation, the pH of the solution dropped to 5.0: changes in nuclobases pKa values upon metal coordination is a well-documented phenomenon, and in particular it is known that metal coordination at N7 increases the acidity of N1H [15]. A slight modification of structure 1b was proposed on the basis of UV, ECD and VCD studies on GMP at neutral and basic pH: the 1:1 G-Ag(I) complex was described as a dimer held together by N(7)-Ag-N(7) coordination bonds. Additional interdimer O(6)-Ag-O(6) coordination bonds drove the formation of assembled species arising from stacking of the dimers. Dimeric structures with a 1 to 2 Ag(I)/G stoichiometry (**Figure 1c**) were proposed on the basis of quantum chemical calculations [16] on model oligonucleotides and X-ray data [1b]: in this case coordination involves only N(7), while O(6) oxygens, as well as enolization/deprotonation phenomena, are not involved. This dimeric structure has been confirmed in the crystal structure of a short DNA strand complexed with Ag(I) [17]. Feng et Al. described a further structure (**Figure 1d**) with a 2:1 Ag(I)/G stoichiometry for the hydrogels formed by 2'-deoxy-2'-fluoroguanosine: in this case Ag(I) bridges O6 (or N3) and a deprotonated exocyclic amino group [18]. In order to contribute to the clarification of Ag(I)/G complex structure, we report here our studies on a model G derivative, namely the lipophilic derivative **LG1** (**Figure 2**), where the sugar primary alcoholic function was derivatized as n-decyl ether and the two secondary hydroxyl functions were converted into isopropylidene ketal. We reasoned that the use of a lipophilic derivative would have allowed us to bypass some of the difficulties often encountered in previous studies, like nucleoside solubility or interferences due to phosphate or water in the case of nucleotide, and possibly expand the library of supramolecular architectures obtainable from Guanosine.

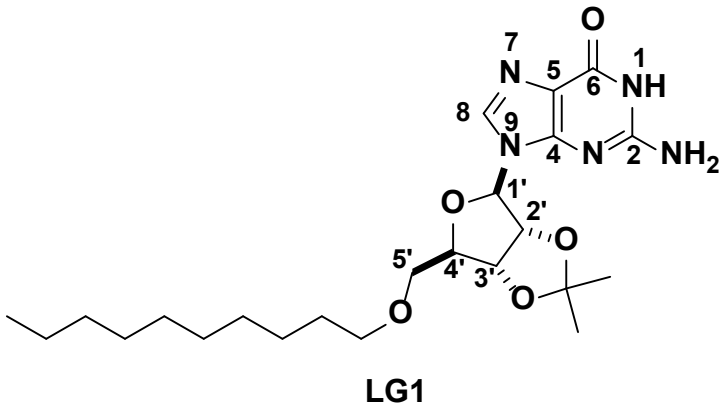

Figure 2. Molecule **LG1**

Results and discussion

UV spectrum recorded on **LG1** in chlorinated solvents shows an absorption maximum at *ca.* 260 nm beside a shoulder cantered at about 280 nm, corresponding to the long (260) and short (280) axis polarized pi-pi* electronic transitions of the guanine chromophore, respectively (**Figure 3**, light blue line). ECD spectrum of the same solution is characterised by two monosignate and very weak negative signals typical of monomeric or oligomeric H-bonded ribbon-like G-structures [19]. However, by addition of an excess of solid $AgNO_3$ with respect to **LG1**, salt is extracted into the organic solution and a drastic change of chiroptical properties takes place, indicating that the metal ion coordinates guanosines, thus leading to a new 'superchiral' self-assembled G-Ag species (**Figure 3**). In fact, under these conditions, an intense ECD signal with a positive-negative-positive sequence appears in the guanine absorption region, being the negative band at 267 nm predominant. The observed spectral trace can reasonably be ascribed to the concomitance of a positive exciton coupling emerging at ca. 280 nm and a negative one centred at ca. 260 nm, revealing chiral stacking between at least two adjacent guanine chromophores [20].

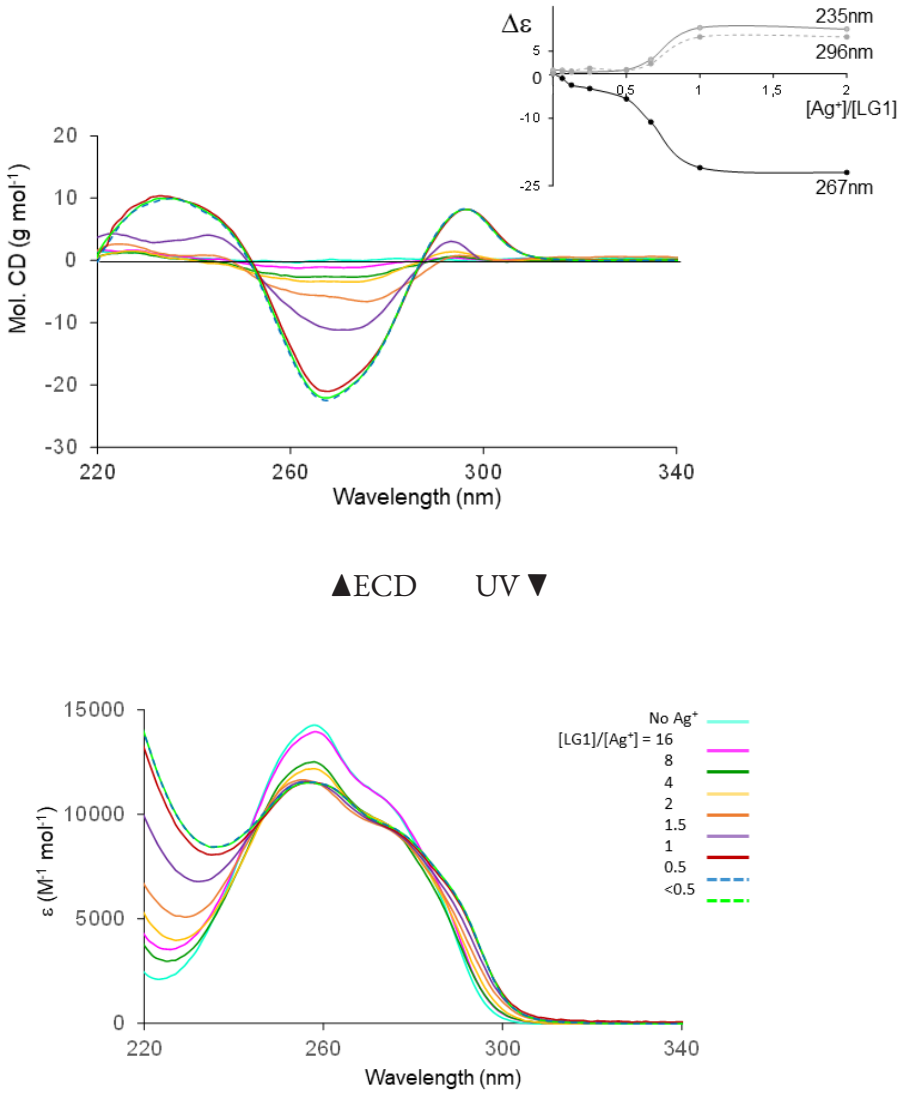

Figure 3. ECD and Uv spectra of **LG1**, in presence of $AgNO_3$ at different concentrations.

Dilution experiments evidence a good stability for the new structure. Indeed, ECD traces almost superimposable are obtained for concentrations ranging from 10 to 1 mM (in terms of G concentration), while ECD intensities tend to diminish by diluting the solution from 1 to 0.1 mM, likely due to disaggregation pathways. *VT*-ECD measurements performed in dichloromethane confirm the thermodynamic stability of the complex: a partial disaggregation is observed only at 90°C (30% ca. reduction of signal intensities), however ECD bands are completely recovered by cooling the solution to room temperature.

Titration experiments were performed with the aim of determining the [**LG1**] to [$AgNO_3$] stoichiometry of the complex. Thus, **LG1** solutions at a fixed concentration were added with increasing amounts of solid salt and UV/ECD measurements were carried out after stirring the samples to equilibrate the system (see experimental part). ECD spectra obtained for different [**LG1**]/[Ag^+] molar ratios are reported in **Figure 3**. By considering all the curves it can be noticed that different band shapes emerge during titration and isodichroic points cannot be detected. This observation suggests that the complexation process cannot be described by a two-state population model. On the contrary, different **LG1**-Ag complexes form during salt addition. Starting from the **LG1** solution (light blue line), a positive signal at ca. 290 nm and a negative broad band between 280 and 240 nm tend to increase with [Ag^+] up to a [**LG1**]/[Ag^+] molar ratio = 4 (yellow trace). When [**LG1**]/[Ag^+] becomes = 2 (orange trace) the negative optical activity becomes predominant with two minima at 265 and 255 nm, while the intense positive-negative-positive curve described above progressively appears as the molar ratio approaches 1. As highlighted also by the trends of 296, 267 and 235 nm CD values plotted against molar ratios (**Figure 3**), [**LG1**]/[Ag^+] = 1 represents a turning point of the complexation process. In fact, both CD intensities and band shapes are superimposable for molar ratios ≤ 1, indicating that maximum amount of salt has been extracted and that the 1 to 1 stoichiometry characterises the final G-Ag species. The same experiment was monitored by UV measurements. Spectra reported in **Figure 3** confirm the absence of isosbestic points as typically found in the case of a two species-equilibrium. As shown by the 260 nm absorbance values plotted against molar ratios, a hypochromic effect diagnostic of π-π stacking interactions between aromatic planes appears already at a molar ratio = 8, however it further increases and gains its maximum when molar ratio is = 1. Analogously to ECD, UV spectra obtained for molar ratios ≤ 1 result superimposable. In addition, they all show a peculiar red-shifted absorption in the 290 nm region, presumably ascribable to specific interactions between guanine planes composing the complex. Titration of **LG1** with $AgNO_3$ was also followed by NMR spectroscopy. Guanosine **LG1** likely forms H-bonded ribbon-like assemblies in chlorinated solvents [19], as its ^1H NMR spectrum in $CDCl_3$ (**Figure 4**, middle) shows quite broad signals, and both the amino (2-NH_2) and the imino (1-NH) protons participating to H-bonding result deshielded with respect to their resonances in DMSO (**Figure 4**, top).

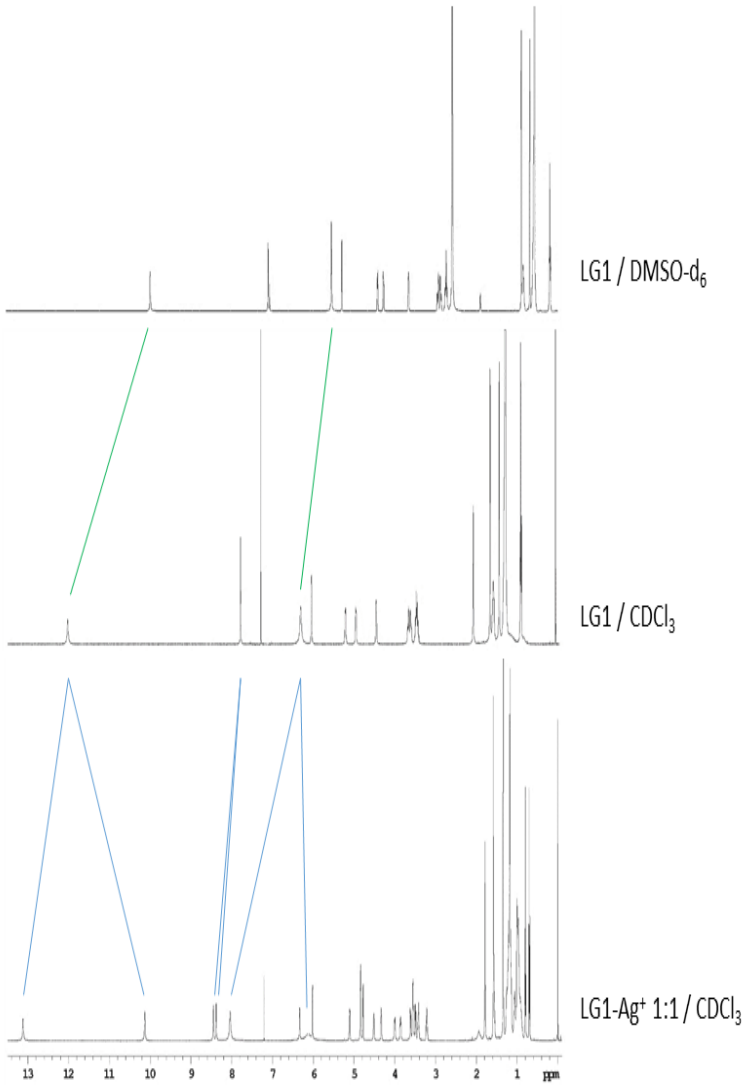

Figure 4. ^{1}HNMR spectra of **LG1** in different environments. Top) DMSO-d_6 Middle) $CDCL_3$ Bottom) $CDCL_3$ in presence of Ag^+ cation

By addition of 1/8 or 1/4 of $AgNO_3$ (**Figure 5**) a partial disaggregation of G-ribbons takes place, as evidenced by progressive deshielding of amino protons. In concomitance, new sets of sharp signals presumably related to emerging G-Ag species start to grow (see peaks labelled by black circles in **Figure 5b** and black stars in **Figure 5c**). In both cases, a residual amount of uncomplexed guanosine, arranged in dimers or ribbon-like oligomers, is still present in solution as revealed by detectable 1-NH, H-8 and 2-NH_2 peaks.

By further addition of salt, uncomplexed guanosine signals almost disappear and the spectrum shows only sharp signals of complexed species in varying amounts (**Figure 5c,d,e**). These intermediate complexes disappear completely when the molar ratio becomes 1 (**Figure 5f**).

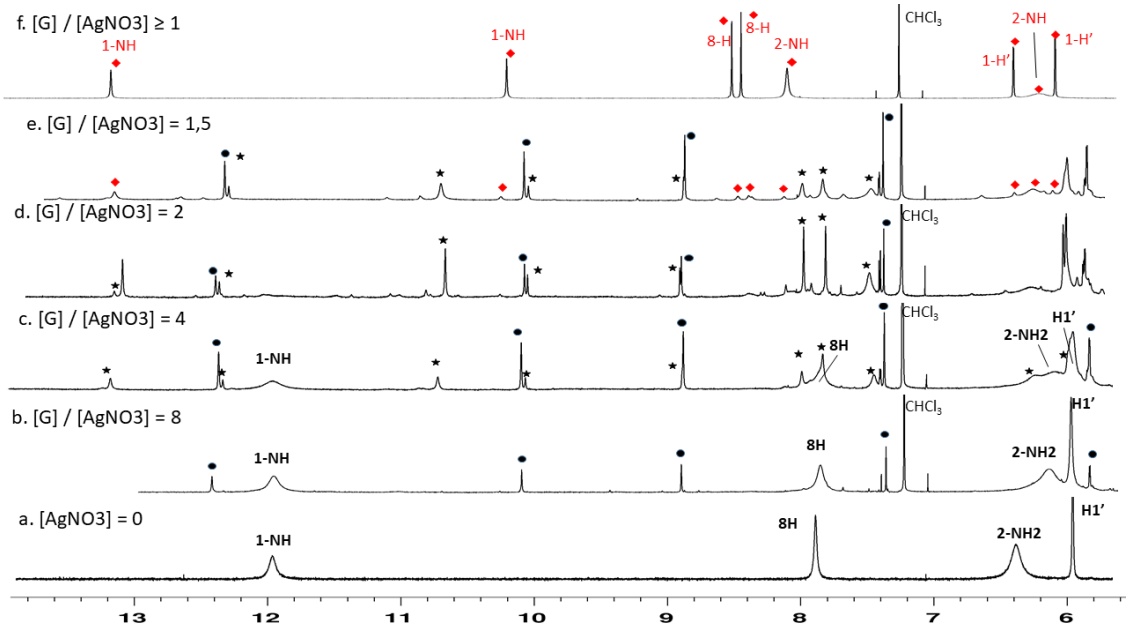

Figure 5. LG1+$AgNO_3$ ^{1}HNMR spectrum in $CDCl_3$. Progressive disaggregation of ribbons evidenced by the deshielding of amino protons and subsequent formation of the complex G-Ag.

In this case, the spectrum shows exclusively two new, well resolved and sharp sets of signals, with 1 to 1 relative intensity, which show the same diffusion coefficient in DOSY experiments. (**Figure 5f** and **Figure 4** bottom). In particular, the imino signal at 12.2 ppm splits into two signals: a remarkably downfield peak at 13.2 ppm, suggestive of H-bonding, and an up-field one at 10.2 ppm, being the latter chemical shift the same as the free imino proton in DMSO. The amino signal behaves analogously. The 1:1 G-Ag stoichiometry is compatible with structures a and b in **Figure 1**, but integration of signals shows that in our case no deprotonation occurs upon Ag^+ complexation, ruling out the involvement of enolate ions.

The spectrum does not change when further amounts of $AgNO_3$ are added, in agreement with what observed above from ECD and UV analyses. All these data are suggestive of the formation of a well-defined Ag-coordinated G complex characterised by a 1:1 G-Ag stoichiometry when [**LG1**]/[Ag^+] molar ratio is ≤ 1. Indeed, the second equivalent of Ag^+ seems crucial for the formation of the final complex, as its signals are absent in the 2:1 ratio NMR spectrum (**Figure 5d**). VT-^{1}H NMR measurements ruled out a possible aggregation of this complex to form higher molecular weight species, because no significant variation was observed in either chemical shift or linewidth of non-exchangeable protons on cooling the complex down to -50°C. It is important to notice that imino protons (see below) at 13.2 and 10.2 ppm show no significant shift, while both amino signals at 8.1 and 6.2 ppm split into two signals each upon cooling (8.50 and 7.91 ppm, 6.82 and 5.81 ppm, respectively at -50°C). Examination of spectra at different temperatures clearly shows that the two downfield signals originate from the fast-exchanging 8.1 ppm peak while the up-field couple comes from the 6.2 ppm one. No significant changes were observed in the spectrum on increasing concentrations from 10 to 150 mM. If kept in the dark, the complex is stable over time at least for months, and it can be dried and dissolved again with no changes in the ^{1}H-NMR spectrum.

The ^{13}C NMR spectrum shows an analogous behaviour (**Figure 6**): each signal of uncomplexed **LG1** splits into two signals in the **LG1**/Ag^+ 1:1 complex.

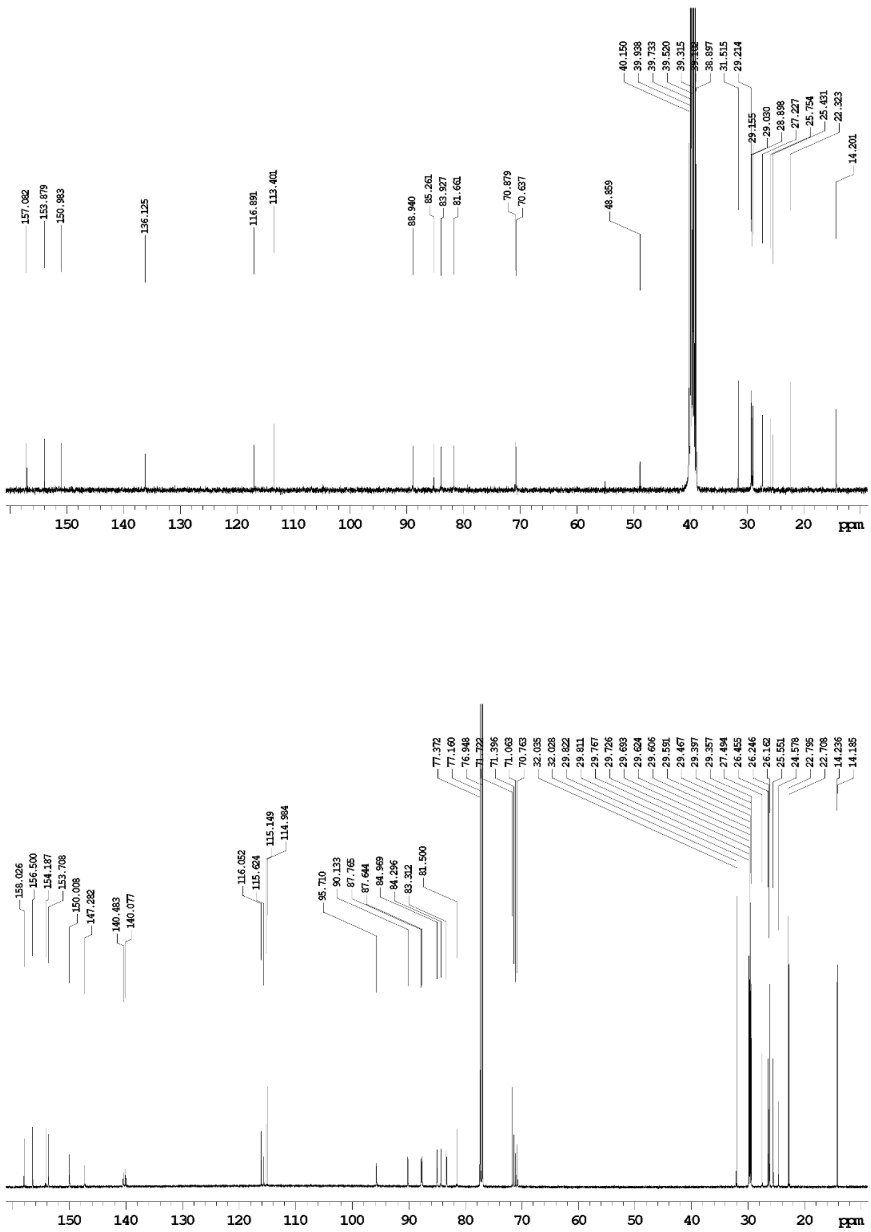

Figure 6. ^{13}C NMR of pure **LG1** in DMSO-d_6 (top) and of the **LG1**/Ag^+ 1:1 complex in $CDCl_3$ (bottom)

The two sets of signals suggest that the complex is either asymmetric or dissymmetric with C_n symmetry and they could in principle arise from the presence in the complex of either two tautomeric forms of **LG1** in slow exchange or two differently-coordinated guanosine ligands or two equally populated conformers.

Each NMR signal was assigned by means of 1D (^{1}H, ^{13}C and Noesy1D) and 2D (COSY, HSQC, HMBC, NOESY and ROESY) NMR experiments (**Tables 1** and **2**) and the two sets of signals were assigned to two different but equally populated conformers of **LG1**.

	T (°C)	N(1)H	N(2)H**A**	N(2)H**B**	H(8)	H(1')	H(2')	H(3')	H(4')	H(5')/H(5'')[a]
anti	25	13.18	8.10		8.44	6.40	4.57	4.84	4.9	4.07-4.06 3.56-3.55
	-50	13.16	8.50	5.81	8.25	6.34	4.57	4.85	4.94	4.03 3.52
syn	25	10.19	6.19		8.51	6.08	5.17	4.9	4.40	3.93-3.92 3.69-3.67
	-50	10.12	7.91	6.82	8.42	6.03	5.10	4.85	4.41	3.94 3.65

a. not assigned

Table 1. ^{1}H-NMR chemical shifts (ppm) for **LG1**/Ag 1:1 complex in $CDCl_3$ at r.t. and at -50°C.

	C2	C4	C5	C6	C8	C1'	C2'	C3'	C4'	C5'
anti	154.2 153.7[a]	147.3	115.6	158.0	140.1	95.7	87.8	83.3	87.6	71.1
syn		150.0	115.1	156.5	140.5	90.1	84.3	81.5	85.0	70.8

a. not assigned

Table 2. ^{13}C-NMR chemical shifts (ppm) for **LG1**/Ag 1:1 complex in $CDCl_3$ at r.t.

One set of signals arises from **LG1** in a *syn* conformation and the other set comes from molecules of **LG1** in an *anti* conformation around the N9-C1' glycosidic bond. Usually, assignment of signals to either syn or *anti* conformers can be easily done on the basis of NOE proximities between H8 and H1' or H2', being the latter greater than the former in the *anti* conformer, while the opposite holds for the *syn* conformer. In the present case, irradiation of both H8A and H8B gave an Overhauser effect on the corresponding H1' stronger than on H2' (see below). Hence, the attribution was done on the basis of $^{3}J_{CH}$ coupling constants. The actual $^{3}J_{CH}$ coupling constants were measured from a proton-coupled ^{13}C spectrum and are reported in **Table 3**.

	anti	*syn*
C4 / H1'	4.8	0
C8 / H1'	<2	3.3

Table 3. selected $^{3}J_{CH}$ coupling constants (Hz).

According to the fittings of the Karplus equations for the $^{3}J_{C8\text{-}H1'}$ and $^{3}J_{C4\text{-}H1'}$ coupling constants reported in the literature for guanosine [21] the measured constants are in agreement with a O4'-C1'-N9-C4 torsion angle in the 50°-80° range (characteristic of *syn* conformation) for one set of signals, while the second set arises from an *anti* conformer, with a O4'-C1'-N9-C4 torsion angle around 180°. The attribution is confirmed by the strong correlation observed between H5' and H8 for the *anti* conformer in NOESY-1D experiments, as opposed to the weak correlation between H5' and H8 observed for the *anti* (**Figure 7**).

The r.t. ^{1}H-NMR spectrum of the 1:1 complex together with peaks assignment is shown in **Figure 7.**

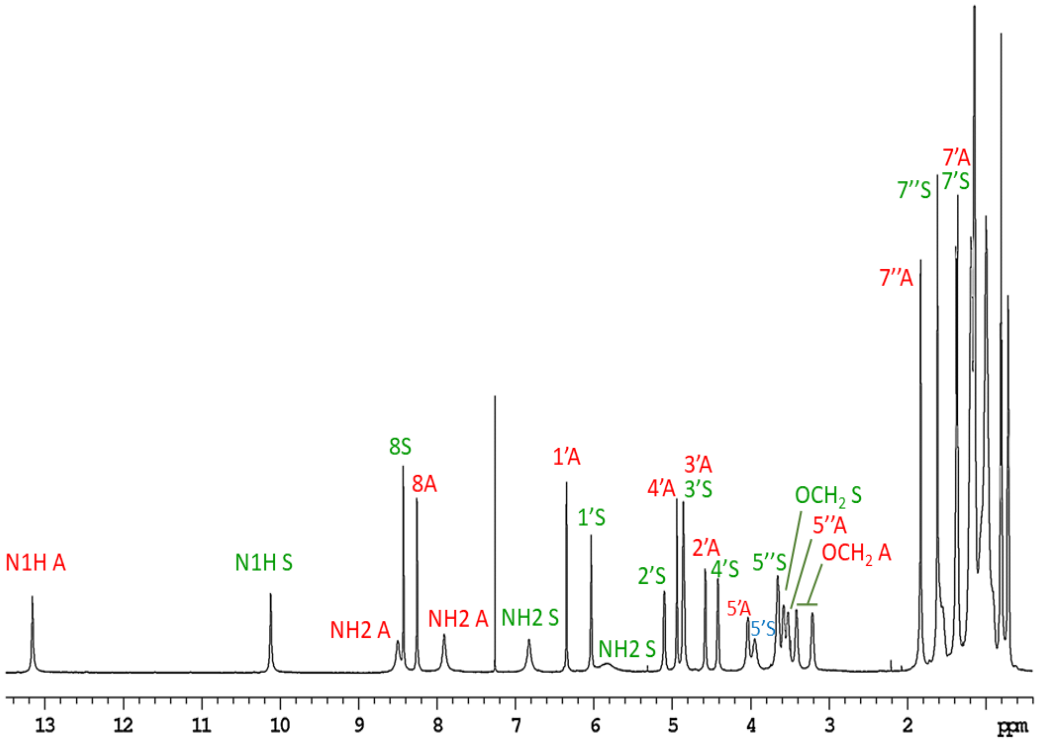

Figure 7. The r.t. ^{1}H-NMR spectrum of the 1:1 complex peaks assignment in the r.t. ^{1}H-NMR spectrum of the 1:1 **LG1**:$AgNO_3$ complex.

The ^{109}Ag NMR spectrum of the complex (**Figure 8**) shows two signals of similar intensity at very different chemical shifts, 202.6 and 402.6 ppm respectively. The two signals could be due to two differently bound silver ions (e.g. N7-Ag-O6 and N7-Ag-N7) or to the binding of Ag^{+}, with the same connectivity, to two different G conformers. In light of the very large difference in chemical shift, the first hypothesis seems more likely, but we were unable to find data in the literature to corroborate it. To the best of our knowledge, a ^{109}Ag NMR spectrum of a silver/guanosine complex has never been reported.

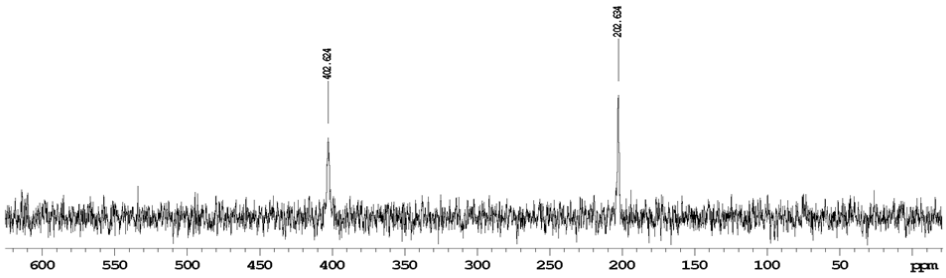

Figure 8. ^{109}Ag NMR spectrum of the complex.

The proton decoupled ^{15}N-NMR spectrum recorded on the **LG1**/Ag^+ 1:1 complex at r.t. in $CDCl_3$ is shown in **Figure 9**. Literature ^{15}N-NMR chemical shifts for guanosine are reported in **Table 4** for shake of comparison [22]. Two sets of signals are present in the spectrum, analogously to what observed in ^{1}H, ^{13}C and ^{109}Ag spectra. The position of N1, N9 and NH_2 resonances fits well with those of native G. It is known from literature [23] that N1 chemical shift for G and dG is around 146 ppm both in water and DMSO, and is not affected by substituents on sugar. This signal is significantly downfiled shifted (> 50 ppm) as consequence of either enolate formation or O6 alkylation. The presence of two peaks in the normal chemical shift range for N1 (149.61 and 145.95 ppm) and the absence of signals below 200 ppm suggests that for the **LG1**/Ag^+ complex no enolization phenomena are involved.

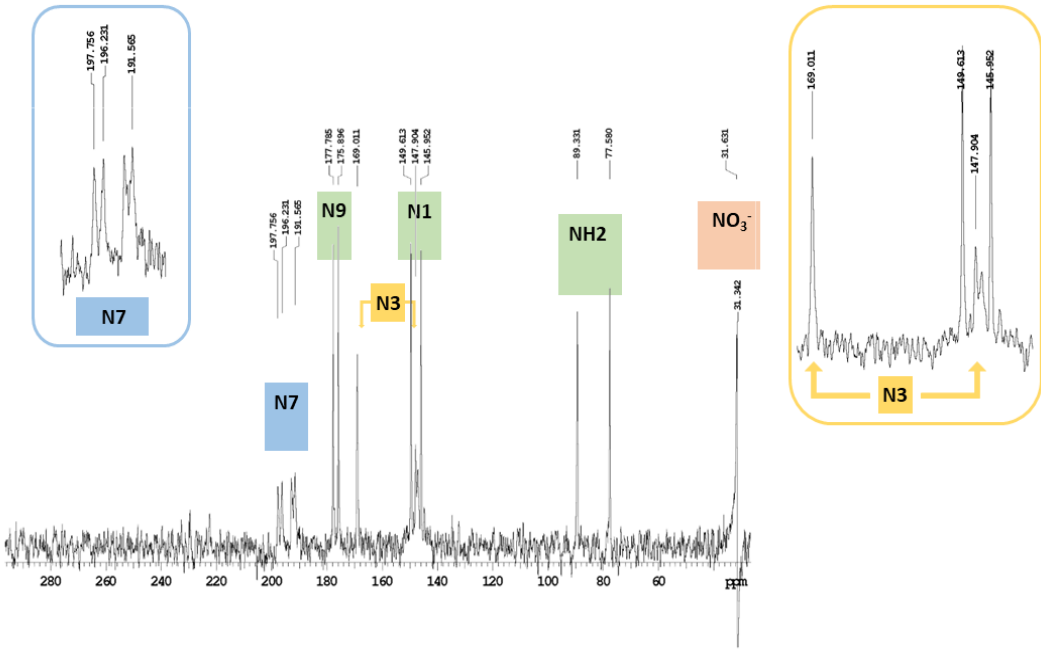

Figure 9. The proton decoupled ^{15}N-NMR spectrum recorded on the **LG1**/Ag^+ 1:1 complex at r.t. in $CDCl_3$.

N7	N9	N3	N1	NH_2
246.0	169.0	164.8	146.2	72.3

Table 4. ^{15}N-NMR chemical shifts (ppm) of G in dmso-d_6 [22].

On the other hand, the absence of signals below 200 ppm implies also that N7 signal, which normally appears at 247-248 ppm for G and dG, is up-field shifted in the **LG1**/Ag^+ spectrum. It is known [22, 24] that coordination of a metal ion (Hg^{2+}, Cd^{2+}, Zn^{2+}) leads to a strong upfield shift of the nitrogen involved. In particular, it has been reported that the N7 signal undergoes an up-field shift of up to 20 ppm when N7 is involved in metal coordination, and moves up to 158-160 ppm in N7-methylated ammonium derivatives. We therefore assign signals in the 191-198 ppm range to N7s of the **LG1**/Ag^+ complex. These signals appear as a couple of doublets centered at 197.0 ppm (*J*=85.0 Hz) and 192.2 ppm (J=82.6 Hz). Both the up-field shift and the coupling constants magnitude [11d] suggest the presence of two different N7s, both coordinated to Ag^+. The N3 signals show a peculiar behaviour: an N3 appears at 169.01 ppm, in line with native G or dG, while the second N3 appears as an up-shifted doublet at 147.5 ppm (*J*=51.0 Hz), indicating interaction of this N3 with silver ion. Thus, both N7s but only one N3 are silver-bonded, supporting the hypothesis that the two signals in the ^{109}Ag NMR spectrum arise from silver ions bound to different nitrogens.

The folded signal, which appears at 31.71 ppm in **Figure 9** and whose real chemical shift can be calculated to be 402 ppm, can be assigned to the nitrate ion. It is unlikely that nitrate ions in $CDCl_3$ were free and they must form ionic couples with the complex: VCD spectra (**Figure 10**) of the complex show indeed an albeit weak optical activity at the stretching frequency of the nitrate ion [25] suggesting that nitrates are actually bound to the complex.

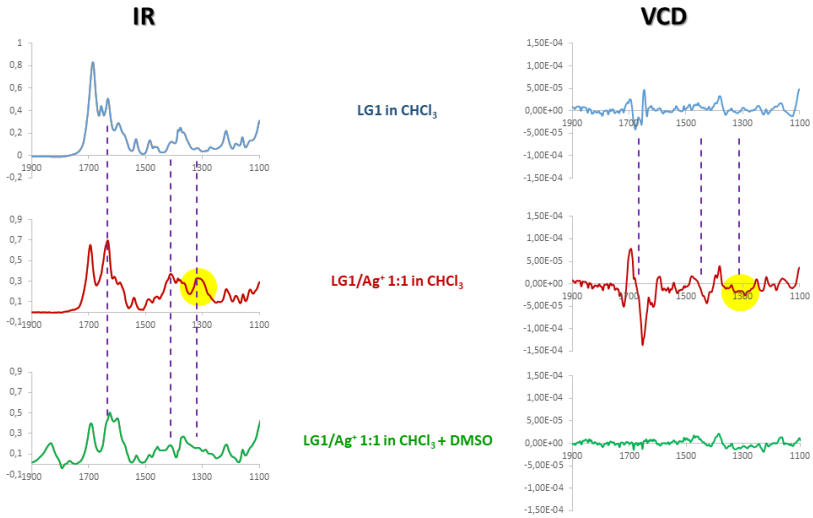

Figure 10. IR and VCD spectra of LG1/Ag^+ complex.

Furthermore, in the ^{13}CNMR spectrum of uncomplexed **LG1**, the C6 signal appears at 157.6 ppm in DMSO and at 158.1 ppm in $CDCl_3$. In the **LG1**/Ag 1:1 complex two C6 signals are present at essentially the same frequencies, 158.0 and 156.5 ppm in $CDCl_3$. It is known that an alteration of the tautomeric form of guanine produces a downfield shift of C6 resonance [26]: for instance, C6 resonates at 156.8 ppm for native G and at 161.1 ppm for O6-methylated G in DMSO, respectively. Comparison of these values confirms the absence of tautomeric forms.

Analogously to what observed here for **LG1**/Ag^+, complexes with C_4 symmetry originated by stacking of G-quartets from lipophilic guanosines can indeed show ^{1}H-NMR spectra with two sets of signals in a 1:1 ratio, and a strong optical activity in the ECD spectrum, the latter being due to the helical stacking of the nucleobases. Nonetheless, G-quartet based complexes do form at completely different G/metal stoichiometric ratios (typically G:metal 8:1 – 4:1), show a markedly different behaviour as far as exchangeable protons are concerned (for instance, no upfield shift of imino protons) and are often observable by ESI-MS (cfr. below). This rules out the presence of G-quartets in this case.

In spite of the fact that ESI-MS spectra recorded on **LG1**/Ag^+ samples (**Figure 11**) did not show signals attributable to species heavier than the [**LG1**$_2$-Ag]$^+$ dimer, the hypochromic effect observed in titration experiments, the presence of two couplets in the ECD spectrum and the phase of cross-peaks in NOESY spectra (see below) rule out a simple dimeric structure and point to a more complex, pi-stacked aggregate, built of dimeric structural units. Only 50% of silver ions is essential for generating dimeric G species, while residual Ag^+ is loosely linked to guanosines and is not detected by electrospray ionization but, as underlined above, is essential for complex formation in solution.

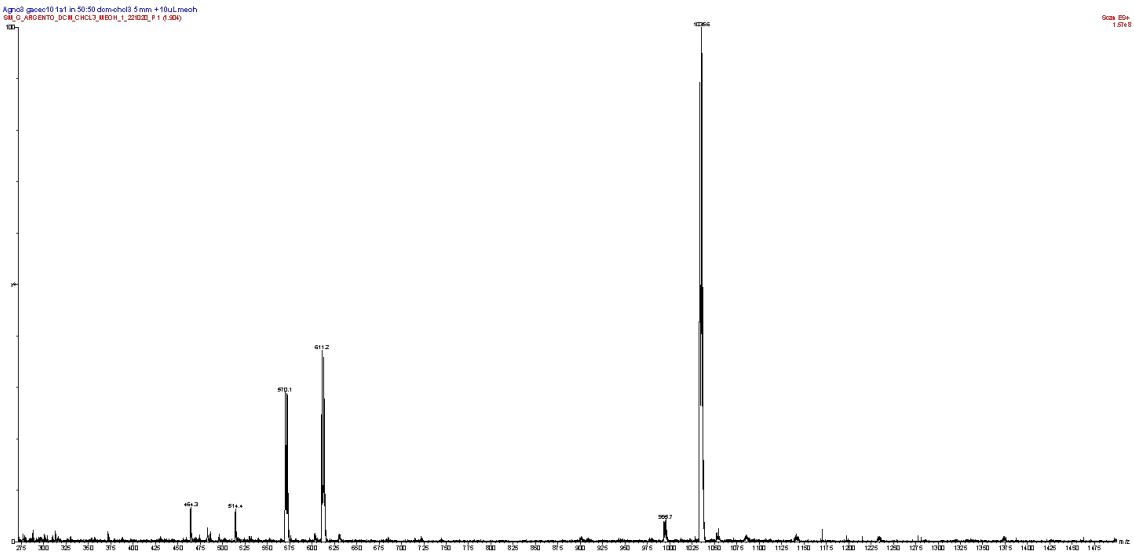

Figure 11. ESI of **LG1**/Ag^+ 1:1 in 50:50 MeCN/DCM (positive mode) – 10ml of MeOH added.

Considering that all N7s are bound to Ag^+ and ESI clearly shows the presence of **LG1**$_2$$Ag^+$ dimers, we can take the (G)N7-Ag^+-N7(G) (**Figure 1c**) as the basic structural unit of the complex. According to both calculations and X-ray data [16], this dimeric structure exists in what could be regarded as "s-trans" conformation, with the two bases lying on the opposite sides of the perpendicular plane containing the N7-Ag-N7 fragment (**Figure 11**).

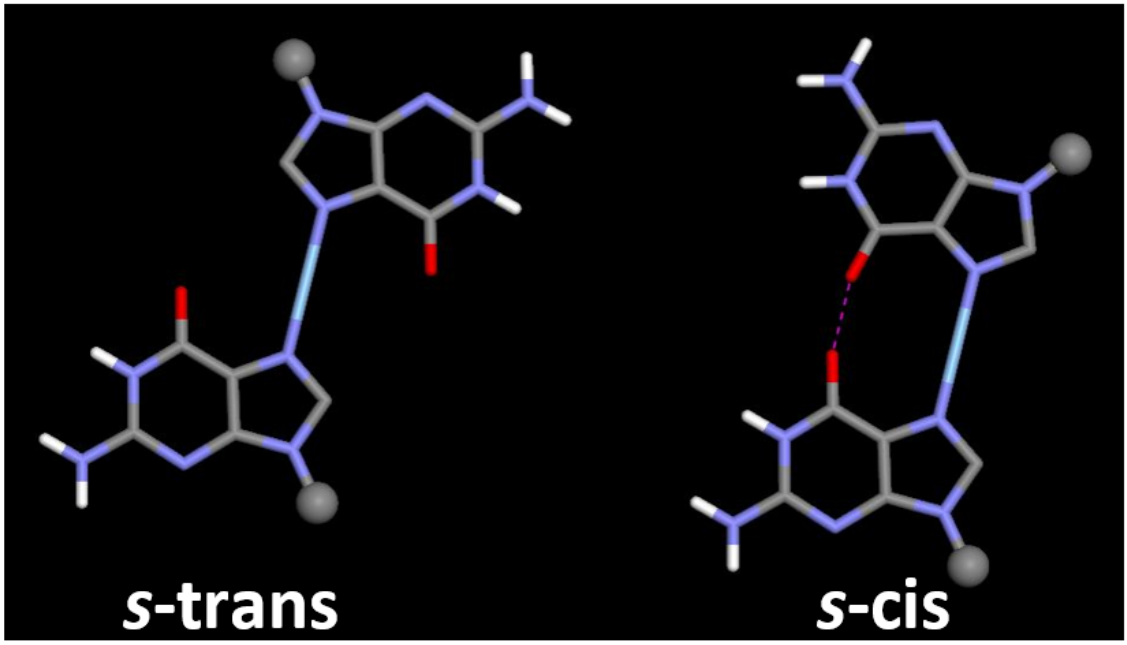

Figure 12. The two possible structures of the basic units of the complex.

Most of the evidences presented so far can be accounted for by a simple dimeric structure, but both UV-ECD data and NOE experiments point to a more complex structure. UV-ECD data (hypochromism and presence of two couplets, respectively) suggest a stacked structure. NOE experiments (see below) show invariably antiphase correlations with respect to the irradiated peak, characteristic of the "slow tumbling regime" and suggestive of species in solution with a molecular weight > 2000 Da. The calculated mass of the structure of **Figure 11** is 1266 Da, a value in the "intermediate motion regime", where NOE signals are often not observable [27].

To examine the stacking of these basic units, another aspect must be taken into account: the two faces of guanosine are diastereotopic. We label head (H) the face where walking from O6 to C6 to C5 to N7 one describes a clockwise rotation and we label tail (T) the face where the same path leads to an anticlockwise rotation (**Figure 13**).

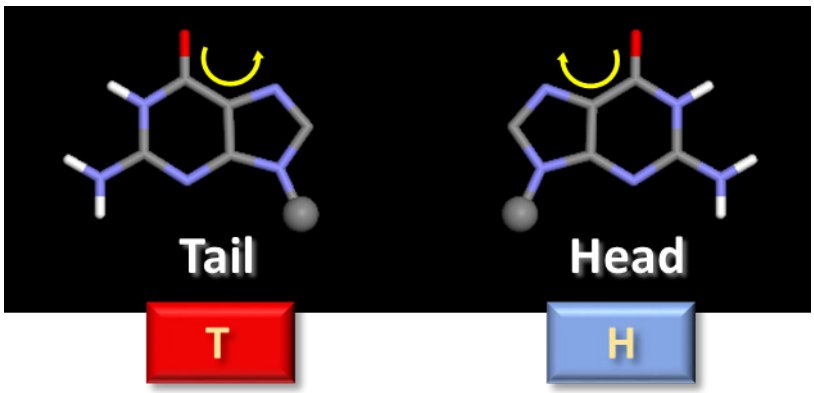

Figure 13. Diasterotopic faces of the guanosine. H= face where walking from O6 to C6 to C5 to N7 one describes a clockwise rotation, T= the face where the same path leads to an anticlockwise rotation.

As a consequence of the s-trans conformation, the two guanosines of a dimeric unit show the same face (both H or both T) on each side. When two such units pi-stack on top of each-other, the stacking can be either homopolar (two like-faces facing each-other, H to H or T to T) or heteropolar (H to T or T to H) (**Figure 14**), leading in principle to the formation of a large number of diastereoisomeric complexes.

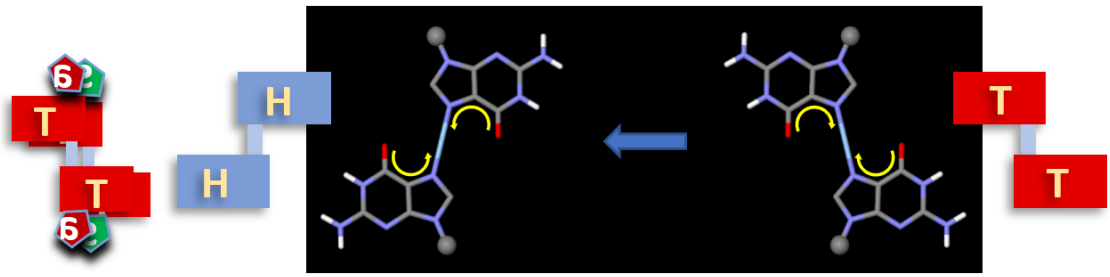

Figure 14. Left : TT and HH faces of a dimer. Rightb: example of heteropolar H to T stacking.

The complex must contain an equal number of *syn* and *anti* conformers. Thinking of two stacked dimeric units, there are two possibilities: a fully-*anti* dimer stacked onto a fully-*syn* dimer or two stacked identical dimers, containing both conformers each (mixed dimers). In addition, the double set of signals in both the ^{1}H and ^{13}C NMR spectra indicate that the complex must belong to the C_2 point group. **Figures 15-16** show selected NOESY-1D and ROESY-1D spectra. As mentioned above, correlations are always antiphase with respect to the irradiated peak. Irradiation of 5' or 2' protons is consistent with the conformational *syn/anti* assignment. In particular, the correlation between 2'S and both 6 ppm NH_2 and 10 ppm NH, allows the assignment of these exchangeable protons. What was puzzling at the beginning is the anomalous intensity of the 2'A/1'A and 2'S/8 correlations. Normally, 2'H has a stronger correlation with H1' than with H8 in the *syn* conformer and the opposite is observed in the *anti* conformer [28]. The same observation can be made on the -50°C ROESY-1D spectrum of **Figure 15**. Another relevant point one can make out of these spectra is the lack of correlations between signals belonging to *syn* conformers and signals belonging to *anti* conformers. The only correlations relating *syn* and *anti* conformers we did observe are shown in **Figure 16**: the up-field N1H S signal shows proximity with both N1H A and H1' A. The lack of through-space interactions between the two conformers makes it unlikely the stacking between a fully-*anti* dimer and a fully-*syn* dimer. On the contrary, the stacking of mixed dimers can account for it, if *syn* conformer stacks with *syn* and *anti* stacks with *anti*. In this case, also the anomalous intensities of some NOE signals can find an explanation, being the result of both intramolecular and intermolecular (i.e. interdimer) contributions.

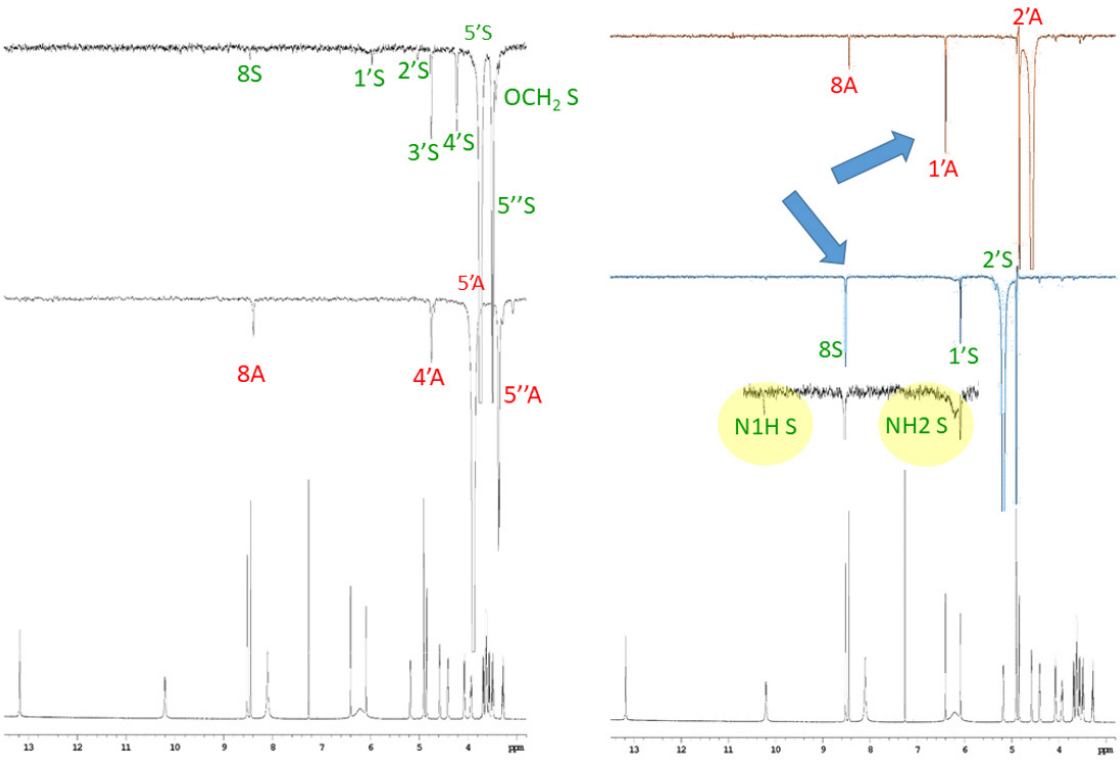

Figure 15. Selected NOESY-1D spectra at r.t.: irradiation of 5'S (top left), 5'A (bottom left), 2'A (top right) and 2'S (bottom right).

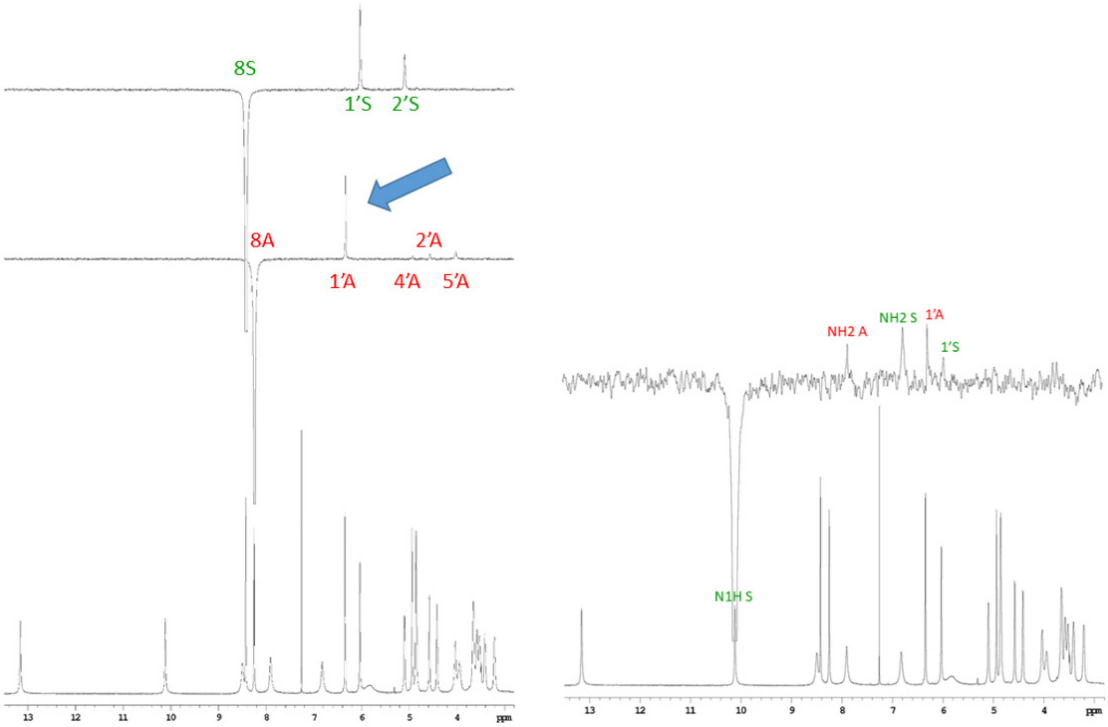

Figure 16 Selected ROESY-1D spectra at -50°C: irradiation of 8S (top left), 8A (bottom left) and N1H S (right).

Conclusion

In light of the evidences presented above, the examination of the alternative stereoisomeric complexes in light of the evidences presented above allows to identify one compatible structure, which is shown in **Figure 17**. The complex has a C_2 symmetry and contains 4 guanosines and 4 $AgNO_3$ units (overall stoichiometry 1:1). It arises from the homopolar stacking of two mixed dimers (synG_N7--Ag^+--N7_antiG), with the second couple of silver atoms connected to N3s of the *anti* conformers. Imino and amino protons of *anti* conformers are all H-bonded to nitrate ions, while the corresponding *syn* protons are free. The structure accounts for the NOE proximities mentioned above (indicated by arrows).

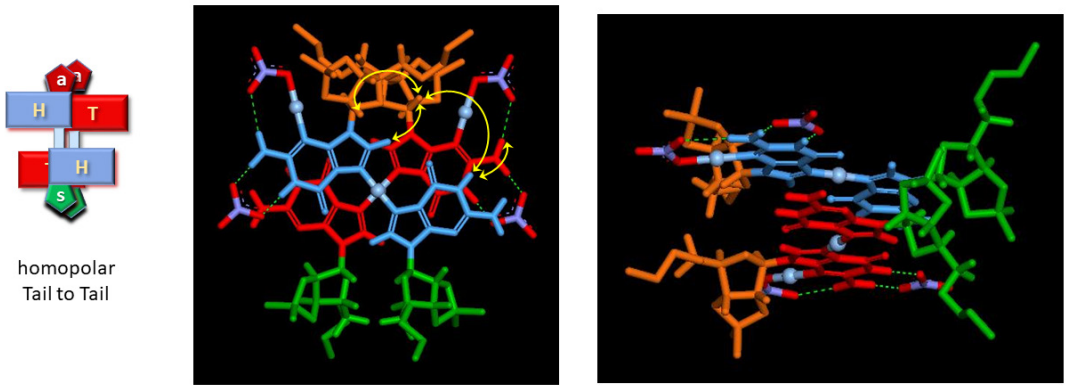

Figure 17. LG1/Ag+ proposed Complex, stoichiometry 1:1.

Methods and materials

General Methods.

Macherey-Nagel polygram silica gel plates (layer thickness 0.20 mm) were used for thin layer chromatography (TLC) analyses. Column chromatography was performed on Geduran silica gel 60 (40–63 μm). Reagents (Guanosine and 1Br-Decane) and dry solvents, were purchased from Sigma-Aldrich or TCI. Electrospray ionization (ESI) mass spectra were obtained from methanol solutions in either the positive or negative mode, with Micromass ZMD 4000 or ZQ- 4000 instruments. Nuclear magnetic resonance (NMR) spectra were recorded on Varian Inova (600, 400, or 300 MHz) spectrometers and referenced to the residual solvent resonance (s = singlet, bs = broad singlet, d = doublet, t = triplet, q = quartet, qi = quintet, m = multiplet; coupling constant are in Hz). Structural assignments were made with additional information from gCOSY (gradient-selected correlation spectrosco- py), gHSQC (gradient-selected heteronuclear single-quantum corre- lation), and gHMBC (gradient-selected heteronuclear multiple bond correlation) experiments. Diastereotopic protons/carbons were not assigned. CD spectra were recorded on a Jasco J-710 spectropolarim- eter. Synthetic schemes with compound numbering are reported in the following information.

Synthesis

2-amino-9-[6-(hydroxymethyl)-2,2-dimethyl-tetrahydro-2H furo[3,4-d][1,3]dioxol-4-yl]-6,7,8,9- tetrahydro-1H-purin-6-one GACE. Commercial guanosine (2,5 g, 1 eq., 8,86 mmol) was suspended in 150 ml of acetone in a 1000 ml flask and left stirring. 70% perchloric acid (1 ml, 1,34 eq, 11,62 mmol) was added dropwise obtaining immediately a colourless solution. After 70 minutes, a solution of ammonium hydroxyde (7,455M, 1,67 ml. 1,4 eq., 12,45 mmol) was added and the mixture was cooled down in an ice bath. Water (120 ml) was added and the solution was concentrted under vacuum pressure until the formation of a precipitate and the removal of the acetone. The solid was filtered ad dryed, the product was obtained in a 80 % yield (2,293 g, 7,1 mmol) as white crystals.

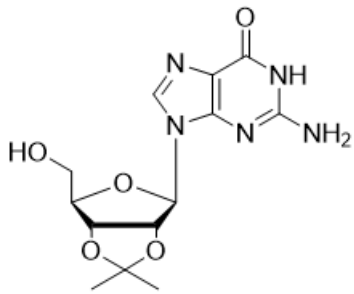

2-amino-9-{6-[(decyloxy)methyl]-2,2-dimethyl-tetrahydro-2H-furo[3,4-d][1,3] dioxol-4-yl}-6,7,8,9-tetrahydro-1H-purin-6-one LG1. GACE (1,037 g, 1 eq. 3,2 mmol) was dried under vacuum for 3 h at 55°C. Afterwards it was put in a 100 ml flask under nitrogen flow and dissolved in 25 ml of anhydrous THF at RT. KI (0,053 g, 0.1 eq., 0.32 mmol), 1 Br-decane (3,536 g, 5 eq., 16 mmol) and NaH (66%) (0,230 g, 3 eq., 9,6 mmol) were added (the addition of NaH produces some bubbles) and the obtained suspension was left stirring overnight at 65°C. As TLC (CH_2Cl_2/MeOH 9:1) revealed the presence of unreacted starting material, an extra amount of NaH (66 mg, 1 eq., 3,2 mmol) was added, and reaction was

continued for 4 h. After cooling to room temperature, solvents were removed by distillation. The light-yellow residue was dissolved in 30 mL of CH_2Cl_2 and washed with water (3x20 ml), brine (40 mL) and then dried over $MgSO_4$. The organic solution was dried under vacuum and a light-yellow solid was obtained (4 g). The residue was purified by column chromatography on silica gel (CH_2Cl_2/MeOH 95:5). The obtained withe powder (330 mg) was crystalized in ethanol (13 ml) and the product was obtained in a 18 % yield (268 mg, 0.576 mmol) as a white solid. RF = 0.3 (CH_2Cl_2/MeOH 95:5).

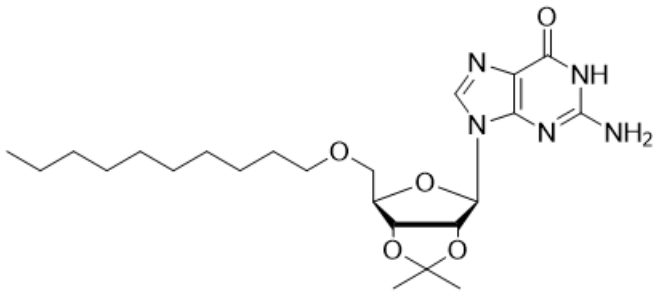

References

[1] (a) Zhou, W., Saran, R., & Liu, J. (2017). Metal Sensing by DNA. Chemical Reviews, 117, 8272-8325. (b) Kondo, J., Tada, Y., Dairaku, T., Hattori, Y., Saneyoshi, H., Ono, A., & Tanaka, Y. (2017). Nat. Chem., 9, 956-960. (c) Copp, S. M., Schultz, D. E., Swasey, S., & Gwinn, E. G. (2015). ACS Nano, 9, 2303-2310. (d) Gwinn, E., Schultz, D., Copp, S. M., & Swasey, S. (2015). Nanomaterials, 5, 180-207.

[2] (a) Lippert, B., & Sanz Miguel, P. J. (2016). Acc. Chem. Res., 49, 1537-1545. (b) Takezawa, Y., & Shionoya, M. (2012). Acc. Chem. Res., 45, 2066-2076. (c) Lippert, B. (2000). Coordination Chemistry Reviews, 200-202, 487-516.

[3] (a) Ceramella, J., Mariconda, A., Iacopetta, D., Saturnino, C., Barbarossa, A., Caruso, A., Rosano, C., Sinicropi, M. S., & Longo, P. (2020). Bioorganic & Medicinal Chemistry Letters, 30, 126905. (b) Liang, X., Luan, S., Yin, Z., He, M., He, C., Yin, L., Zou, Y., Yuan, Z., Li, L., Song, X., & Lv, C. (2018). European Journal of Medicinal Chemistry, 157, 62-80.

[4] Roy, A., Bulut, O., Some, S., Mandal, A. K., & Yilmaz, M. D. (2019). Influence of local strain caused by cycloaddition on the band gap control of functionalized single-walled carbon nanotubes. RSC Advances, 9, 2673-2678.

[5] (a) Stefan, L., & Monchaud, D. (2019). Nature Reviews Chemistry, 3, 650-668. (b) Davis, J. T., & Spada, G. P. (2007). Chemical Society Reviews, 36, 296-313.

[6] Fritzsche, W., & Spindler, L. (Eds.). (2013). Guanine quartets: Structure and application. RSC Publishing.

[7] Campitiello, M., Cremonini, A., Squillaci, M. A., Pieraccini, S., Ciesielski, A., Samorì, P., & Masiero, S. (2021). Self-Assembly of Functionalized Lipophilic Guanosines into Cation-Free Stacked Guanine-Quartets. J. Org. Chem., 86, 9970-9978.

[8] Yoshikawa, I., Sawayama, J., & Araki, K. (2008). Highly Stable Giant Supramolecular Vesicles Composed of 2D Hydrogen-Bonded Sheet Structures of Guanosine Derivatives. Angew. Chem. Int. Ed., 47, 1038-1041.

[9] Swasey, S. M., Rosu, F., Copp, S. M., Gabelica, V., & Gwinn, E. G. (2018). Parallel Guanine Duplex and Cytosine Duplex DNA with Uninterrupted Spines of AgI-Mediated Base Pairs. J. Phys. Chem. Lett., 9, 6605-6610.

[10] Swasey, S. M., & Gwinn, E. G. (2016). Silver-mediated base pairings: towards dynamic DNA nanostructures with enhanced chemical and thermal stability. New J. Phys., 18, 045008.

[11] (a) Berdakin, M., Féraud, G., Dedonder-Lardeux, C., Jouvet, C., & Pino, G. A. (2014). J. Phys. Chem. Lett., 5, 2295-2301; (b) Megger, D. A., & Müller, J. (2010). Nucleosides, Nucleotides Nucleic Acids, 29, 27-38; (c) Ono, A., Cao, S., Togashi, H., Tashiro, M., Fujimoto, T., Machinami, T., Oda, S., Miyake, Y., Okamoto, I., & Tanaka, Y. (2008). Chem. Commun., 4825-4827; (d) Dairaku, T., Furuita, K., Sato, H., Šebera, J., Nakashima, K., Kondo, J., Yamanaka, D., Kondo, Y., Okamoto, I., Ono, A., Sychrovský, V., Kojima, C., & Tanaka, Y. (2016). Chem. Eur. J., 22, 13028-13031.

[12] Cini, R., Colamarino, P., & Orioli, P. L. (1977). A proton magnetic resonance investigation on 1:1 cytidine and guanosine silver(I) complexes. Bioinorg. Chem., 7, 345-349.

[13] Loo, K., Degtyareva, N., Park, J., Sengupta, B., Reddish, M., Rogers, C. C., Bryant, A., & Petty, J. T. (2010). Ag(+)-mediated assembly of 5′-guanosine monophosphate. J. Phys. Chem. B, 114, 4320-4326.

[14] Dash, J., Patil, A. J., Das, R. N., Dowdall, F. L., & Mann, S. (2011). Supramolecular hydrogels derived from silver ion-mediated self-assembly of 5′-guanosine monophosphate. Soft Matter, 7, 8120-8126.

[15] Lippert, B. (2005). Chapter 6: Bioinorganic Chemistry. In K. D. Karlin (Ed.), Progress in Inorganic Chemistry, Vol. 54 (pp. 183-234). John Wiley & Sons.

[16] Swasey, S. M., Leal, L. E., Lopez-Acevedo, O., Pavlovich, J., & Gwinn, E. (2015). Silver (I) as DNA glue: Ag(+)-mediated guanine pairing revealed by removing Watson-Crick constraints. Sci. Rep., 5, 10163–10171.

[17] Liu, H., Shen, F., Haruehanroengra, P., Yao, Q., Cheng, Y., Chen, Y., Yang, C., Zhang, J., Wu, B., Luo, Q., et al. (2017). A DNA Structure Containing AgI -Mediated G:G and C:C Base Pairs. Angew. Chem., Int. Ed., 56, 9430–9434.

[18] Feng, H., Du, Y., Tang, F., Ji, N., Zhao, X., Zhao, H., & Chen, Q. (2018). Silver ions blocking crystallization of guanosine-based hydrogel for potential antimicrobial applications. RSC Adv., 8, 15842–15852.

[19] Ciesielski, A., El Garah, M., Masiero, S., & Samorì, P. (2015). Self-assembly of Natural and Unnatural Nucleobases at Surfaces and Interfaces. Small, 12, 83–95.

[20] Masiero, S., Trotta, R., Pieraccini, S., De Tito, S., Perone, R., Randazzo, A., & Spada, G. P. (2010). A non-empirical chromophoric interpretation of CD spectra of DNAG-quadruplex structures. Org. Biomol. Chem., 8, 2683–2692.

[21] Vokacova, Z., Bickelhaupt, F. M., Sponer, J., & Sychrovsky, V. (2009). Structural interpretation of J coupling constants in guanosine and deoxyguanosine: modeling the effects of sugar pucker, backbone conformation, and base pairing. J. Phys. Chem. A, 113, 8379–8386.

[22] Bucmanan, G. W., & Stothers, J. B. (1982). Diamagnetic metal ion – nucleoside interactions in solution as studied by 15N nuclear magnetic resonance. Can. J. Chem., 60, 787–791.

[23] Cho, B. P., Kadlubar, F. F., Culp, S. J., & Evans, F. E. (1990). Nitrogen-15 nuclear magnetic resonance studies on the tautomerism of 8-hydroxy-2′-deoxyguanosine, 8-hydroxyguanosine, and other C8-substituted guanine nucleosides. Chem. Res. Toxicol., 3, 445–452.

[24] Tanaka, Y., & Ono, A. (2008). Nitrogen-15 NMR spectroscopy of N-metallated nucleic acids: insights into 15N NMR parameters and N–metal bonds. Dalton Trans., 4965–4974.

[25] Goncharova, I. (2014). Ag (I)-mediated homo and hetero pairs of guanosine and cytidine: Monitoring by circular dichroism spectroscopy. Spectrochim. Acta A, 118, 221–227.

[26] Chang, C., Ashworth, D. J., Chern, L., DaSilva Gomes, J., Lee, C., Mou, P. W., & Narayan, R. (1984). 13C NMR studies of methylnucleosides. Org. Magn. Reson., 22, 671–675.

[27] Claridge, T. D. V. (1999). High-Resolution NMR Techniques in Organic Chemistry. Pergamon-Elsevier, Oxford.

[28] (a) Marlow, A. L., Mezzina, E., Spada, G. P., Masiero, S., Davis, J. T., & Gottarelli, G. (1999). J. Org. Chem., 64, 5116–5123; (b) Mezzina, E., Mariani, P., Itri, R., Masiero, S., Pieraccini, S., Spada, G. P., Spinozzi, F., Davis, J. T., & Gottarelli, G. (2001). Regular Polymer. Chem. Eur. J., 7, 388–395.

THE END

Alessio Cremonini